

ABSTRACT

LI, QINMIAO. Control Schemes for Photovoltaic Systems to Provide Frequency Support to the Electric Power System. (Under the direction of Dr. Mesut Baran).

This thesis focuses on control schemes that can utilize photovoltaic (PV) generation systems to provide frequency support to the electric power systems. A series of work involving PV penetration impact studies, PV system modeling, and controller design have been carried out in this thesis.

Currently, growing level of PV penetration is challenging the conventional generation control scheme in electric power system. The inverter-based PV systems do not possess rotating inertia or governor systems. Thus, the frequency response capability in a power system degrades when more PV systems are introduced in replace of synchronous generation. To identify and assess the corresponding impact on frequency response, two simulation testbeds are developed. One testbed is based on PSCAD and can be used for time-domain simulations of small systems, while the other one adopts co-simulation algorithms and suits for phasor-domain simulations of very-large-scale systems. Using the two testbeds, simulations of the frequency event under different PV penetration clearly indicate the negative impact of higher PV penetration on the frequency response, in terms of frequency nadir, rate of change of frequency, and settling frequency.

Then, to enable frequency support functions from PV and improve the frequency response, we first consider the large-scale PV plant which consists of identical subsystems. To design the control functions, a new small-signal model (SSM) for a three-phase two-stage PV system is proposed. Comparing to existing models, this SSM includes full dynamics of PV system and is also suitable for designing frequency support controls. Using this SSM, we propose a novel frequency support control method which is different than other approaches which only focus on

emulating droop and inertial responses of local PV. The proposed method uses a tracking linear quadratic regulator (LQR) based controller to help the system frequency effectively track that of a designed reference system with given inertia and droop constants. To design this LQR, an unknown input observer (UIO) is adopted to estimate the system states, as well as the unknown disturbance. The proposed SSM is validated against the detailed nonlinear PV system model, and the effectiveness of the proposed controller is demonstrated using a standard test system. Test results also show that the proposed method achieves the desired frequency response more effectively than the alternative method from literature, while the later method is liable to over-compensation of frequency response at the price of requiring more power reserve in PV.

As the other popular type of installation, distributed PV represent a considerable portion of the growing PV integration. Comparing to large-scale PV plants, distributed PV are usually smaller in size and have diversities in working conditions and parameters. To enable frequency support functions, existing approaches for large-scale PV plants may not be adopted for distributed PV. Therefore, based on our work on large-scale PV plants, we also propose a novel control scheme for the same purpose but focusing on distributed PV. To address the diversities among distributed PV, a reduced-order aggregate model is proposed to represent their overall dynamic behavior. Then, using this model, we adopt the UIO-based tracking LQR to supervise a group of distributed PV to provide frequency support. In addition, considering practical implementation, we also propose an inversion method for the controller to invert the control signals for aggregate model back to each individual PV's. The proposed reduced-order model is validated against a group of distributed PV systems represented by detailed nonlinear model. We also demonstrate the effectiveness of the control scheme, as well as the inversion method, through time-domain simulations using standard test system.

© Copyright 2020 by Qinmiao Li

All Rights Reserved

Control Schemes for Photovoltaic Systems to Provide Frequency Support to the Electric Power System

by
Qinmiao Li

A dissertation submitted to the Graduate Faculty of
North Carolina State University
in partial fulfillment of the
requirements for the degree of
Doctor of Philosophy

Electrical Engineering

Raleigh, North Carolina
2020

APPROVED BY:

Dr. Mesut Baran
Committee Chair

Dr. David Lubkeman

Dr. Aranya Chakraborty

Dr. Yahya Fathi

DEDICATION

To my parents

Youbin Li and Zhenping Zhi

and in memory of my grandfather

Xiaolin Zhi

BIOGRAPHY

Qinmiao Li was born in Liaocheng, Shandong, China, in 1991. He received his B.E. degree in electrical engineering and its automation from Shandong University, China. In 2015, he obtained his M.S. degree in electrical engineering from North Carolina State University, Raleigh, USA, where he is currently pursuing his Ph.D. degree. From 2015 to 2016, he was with ETAP, Operations Technology, Inc. as an automation and control engineer. During the summers in 2017 and 2018, he did internships at National Renewable Energy Laboratory and Argonne National Laboratory, respectively. His research interests include dynamic modeling, and supervisory control of photovoltaic systems.

ACKNOWLEDGMENTS

My first and sincere gratitude goes to my advisor Dr. Mesut Baran, who has dedicated his knowledge, insights, and patience to me. He shapes the way for me as a fresh graduate to enter the research realm and continues to guide me finding my path in it. I appreciate everything learned from him. This dissertation will not be possible without him.

Meanwhile, I would like to thank my committee members: Dr. Aranya Chakraborty, Dr. Yahya Fathi, and Dr. David Lubkeman for their advice on my dissertation. I would like to thank Dr. Shrirang Abhyankar from Argonne National Lab for his guidance on the work of Chapter 2.

I also feel very grateful to have my lovely friends at NC and awesome colleagues at FREEDM Center: Lisha Sun, Liqi Zhang, Anjie Jiang, Mengran Zhu, Mingyu Yang, Hongyu Wu, Yue Shi, Yao Ma, Xiangqi Zhu, Haotao Ke, Xin Tao, Yuhua Du, Jiyu Wang, Qian Long, and Hui Yu. Their friendships and support make me the lucky one.

My special thanks go to my beloved Danyang Wang, who sacrifices so much for me and always has her faith in me. It has been her closest company over the longest distance that lights up my days.

Last and foremost, I have my heartfelt gratitude for my parents: Youbin Li and Zhenping Zhi. They are the greatest parents who have devoted endless love and support to me throughout my entire life.

TABLE OF CONTENTS

| | |
|---|------|
| LIST OF TABLES | viii |
| LIST OF FIGURES | ix |
| Chapter 1 : Introduction | 1 |
| 1.1 Overview of Conventional Generation Control | 3 |
| 1.2 Impacts of PV Penetration on Generation Control..... | 7 |
| 1.3 Frequency Support Control Functions of PV | 9 |
| 1.4 Proposed Control Schemes for Distributed PV..... | 11 |
| Chapter 2 : Impact of High PV Penetration on Frequency Response..... | 14 |
| 2.1 PV Modeling | 14 |
| 2.1.1 Average Model | 14 |
| 2.1.2 2-dq Average Model..... | 23 |
| 2.1.3 PVD1 Model | 24 |
| 2.1.4 Comparison of PV Models | 25 |
| 2.2 Testbed Development..... | 27 |
| 2.2.1 PSCAD Testbed | 27 |
| 2.2.2 Dynamic Co-simulation Testbed..... | 28 |
| 2.3 Results and Evaluation of High PV Penetration Impact on Frequency Response .. | 36 |
| 2.3.1 Frequency Response in PSCAD..... | 36 |
| 2.3.2 Frequency Response in Dynamic Co-simulation | 39 |
| Chapter 3 Frequency control scheme for large-scale PV plants | 43 |
| 3.1 System Modeling..... | 46 |
| 3.1.1 Large-scale PV Plant..... | 46 |

| | | |
|--|--|-----|
| 3.1.2 | Transmission System..... | 51 |
| 3.1.3 | Combined System | 51 |
| 3.2 | Controller Design | 53 |
| 3.2.1 | Unknown Input Observer | 54 |
| 3.2.2 | Reference System..... | 56 |
| 3.2.3 | LQR..... | 56 |
| 3.2.4 | Analysis of Close-loop System | 59 |
| 3.3 | Test Results | 62 |
| 3.3.1 | Model Validation..... | 62 |
| 3.3.2 | Controller Performance | 64 |
| 3.3.3 | Comparison with Alternative Method..... | 71 |
| 3.3.4 | Implementation..... | 74 |
| 3.4 | Conclusion..... | 77 |
| Chapter 4 : Frequency support control scheme for distributed PV..... | | 79 |
| 4.1 | System Modeling..... | 81 |
| 4.1.1 | The Single-phase Two-stage PV System | 81 |
| 4.1.2 | The Reduced-order Aggregate Model..... | 86 |
| 4.1.3 | Transmission System..... | 94 |
| 4.2 | Proposed Control Scheme | 95 |
| 4.2.1 | LUT and the Combined System Model..... | 95 |
| 4.2.2 | The UIO-based Tracking LQR..... | 97 |
| 4.2.3 | Inversion of Control Signal | 97 |
| 4.3 | Test Results | 101 |

| | |
|--|-----|
| 4.3.1 Reduced-order Aggregate Model Validation | 101 |
| 4.3.2 Controller Performance | 104 |
| 4.4 Conclusion..... | 109 |
| Chapter 5 : Summary and future work..... | 110 |
| 5.1 Summary of Current Work..... | 110 |
| 5.2 Future Work | 112 |
| References | 113 |
| Appendices | 123 |
| Appendix I: Equations for 2dq PV System Model | 124 |
| Appendix II: System Configurations of PSCAD Testbed | 126 |
| Appendix III: System Configurations of Co-simulation Testbed | 127 |
| Appendix IV: PV System Parameters..... | 128 |
| Appendix V: Distributed PV System Parameters | 129 |
| Appendix VI: Distributed PV System Parameters..... | 130 |

LIST OF TABLES

| | | |
|------------|---|-----|
| Table 2.1. | A Comparison Summary of PV Models | 26 |
| Table 2.2. | A Summary of Evaluation Metrics for PSCAD Testbed | 37 |
| Table 2.3. | A Summary of Evaluation Metrics for Dynamic Co-simulation Testbed | 40 |
| Table 3.1. | Controller Design Parameters | 66 |
| Table 4.1. | Variable Distributions and Corresponding Parameters | 91 |
| Table 4.2. | Part of the Control Design Parameters | 105 |

LIST OF FIGURES

| | |
|--|----|
| Figure 1.1. Governor steady-state frequency droop characteristics [32]. | 3 |
| Figure 1.2. AGC control diagram for one generator [32]. | 4 |
| Figure 1.3. Typical frequency response to a loss of generation [35]. | 6 |
| Figure 1.4. EI frequency response change due to renewable integration [7]. | 8 |
| Figure 1.5. ERCOT frequency response during a 2700 MW generator loss [10]. | 9 |
| Figure 1.6. Diagrams for proposed control schemes for (a) large-scale PV plant; (b) distributed PV. | 12 |
| Figure 2.1. Diagram for a two-stage single-phase PV system. | 15 |
| Figure 2.2. Equivalent circuit of DC-DC converter and DC-link. | 17 |
| Figure 2.3. Equivalent circuit of DC-AC inverter and output filter. | 17 |
| Figure 2.4. Diagram for an ideal PLL. | 18 |
| Figure 2.5. Control diagram of inverter controller. | 19 |
| Figure 2.6. Flowchart of the P&O algorithm in MPPT controller. | 22 |
| Figure 2.7. Diagram for the modified PVD1 model. | 25 |
| Figure 2.8. PV model in PSCAD testbed. | 27 |
| Figure 2.9. Distribution test system connected to an equivalent synchronous generator. | 28 |
| Figure 2.10. Flowchart for the interfacing algorithm. | 32 |
| Figure 2.11. PV model in the dynamic co-simulation. | 33 |
| Figure 2.12. Distribution dynamic simulation using OpenDSS and PETSc. | 34 |
| Figure 2.13. IEEE 14 bus system. | 35 |
| Figure 2.14. IEEE 8500-node test feeder. | 35 |
| Figure 2.15. Frequency response under different PV penetration levels in PSCAD testbed. | 37 |

| | |
|---|----|
| Figure 2.16. Generator and PV generation under different PV penetration levels in PSCAD testbed..... | 38 |
| Figure 2.17. Frequency response under different PV penetration levels in dynamic co-simulation testbed..... | 40 |
| Figure 2.18. Generator and PV generation under different PV penetration levels in dynamic co-simulation testbed..... | 41 |
| Figure 3.1. Conceptual diagram of proposed controller..... | 44 |
| Figure 3.2. Block diagram of a two-stage three-phase PV system..... | 46 |
| Figure 3.3. LUT surface at reference temperature ($T = 26.85^{\circ}\text{C}$) under different solar irradiance levels and ΔV_{PV} | 49 |
| Figure 3.4. Block diagram of the system models..... | 50 |
| Figure 3.5. Architecture and components of the UIO-based tracking LQR..... | 53 |
| Figure 3.6. When $\Delta V_{PV} = -10\text{ V}$, (a), (c) comparison of DC-link voltages and the absolute error; (b), (d) comparison of output power and the absolute error..... | 63 |
| Figure 3.7. When $\Delta V_{dcref} = -10\text{ V}$, (a), (c) comparison of DC-link voltages and the absolute error; (b), (d) comparison of output power and the absolute error..... | 63 |
| Figure 3.8. Modified WECC 9-bus system with PV plant..... | 65 |
| Figure 3.9. (a) Frequency response comparison under load disturbance; (b) Absolute error between test system frequency and reference system frequency..... | 65 |
| Figure 3.10. (a) Comparison of d_c and \hat{d}_c ; (b) Comparison of ΔV_{dc} and $\Delta \hat{V}_{dc}$; (c) Comparison of ΔP_{PV} and $\Delta \hat{P}_{PV}$ | 68 |
| Figure 3.11. Control input ΔP_{PV} | 70 |
| Figure 3.12. Control input ΔV_{dcref} | 70 |

| | |
|---|-----|
| Figure 3.13. (a) Frequency response comparison with load drop; (b) Absolute error between test system frequency and reference system frequency. | 71 |
| Figure 3.14. Conceptual diagram of the alternative method..... | 73 |
| Figure 3.15. Frequency response comparison between proposed controller and alternative method. | 73 |
| Figure 3.16. Comparison of ΔP_{PV} from the cases (a) with proposed control and (b) with alternative method. | 74 |
| Figure 3.17. Comparison between the estimated disturbance with noise and the actual disturbance. | 76 |
| Figure 3.18. Under proposed controller, (a) comparison of system frequencies with and without noise; (b) corresponding absolute error..... | 76 |
| Figure 4.1. Conceptual diagram of proposed control scheme. | 81 |
| Figure 4.2. Diagram for one single-phase two-stage PV system..... | 82 |
| Figure 4.3. Diagram of the dual-loop current mode controller..... | 84 |
| Figure 4.4. Probability distribution of the absolute percentage approximation error from MCS..... | 90 |
| Figure 4.5. LFC model including distributed PV. | 94 |
| Figure 4.6. Architecture and components of the UIO-based tracking LQR. | 96 |
| Figure 4.7. Inversion of control signals. | 98 |
| Figure 4.8. The LUT surface of $g(\Delta V_{PV}, S, T)$ for a 5695 W PV panel at 26.85 °C. | 99 |
| Figure 4.9. When $\Delta V_{PV}^a = -12.775 V$, (a) comparison of total increment power ΔP_{PV}^a ; (b) comparison of aggregate DC-link voltage ΔV_{dc}^a | 103 |

| | |
|--|-----|
| Figure 4.10. When $\Delta V_{dcref}^a = -7.730 V$, (a) comparison of total increment power ΔP_{PV}^a ; | |
| (b) comparison of aggregate DC-link voltage ΔV_{dc}^a | 103 |
| Figure 4.11. Modified WECC 9-bus system with distributed PV. | 106 |
| Figure 4.12. (a) Frequency response comparison under load disturbance; | |
| (b) Absolute error between frequencies of (i) and (ii)..... | 106 |
| Figure 4.13. For PV systems with the same rated power (200 KW), but different solar irradiance: (a) comparison of power responses; | |
| (b) correlation between steady-state ΔP_{PV} and S | 107 |
| Figure 4.14. For PV systems with the same solar irradiance ($S=70$), but different rated power: (c) comparison of power responses; | |
| (b) correlation between steady-state ΔP_{PV} and rated power..... | 108 |

CHAPTER 1 : INTRODUCTION

Frequency regulation is of vital importance to electric power system operation and stability. Under normal conditions, frequency in a large interconnected power system should be maintained within ± 0.036 Hz [1] from its nominal value, which is 60 Hz. Abnormal frequency deviations will not only affect the stability of whole power system, but also degrade the performance of load-end machines and even damage system equipment [2]. In an alternate current (AC) power system, the frequency is affected by the real power balance, which is the balance between real power generation and the demand. Any mismatches on the real power can cause deviations of system frequency from the nominal value. Therefore, maintaining proper system frequency in response to disturbances is essentially the same as maintaining the real power balance, which is achieved predominantly by the generation control of synchronous generators [3].

Nowadays, renewable energy based generation systems such as wind and photovoltaic (PV) systems are expected to grow, due to its sustainability and economic benefits. As a result, a considerable amount of conventional generation, which has been the dominant resource for controlling system frequency, is to be replaced by the renewable generation [4, 5]. Unlike synchronous generators, PV systems interface with the grid through electronic converters and thus do not possess physical inertia. In addition, as PV are normally operating at maximum power point tracking (MPPT) mode, their power output does not respond to the system frequency change [6]. Therefore, increasing penetration of PV in replacement of conventional generation will inevitably cause the loss of system frequency response capability and degrade the frequency response performance [7-12].

Therefore, enabling frequency support functions of PV systems has now become imperative. Policy-wise, many system operators and regulatory authorities around the world have

initiated grid codes or orders to ensure adequate system frequency response capability under high penetration of renewables [13-16]. Technically, lots of research have been carried out focusing on the frequency support of PV systems [17-29]. However, the existing methods from literature are still liable to two main limitations: 1) most of the methods aim at making a PV system behave like a synchronous generator and are designed based on local PV only. Therefore, the actual overall system frequency response will not necessarily be that of a desired conventional system; 2) most of the methods are proposed for large-scale PV plants and thus not suitable for distributed PV, which also share a large portion of the total penetration [30, 31] and are more difficult to manage due to the diversity among each individual units.

To address the above limitations, this paper proposes control schemes for both large-scale PV plants and distributed PV. Different from the current methods, the proposed control schemes focus on the overall system frequency response. A frequency reference is first constructed from a reference system which have the desired inertia and frequency droop constants, with the help of a disturbance observer, namely, the unknown input observer (UIO). Then, linear quadratic regulator (LQR) based controllers are designed to adjust the PV's output power to make the system frequency track the reference. By doing so, the close-loop system frequency response capability is as desired (the same as that of the reference system).

In rest of this chapter, conventional generation control scheme is first reviewed in Section 1.1. Section 1.2 discusses in detail the impact from PV integration on the generation control performance. Then, we review the state-of-art methods for frequency control methods of PV in Section 1.3. In the end, the proposed new control schemes are briefly introduced in Section 1.4.

1.1 Overview of Conventional Generation Control

1) Basic Concepts

Conventional generation control, often referred to as load frequency control, usually takes synchronous generators as the control plant with the control objective of dynamically following the system load. As mentioned, the balance of generation and load is reflected in frequency. Therefore, frequency measurement is used as an effective feedback signal to adjust generator's set-point. This feedback control scheme involves two layers of control:

- Governor at generator (primary control)
- Automatic Generation Control (AGC) at interconnection control center (secondary control)

The governor, or speed governing system, is widely implemented locally at generators. It introduces a feedback loop where the frequency deviation is measured and converted to adjustment of turbine valve position and then the mechanical power. The feedback loop contains a proportional gain $\frac{1}{R}$, where R determines the change of power output corresponding to a given change in frequency in steady-state. This relationship is called frequency droop characteristics which can be illustrated by Figure 1.1.

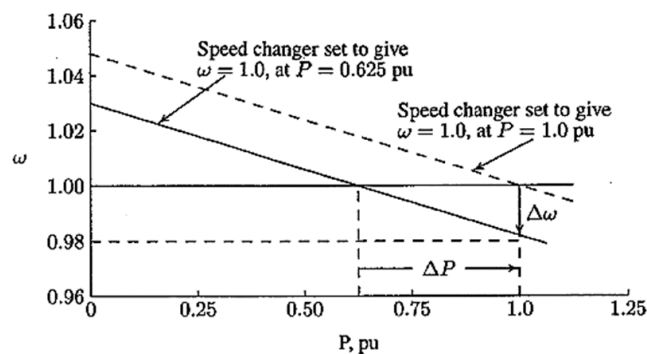


Figure 1.1. Governor steady-state frequency droop characteristics [32].

However, the generation control implemented in power system operation does not solely rely on the local governor system because of its limitations [3]:

- Cannot recover frequency to nominal value, due to its droop characteristics
- Cannot achieve economic dispatch considering generation cost
- Cannot maintain power interchange schedule between areas
- Performance is restricted by dead-bands

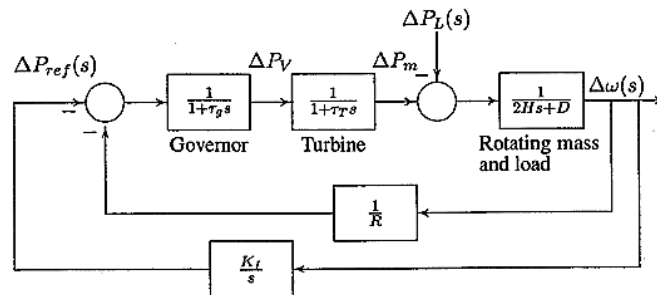


Figure 1.2. AGC control diagram for one generator [32].

To tackle the limitations of governor control, the automatic generation control (AGC) is introduced. AGC applies a reset (integral) control on top of governor to regulate the frequency. The classical type of controller, as shown in Figure 1.2, is an integral controller taking the feedback from measured frequency deviation. A more complete use of proportional, integral, and derivative (PID) controller is often utilized in practice. There are also adaptive state-space controller under research but not commonly implemented [3, 33].

AGC is a centralized control scheme as it is implemented at the control center for controlling the system within one balancing authority (BA) area. In order to adjust all generation units economically, the AGC control signal sent to each generator is proportionally scaled with corresponding participation factor [34]. In addition, the tie-line bias control incorporated to AGC can effectively maintain the power interchange schedule between different BAs. The basic idea of

tie-line bias control is to calculate a synthesized error for the integral controller. This error should contain not only the frequency deviation, but also the tie-line interchange error from its scheduled value, such that both of the errors will be eliminated. This synthesized error is referred to as area control error (ACE) and defined in Equation (1). NI_A and NI_S are the actual and scheduled net interchange (MW); f_A and f_S are the actual and scheduled system frequency. B is called frequency bias setting. The frequency bias setting is typically fine-tuned to be as close as possible to the area's frequency response, such that each area's generation only responds its own load change and the participation for external load disturbance is minimized. However, in reality, it is very difficult to obtain accurate values of areas' frequency response.

$$ACE = (NI_A - NI_S) - 10B(f_A - f_S) \quad (1)$$

2) Evaluation of Generation Control Performance

The performance of generation control is evaluated by the frequency response. Below, Figure 1.3 illustrates a frequency response to a loss of generation. People often define three periods to analyze the response curve [35]: 1) Arresting period. This is the first period for the first frequency drop, from the beginning of disturbance to the minimum frequency point; 2) Rebounding period. This period follows the end of arresting period and last till the end of first frequency swing; 3) Recovery period. This period is for when frequency eventually recovers to its nominal value. Usually, the first two periods have to be controlled within half-minute after disturbance, while the recovery period can take minutes to complete.

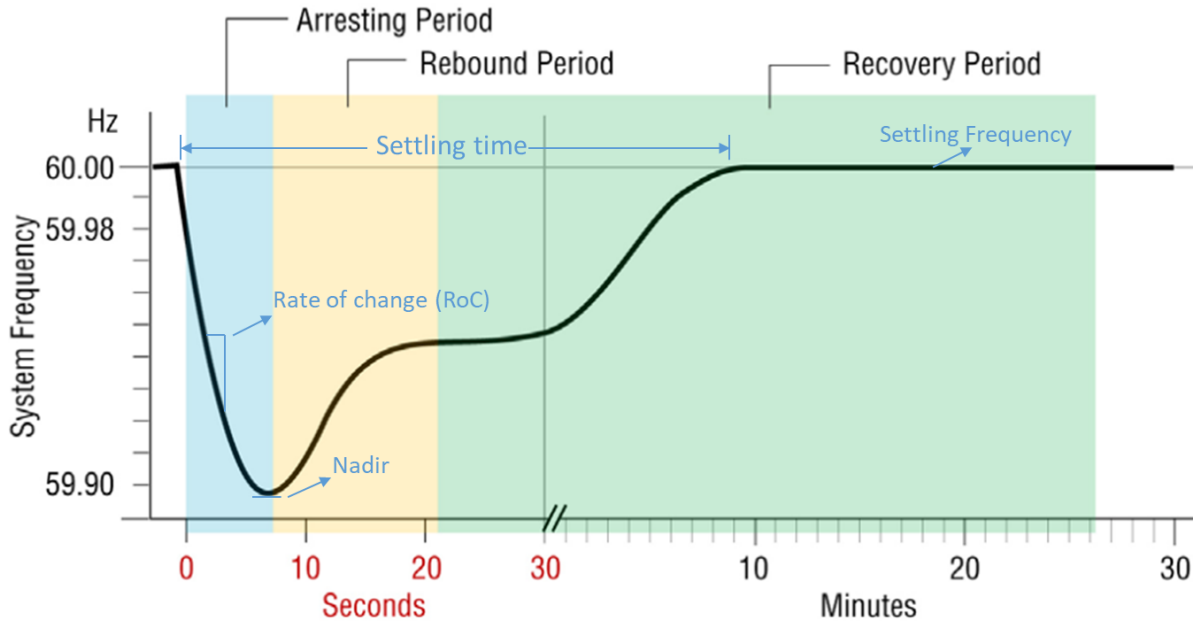


Figure 1.3. Typical frequency response to a loss of generation [35].

Some other numerical metrics are also used to evaluate the frequency response performance. Rate of change of frequency (RoCoF) describes how fast the frequency changes. This is often measured in the arresting period. Frequency nadir represents the lowest frequency value during the disturbance. Another metric is the settling time, which means the time spent for the system to recover its frequency to a steady-state value, which is the settling frequency. Referring to the control diagram in Figure 1.2, generation control performance in terms of abovementioned metrics are strongly related to the generator parameters. RoC is mainly determined by the mechanical inertia, H ; frequency nadir is greatly affected by the combination of inertia response, H , and governor response, $\frac{1}{R}$; after the frequency decline has been arrested, secondary control, AGC, will stabilize frequency at a steady-state level and then determines the settling time and frequency. However, if no AGC or other secondary control is present, the settling frequency will not be equal to the nominal frequency, which is 60 Hz.

1.2 Impacts of PV Penetration on Generation Control

In the near past, tremendous effort has been put on the integration of PV. According to [36-38], in 2015, 13.44% of domestically produced electricity in the United States is renewable energy, among which 25 GW of solar PV capacity has been installed, with an additional 1.8 GW of concentrating solar power plant. In the state of California, which is a leading state for integrating renewable energy resources and initiating renewable portfolio standards, even approximately 29% of its electricity is provided from renewable sources [39]. In addition, the penetration level of PV systems to power system continues to grow, as wind and PV generation are the fastest growing electricity resources in the United States and in the U.S. East Interconnection. The U.S. Energy Information Administration (EIA) estimates that renewable electric sources account for more than 61% of all new U.S. electricity capacity installations in 2013, up from 57% in 2008 and 4% in 2004 [40]. Study in [41] also estimates that PV generation has the potential to generate up to 40% of the nation's total electricity demand by 2030 and 27% by 2050.

PV generations are commonly interfaced with grid through power electronics. Since PV array generates direct current (DC) power and in order to transmit it to the AC grid, converters are needed. This is inherently different from conventional synchronous generators, which are electromagnetic systems. Therefore, the difference on the energy conversion technologies leads to unavoidable issues for conventional power system to accept high penetration of PV. Serious challenges can arise, especially for generation control, due to the lack of rotating inertia and governor control in common power electronics. The following discusses the impact from PV penetration on the generation control performance.

In [7], authors study the frequency response in eastern interconnection (EI) in U.S. at different penetration level of PV. It is demonstrated that the frequency RoCoF and nadir both

become worse as percentage of PV integration increases from 5% to 65%. This result is given in Figure 1.4. A similar study on the frequency response of EI is performed in [8] using an accurate dynamic EI model. The simulation results indicate that a minimum level of generation with governor-type controller must be maintained to accommodate high-level PV penetration in the system. Reference [12] investigates the impact of high PV penetration on bulk system frequency dynamics. Different than other work, the authors adopt a co-simulation approach to simulate the complete power system with details of both transmission and distribution. Simulation results also reveals negative impact of increasing PV penetration on the frequency dynamics during both generator tripping and transmission fault events. In [10], a similar study has been carried out for ERCOT system, and the results are presented in Figure 1.5. It can be seen that, for the same generator loss event, the frequency drops significantly fast and low when the PV penetration increases from 60% to 80%.

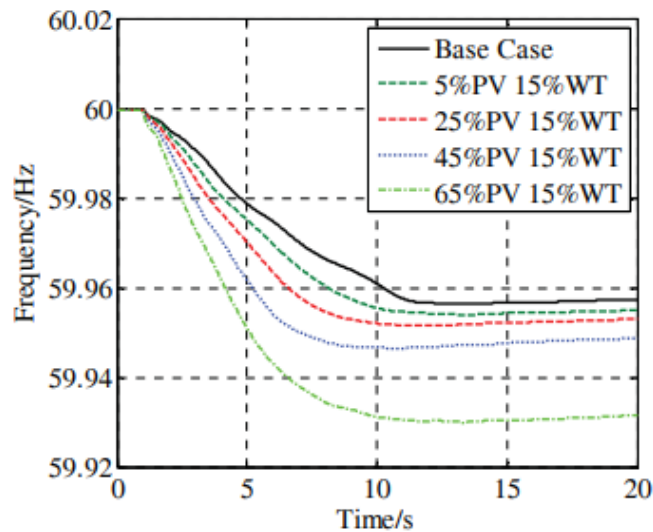


Figure 1.4. EI frequency response change due to renewable integration [7].

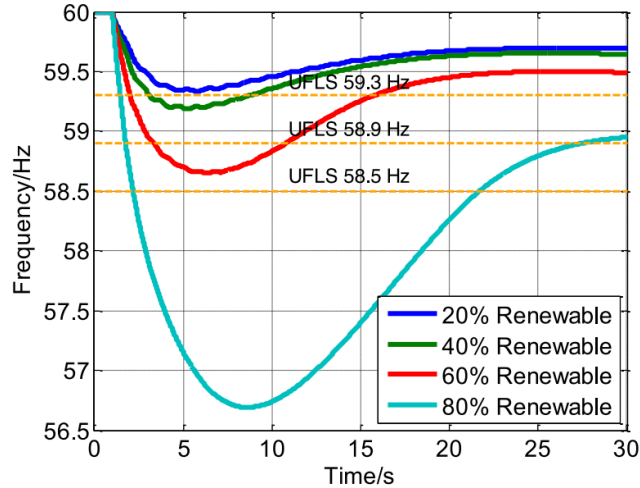


Figure 1.5. ERCOT frequency response during a 2700 MW generator loss [10].

1.3 Frequency Support Control Functions of PV

In face of the aforementioned challenges from high PV penetration on the generation control, utilizing the increasing PV generation as a resource to provide support to the system frequency during disturbances has become a great need. In this regard, globally, many system operators and regulatory authorities have initiated grid codes or orders to ensure adequate system frequency response capability under high penetration of renewables [13-16]. For example, as the issuing of FERC Order 842 [14], all new generation resources in North America connecting to the grid must equip a functioning governor or equivalent controls. Furthermore, ERCOT monitors the on-line system inertia and deploy additional resources to avoid falling below the critical inertia system operating limit [16]. Research work in [42] has also studied the minimum system inertia required by frequency control under the penetration of renewable generations.

Meanwhile, from technical perspective, lots of research have also been carried out focusing on the frequency support of PV systems. Specifically, governor-like control (frequency droop characteristic) and inertial response are the two functions within the research scope. One of the approaches is to keep PV operating in MPPT mode and equip energy storage systems (ESS) to

achieve variable power output level [17-19]. However, as discussed in [20], a more cost-effective approach is the deloading control without ESS, which is to curtail some PV generation by setting the operating point below maximum power point (MPP).

For governor-like control, authors in [21] propose a Newton quadratic interpolation (NQI) based algorithm to adjust PV system active power to a given level other than MPP. Using this algorithm, droop control is implemented to provide frequency regulation. A lookup-table method is introduced in [22] to achieve fast deloading control for higher-level functions designed for PV systems, such as droop control. Both [21, 22] address only droop control in PV systems, but no inertial response. In [23], inertia is emulated along with droop control by the deloading of PV array. However, a piece-wise linearization based dynamic resistance method is used for deloading and the linearization error is not addressed. In addition, the simulation only considers a small-islanded network. Reference [24] investigates the benefit on bulk system frequency quality from large-scale PV plants with active power reserves (APR). Both droop and inertia functions are considered. However, details about realizing APR and primary controls inside PV system are not provided. A synchronous power controller is used in [25] to make PV plants behave similarly as synchronous generators. The controller emulates inertia and droop and generates current references for inverters. Another voltage controller is designed to regulate DC-link voltage within the stable region. However, effectiveness of the voltage controller is not discussed and shown in the case studies.

Other than the deloading approach, another potential for providing frequency support is to utilize the energy stored in DC-link capacitors. Reference [26, 27] have well-studied this method for emulating inertia in wind turbine systems. Similarly, this approach is also applicable for PV and especially suitable for two-stage PV systems where the DC-link voltage is decoupled from PV array's voltage. In [28], the voltage reference for DC-link voltage control is adjusted to rapidly

release and absorb power to emulate inertial response. Separately, droop control is achieved by deloading. However, the amount of emulated inertia is very limited when solely utilizing the capacitor power. Another strategy, as introduced in [29], is to combine deloading and DC-link voltage control for inertia emulation, but droop control is not considered.

As indicated, most of the current methods aim at making PV system behave like a synchronous generator. One shortcoming is that these controller designs are based on local PV only. Thus, the actual system frequency response will not necessarily be that of a conventional system with desired equivalent inertia and droop constants, especially during the initial a few seconds. However, an accurate estimate of the frequency response capability is indeed very important to system operators in order to maintain it at a proper level. The other limitation is that, these methods only consider one single PV system or PV plants consist of identical subsystems. For distributed PV systems, however, they are different in ratings, control parameters, as well as working conditions. Applying above methods to each one will inevitably incur high communication cost and computational complexity. Thus, the preferable solution is to design one controller at the aggregator-level for a group of distributed PV while addressing their variations. To the best of authors' knowledge, literature about frequency support control methods for a group of distributed PV systems are very limited. Reference [43] presents a fuzzy controller for this purpose considering different insolation. However, the PV system model is simplified to only PV modules without control dynamics. Thus, variations among the control parameters are neglected.

1.4 Proposed Control Schemes for Distributed PV

To overcome the above limitations in previous work, we first propose a novel frequency support controller for large-scale PV plant, whose objective is to control the PV power output such that, under a unknown load disturbance, the system frequency response can effectively track that

of a reference system with desired equivalent inertia and droop constants which are provided by the system operators. This objective implies that, by closely following the reference system frequency with the help of proposed controller, the frequency response of the whole system (close-loop system) will be improved to as desired, i.e. close to that of the reference system. Since we only focus on improving the primary frequency response performance, secondary generation control, e.g. AGC, is not considered in this work.

In addition to the controller design, we also propose a small-signal model (SSM) for large-scale PV plant. The model is different than other models from [23, 44-47] in that, it does not only

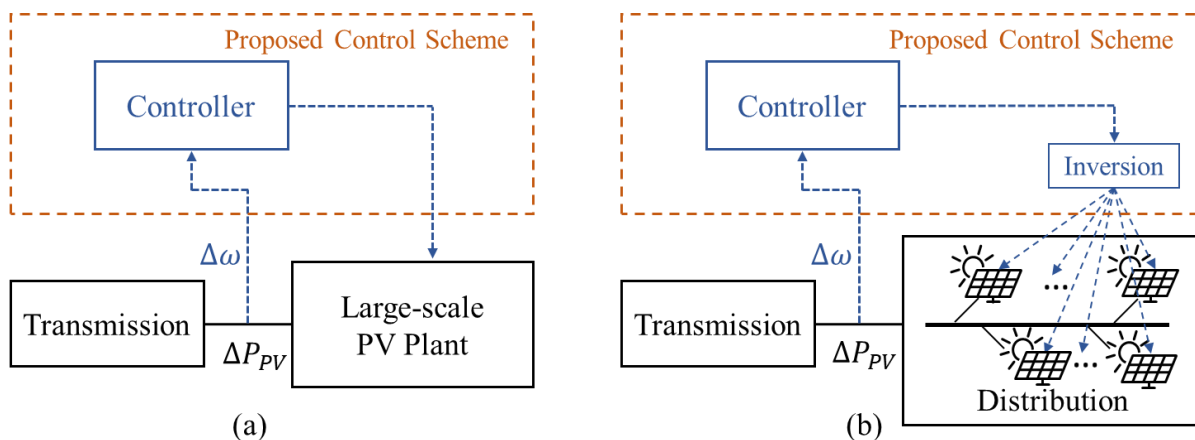


Figure 1.6. Diagrams for proposed control schemes for (a) large-scale PV plant; (b) distributed PV.

consider full dynamics including PV array, DC-link, and converter control, but also incorporates control inputs with which PV system output power can be controlled. We then interface this SSM for PV plants with the load frequency control (LFC) model to form a combined system model which can describe the dynamic relationship between PV system input and system frequency. The combined system model is then used as the plant model for designing proposed controller.

To address the frequency support functions from distributed PV, we propose an aggregate model to represent the overall dynamic behaviors of a group of distributed PV with different

control parameters, solar irradiance, and capacity. Then, we adopt the proposed controller for large-scale PV plant and extend it to distributed PV by using the aggregate model and proposing an inversion method. The inversion method aims at obtaining the individual control input for each distributed PV from the controller's aggregate control signal. The control schemes for both cases: large-scale PV plant and distributed PV are illustrated in Figure 1.6.

The rest of this thesis is organized as follows: Chapter 2 focuses on the evaluation of high PV penetration impact on frequency response. In Chapter 3, we present the proposed control scheme for large-scale PV plants. Chapter 4 introduces the control scheme for distributed PV. Chapter 5 summarizes the contributions of this work and discusses the future work.

CHAPTER 2 : IMPACT OF HIGH PV PENETRATION ON FREQUENCY RESPONSE

As discussed in Chapter 1, the increasing penetration of PV is placing great impact on power system stability, especially in terms of generation control performance. From the basic concepts of power system operation, we also learned that frequency response can be used to evaluate the generation performance with several numerical metrics, such as frequency nadir, RoC, and settling time. In this chapter, we present the detailed results to demonstrate and evaluate the high PV penetration impact on frequency response. Section 2.1 introduces three methods to model a single-phase PV system. Using these methods, one small and one large testbed are developed in Section 0. Simulations are then carried out to evaluate the impact of high PV penetration on frequency response. Section 2.3 is for the simulation results and discussion.

2.1 PV Modeling

The proposed control schemes focus on both large-scale PV plant which mainly consists of three-phase PV systems, and distributed PV which are mainly single-phase. Since modeling of both types of PV systems are very similar and distributed single-phase PV systems are slightly more complex, we choose to model distributed PV in our testbed and thus introduce the three corresponding modeling methods in this chapter, which are average model, 2-dq average model, and PVD1 model. Models for three-phase systems can be easily obtained following the presented methods with minor changes.

2.1.1 Average Model

In Figure 2.1, the diagram for a two-stage single-phase PV system is illustrated. The PV system contains multiple PV arrays as the energy source. A two-stage power conversion stage has one DC-DC boost converter and one single-phase inverter. The adoption of boost converter can effectively adjust PV array's output voltage, such that appropriate level of DC voltage can be

guaranteed and provided for inverter. Another advantage of two-stage topology over single-stage is that the control of PV array's operating point can be separated from DC-link control. After the inverter, a simple R-L filter is modeled to interface with the distribution system. Another component, which is not illustrated in the diagram is the phase-lock loop controller. In the scope of this work, we assume an ideal PLL and do not model it with any dynamic details. Other controllers also include an MPPT controller and an inverter controller. The MPPT controller considered here uses the classical perturb & operate algorithm in [48]. The controller at inverter has one outer voltage loop and one inner current loop. Additional decoupling compensation is applied in the current loop to decouple the inverter current control from network and interfacing filter. The goal of this inverter controller is to regulate the DC-link voltage.

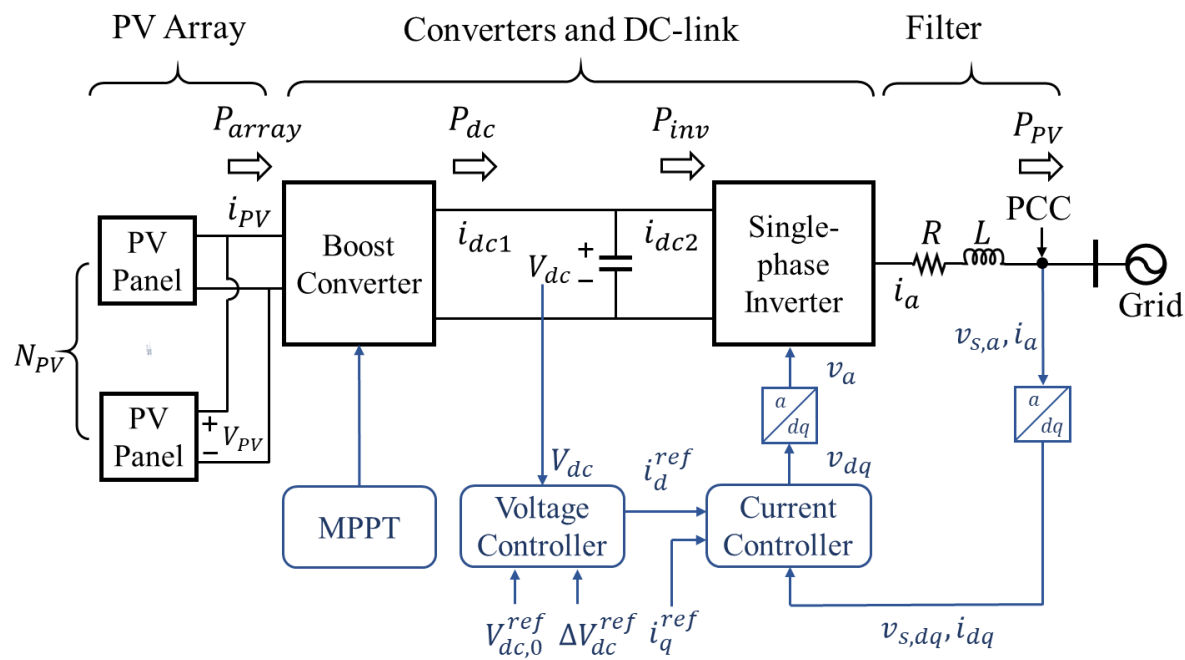


Figure 2.1. Diagram for a two-stage single-phase PV system.

1) PV array

The PV array is described by its current-voltage characteristic function from [48].

$$i_{PV} = N_{PV}n_p I_{ph} - N_{PV}n_p I_{rs} \left(e^{\frac{q}{kTA} \frac{v_{PV}}{n_s}} - 1 \right) \quad (2)$$

where N_{PV} is the number of PV panel connected in parallel, I_{rs} is the reverse saturation current of a $p - n$ junction, q ($= 1.602 \times 10^{-19}C$) is the unit electric charge, k ($= 1.38 \times 10^{-23}J/K$) is Boltzman's constant, T is the $p - n$ junction temperature in (in Kelvin), A is the ideality factor, and I_{ph} is the short-circuit current of one string of the PV array, I_{ph} , a function of the temperature, is a linear function of the solar irradiation level S , as

$$I_{ph} = [I_{scr} + k_T(T - T_r)] \frac{S}{100} \quad (3)$$

where T_r is the cell reference temperature, I_{scr} is the short-circuit current of one PV cell at the reference temperature and irradiation level, and k_T is a temperature coefficient. Based on Equation (2), the power delivered by the PV array can be expressed as:

$$\begin{aligned} P_{array} &= N_{PV}f(v_{PV}, S, T) = N_{PV}i_{PV}v_{PV} \\ &= N_{PV}n_p I_{ph}v_{PV} - N_{PV}n_p I_{rs}v_{PV} \left(e^{\frac{q}{kTA} \frac{v_{PV}}{n_s}} - 1 \right) \end{aligned} \quad (4)$$

2) DC-DC Boost Converter and DC-link

Figure 2.2 shows the equivalent circuit of the DC-DC boost converter and the DC-link capacitor. Here we assume the converter to be lossless and use the average model to avoid switching details. The duty cycle is not explicitly expressed in this model and we assume the PV array voltage, v_{PV} , can be directly controlled by controller such as MPPT controller. However, limitation has to be placed on the duty cycle such that it does not exceed one.

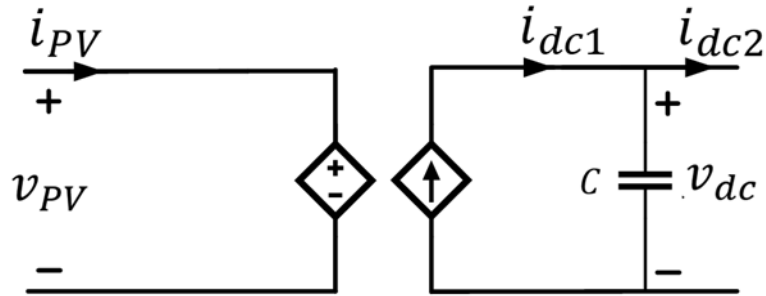


Figure 2.2. Equivalent circuit of DC-DC converter and DC-link.

The average model can be described by Equations (5) and (6).

$$i_{PV}v_{PV} = i_{dc1}v_{dc} \quad (5)$$

$$\frac{dv_{dc}}{dt} = \frac{1}{C}(i_{dc1} - i_{dc2}) \quad (6)$$

3) Inverter

Figure 2.3 plots the equivalent circuit for the single-phase inverter, along with the output filter. Similarly, to the converter model, the inverter is modeled as a lossless inverter without switching detail. A simple power balance equation in Equation (7) is used for the average model. In this inverter model, i_{ac} is treated as the control input.

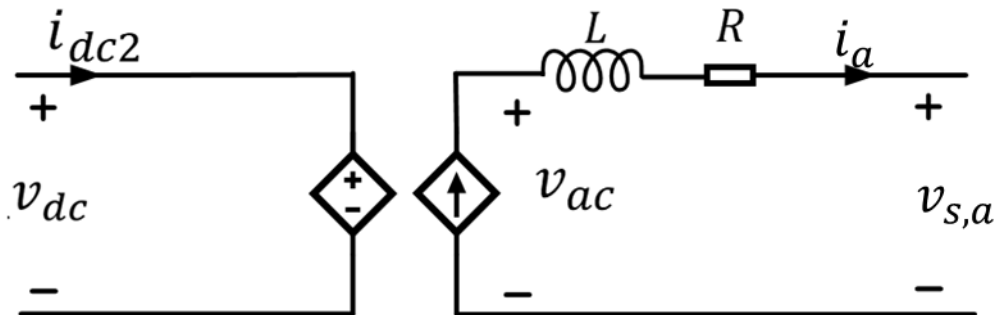


Figure 2.3. Equivalent circuit of DC-AC inverter and output filter.

$$i_{dc2}v_{dc} = i_a v_{ac} \quad (7)$$

4) Filter

In this case, we consider a simple $R - L$ output filter to eliminate the harmonics from inverter to the grid. The filter can be modeled by Equations (8) and (9) in d-q frame. The reason of using d-q components is that the inverter control is based in d-q frame as later introduced.

$$L \frac{di_{a,d}}{dt} = v_{ac,d} - v_{s,d} - Ri_{ac,d} + L\omega i_{a,q} \quad (8)$$

$$L \frac{di_{a,q}}{dt} = v_{ac,q} - v_{s,q} - Ri_{a,q} - L\omega i_{a,d} \quad (9)$$

5) PLL

An ideal PLL is shown in Figure 2.4. For simplicity, we do not model the PLL dynamics. Therefore, in our modeling of PV system, the transformation between d-q and abc frame is directly available without any dynamics. Since the transformation is for single-phase, the signal delay method [49] is used where the abc component has to be delayed by $\frac{\pi}{2}$, which is $\frac{1}{4}$ of its period. The transformation matrices between single-phase and d-q components are in Equation (10) and (11). The specific transformations associated with PLL in this PV system model are shown in Equation (12) - (14).

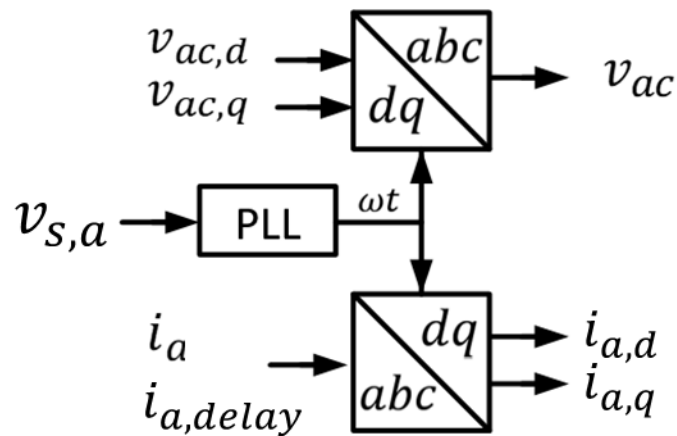


Figure 2.4. Diagram for an ideal PLL.

$$\begin{bmatrix} x_d \\ x_q \end{bmatrix} = \begin{bmatrix} -\sin(\omega t) & \cos(\omega t) \\ \cos(\omega t) & \sin(\omega t) \end{bmatrix} \begin{bmatrix} x \\ x_{delay} \end{bmatrix} \quad (10)$$

$$\begin{bmatrix} x \\ x_{delay} \end{bmatrix} = \begin{bmatrix} -\sin(\omega t) & \cos(\omega t) \\ \cos(\omega t) & \sin(\omega t) \end{bmatrix} \begin{bmatrix} x_d \\ x_q \end{bmatrix} \quad (11)$$

$$i_{a,d} = -\sin(\omega t) i_a + \cos(\omega t) i_{a,delay} \quad (12)$$

$$i_{a,q} = \cos(\omega t) i_a + \sin(\omega t) i_{a,delay} \quad (13)$$

$$v_{ac} = -\sin(\omega t) v_{ac,d} + \cos(\omega t) v_{ac,q} \quad (14)$$

6) Inverter Control

An inverter controller with one outer voltage loop and one inner current loop is considered in this model and illustrated by the diagram in Figure 2.5. The control objective of this inverter controller is to regulate the DC-link voltage at its reference value, such that any amount of power generated from PV array can be stably delivered to the grid. In the outer voltage loop, DC-link voltage, v_{dc} , is measured and compared with the given reference, v_{dc}^{ref} . The voltage error is sent to a classical PI controller. The output from PI controller is taken as the reference value for $i_{a,d}$, which is the d-axis component of inverter output current, i_a .

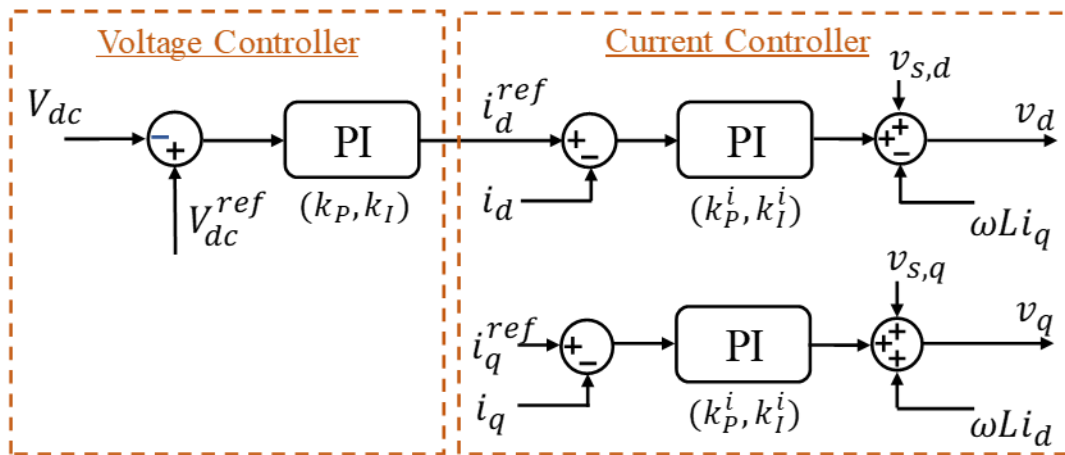


Figure 2.5. Control diagram of inverter controller.

As mentioned in early sections, the current loop control is realized in d-q frame. Therefore, two independent PI controllers are utilized to regulate $i_{a,d}$ and $i_{a,q}$ to their references, respectively. In our scope, since no reactive power control function is considered, the reference for $i_{a,q}$ is set to be zero to eliminate reactive power generation. After the PI controllers, decoupling compensation is adopted to decouple the current control of $i_{a,d}$, $i_{a,q}$ from network disturbance. The final control output after the compensation are the d-q components of inverter output voltage, v_{ac} . Again, we assume the reference values for $v_{ac,d}$ and $v_{ac,q}$ can be achieved ideally without considering any switching detail. In this controller, v_{dc}^{ref} is also an input where higher-level controller can adjust the nominal value of DC-link voltage. This controller can be analytically modeled by Equation (15) - (17).

$$i_{a,d}^{ref} = (v_{dc}^{ref} - v_{dc}) \left(K_P + \frac{K_I}{s} \right) \quad (15)$$

$$v_{ac,d} = (i_{a,d}^{ref} - i_{a,d}) \left(K_P^i + \frac{K_I^i}{s} \right) + v_{s,d} - L\omega i_{a,q} \quad (16)$$

$$v_{ac,q} = (i_{a,q}^{ref} - i_{a,q}) \left(K_P^i + \frac{K_I^i}{s} \right) + v_{s,q} + L\omega i_{a,d} \quad (17)$$

Considering the filter equations (8) and (9), the inverter current $i_{a,d}$ and $i_{a,q}$ are affected by network variables such as $v_{s,d}$, $v_{s,q}$, $L\omega i_{a,q}$, and $L\omega i_{a,d}$. Therefore, other than the controller terms, the additional compensation terms in Equation (16) and (17) can help decouple the inverter current control from distribution network. The resulted current control equations considering the interfacing filter are described by Equations (18) and (19).

$$L \frac{di_{a,d}}{dt} = (i_{a,d}^{ref} - i_{a,d}) \left(K_P^i + \frac{K_I^i}{s} \right) - R i_{a,d} \quad (18)$$

$$L \frac{di_{a,q}}{dt} = (i_{a,q}^{ref} - i_{a,q}) \left(K_P^i + \frac{K_I^i}{s} \right) - R i_{a,q} \quad (19)$$

In order to further decouple the current control from the interfacing filter resistor, [47] proposes a method where the PI controller parameters, K_P^i and K_I^i , can be carefully set as follows to eliminate the filter terms in Equation (18) and (19).

$$K_P^i = \frac{L}{\tau} \quad (20)$$

$$K_I^i = \frac{R}{\tau}$$

where τ is the time-constant, which should be made sufficiently small for a fast current control response. Now the close-loop transfer function of the d- and q-axis current controller become in the simple first-order form:

$$\frac{i_{a,d}(s)}{i_{a,d}^{ref}(s)} = \frac{i_{a,q}(s)}{i_{a,q}^{ref}(s)} = G(s) = \frac{1}{\tau s + 1} \quad (21)$$

Note that, in Equation (21), the dynamics of $i_{a,d}$ and $i_{a,q}$ are now completely decoupled from those of ω , $v_{s,d}$, $v_{s,q}$, R , and L . However, the reference for $i_{a,d}$ is generated from voltage-loop controller. Therefore, we can write the complete state-space equations for the voltage- and current-loop controller, considering the filter dynamics, as:

$$\frac{di_{a,d}}{dt} = -\frac{1}{\tau} i_{a,d} - \frac{K_P}{\tau} v_{dc} + \frac{1}{\tau} x + \frac{K_P}{\tau} v_{dc}^{ref} \quad (22)$$

$$\frac{di_{a,q}}{dt} = -\frac{1}{\tau} i_{a,q} + \frac{1}{\tau} i_{a,q}^{ref} \quad (23)$$

$$\frac{dx}{dt} = -K_I v_{dc} + K_I v_{dc}^{ref} \quad (24)$$

Because the final model contains second-order derivatives, an intermediate state x is introduced to construct the state-space form.

7) MPPT

The MPPT controller controls the input voltage of the DC-DC converter to operate PV arrays at their MPP. In this work, we use the most commonly used MPPT algorithm which is the P&O from [48]. A flowchart for this algorithm is illustrated in Figure 2.6. v_{ref} is the reference for v_{pv} and Δv_{ref} is the increment for the adjusting v_{pv} .

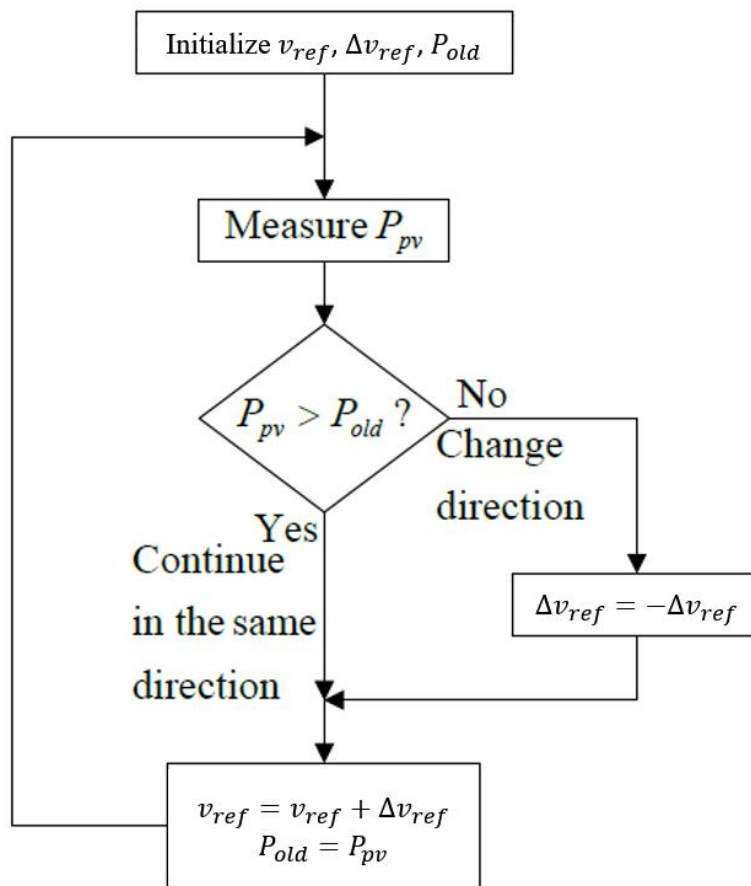


Figure 2.6. Flowchart of the P&O algorithm in MPPT controller.

2.1.2 2-dq Average Model

A modeling method for single-phase single-state PV systems is proposed in [50] to eliminate the second-order harmonics in the inverter control and obtain linearized model. Here we extend this method to single-phase two-stage PV systems.

This method is based on multiple reference frame theory, where in addition to the reference frame at the fundamental grid frequency ω , another reference frame at 2ω is considered. Specifically, the single-phase d-q transformation at frequency ω is given in Equation (25). Therefore we can similarly obtain the d-q transformation at 2ω in Equation (26).

$$x = -\sin(\omega t)x_d + \cos(\omega t)x_q \quad (25)$$

$$x = -\sin(2\omega t)x_{2d} + \cos(2\omega t)x_{2q} \quad (26)$$

The derived model uses the same system topology as introduced in Section 2.1.1. Consider the inverter equation (7), if we substitute i_{ac} and v_{ac} with their d-q components, the inverter input current i_{dc2} can be expressed by:

$$\begin{aligned} i_{dc2} = \frac{1}{2v_{dc}} & (i_{ac,d}v_{ac,d} + i_{ac,q}v_{ac,q} \\ & + \cos(2\omega t)(i_{ac,d}v_{ac,d} - i_{ac,q}v_{ac,q}) \\ & - \sin(2\omega t)(i_{ac,d}v_{ac,q} + i_{ac,q}v_{ac,d})) \end{aligned} \quad (27)$$

Equation (27) implies that i_{dc2} also contains harmonic components at the frequency of 2ω . Comparing (27) with (26), we can categorize i_{dc2} into two components:

1) DC Component

$$i_{dc2,dc} = \frac{i_{ac,d}v_{ac,d} + i_{ac,q}v_{ac,q}}{2v_{dc}} \quad (28)$$

2) AC Components at 2ω

$$i_{dc2,2d} = \frac{i_{ac,d}v_{ac,q} + i_{ac,q}v_{ac,d}}{2v_{dc}} \quad (29)$$

$$i_{dc2,2q} = \frac{i_{ac,d}v_{ac,d} - i_{ac,q}v_{ac,q}}{2v_{dc}} \quad (30)$$

Since the inverter model is now modeled in the reference frame of 2ω , so must the DC side of the system. Because of the DC component in i_{dc2} , the DC side variables of boost converter and PV array should be converted into the form of (31), instead of (26). Then the rest of the system can be modeled by equating the DC and 2ω components, respectively. For the PV array, since it is an algebraic model and v_{PV} are usually controlled by DC reference signal, we assume that v_{PV} and i_{PV} only have DC components. In addition, all the higher-order terms, harmonics at 3ω and 4ω , are ignored. The inverter control introduced in Section 2.1.1 can still be applied in this model since the inverter output voltage and current are still modeled in d-q frame at ω .

$$x = x_{dc} - \sin(2\omega t)x_{2d} + \cos(2\omega t)x_{2q} \quad (31)$$

For the benefit of linearization, this model also aims at removing the time-varying terms. Therefore, special treatment has to be taken on the $\frac{1}{v_{dc}}$ term in Equation (28) - (30), because v_{dc} is also in the form of (31) and has adds time-varying *sine* terms. A simple solution is to use $v_{dc,dc}$ to approximate v_{dc} in (28) - (30).

Complete model equations are provided in Appendix I.

2.1.3 PVD1 Model

We use a modified version of the PVD1 [51] model to represent the single-phase PV plants. The original PVD1 model is for three-phase PV system but in our case, we can easily adopt it as single-phase PV system because this model eventually interfaces with grid by power injection, which is not phase-specific. As shown in Figure 2.7, the PVD1 model includes the constant active and reactive power reference and d-q current controllers with limiters. The current controller has

the same first-order transfer function as the one introduced in Section 2.1.1 for the current control with decoupling compensation. The time constant here, T_g , is equivalent to the aforementioned time constant τ . The current limits are determined based on the selected priority mode. For example, if it is in “P Priority” mode, the active current reference, I_{pcmd} , is firstly satisfied without exceeding the composite current limit I_{max} . The reactive current limit is then calculated based on I_{max} and the desired I_{pcmd} . Based on the original PVD1 model, the frequency trip function is not considered and the voltage trip function is revised with the low-voltage-ride-through (LVRT) characteristics, as per the IEEE 1547-2018 standard [52].

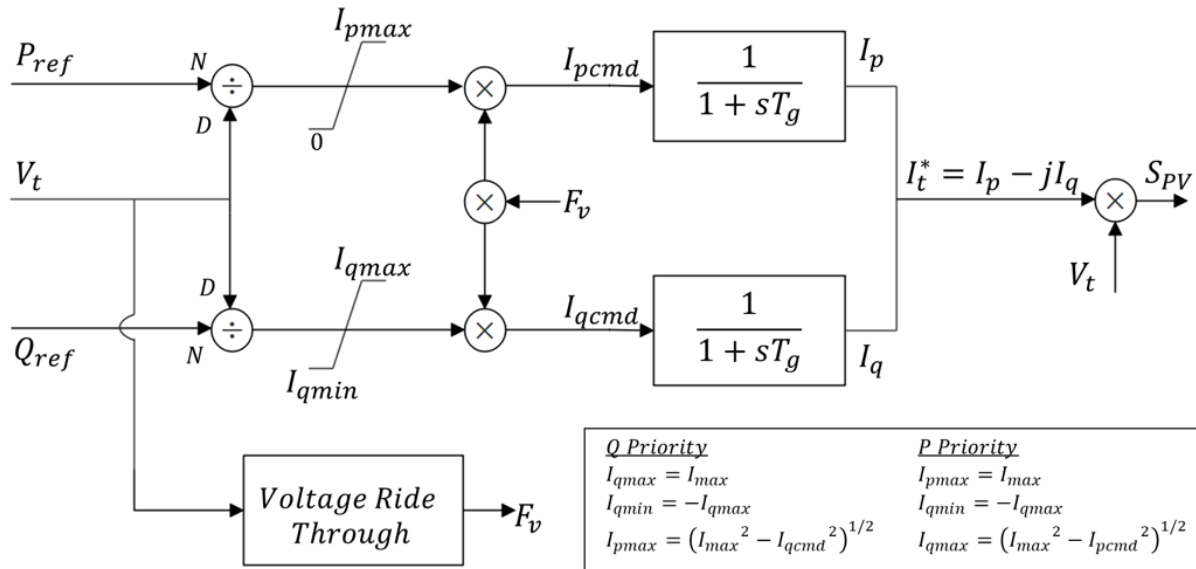


Figure 2.7. Diagram for the modified PVD1 model.

Comparing to the other two PV models, this PVD1 model simplified the dynamics a lot by ignoring the PV array’s characteristics and even the DC-link. However, this model is the most advantageous for its simplicity and ease to implement in simulations.

2.1.4 Comparison of PV Models

In this section, we want to compare the three PV models in above with their advantages and disadvantages. A summary for the comparison is provided in Table 2.1.

Table 2.1. A Comparison Summary of PV Models.

| PV Model | Advantages | Disadvantages |
|--------------------------|--|--|
| Average Model | <ul style="list-style-type: none"> • PV array characteristics • Moderate number of equations • Easy to simulate | <ul style="list-style-type: none"> • Time-variant |
| 2dq Average Model | <ul style="list-style-type: none"> • PV array characteristics • Time-invariant | <ul style="list-style-type: none"> • More dynamics • Too many equations • Computationally expensive |
| PVD1 | <ul style="list-style-type: none"> • Least number of equations • Easiest to simulate | <ul style="list-style-type: none"> • Less dynamics • No PV array |

The average model has the advantages over accuracy as it models the PV array in detail. The number of both dynamic and algebraic equations contained in this model is not too large. The only disadvantage is that there are time-variant terms in the model which are not favorable for obtaining the small-signal model. Similarly, the 2dq model also has the advantage on accuracy. In addition, as modified from the average model, it removes the time-variant terms. However, as the price in return, this model introduces additional dynamic states and equations and therefore becomes computationally expensive to simulate. The last PVD1 model has the least number of equations which make it easiest to simulate. However, it sacrifices the accuracy by only modeling the inverter control dynamics and ignoring both PV array characteristics and DC-link dynamics.

2.2 Testbed Development

In this section, we introduce the development of two testbeds: PSCAD testbed and dynamic co-simulation testbed. The developed testbeds are used to evaluate the high PV penetration impact on frequency response and demonstrate the effectiveness of designed control scheme. The two testbeds are based on different simulation platforms. The test systems are also different in size. Section 2.2.1 and 2.2.2 detail the testbed and their test systems, respectively.

2.2.1 PSCAD Testbed

This testbed is developed in the commercial electro-magnetic transient program (EMTP) PSCAD [53]. PSCAD is an industry standard simulation tool for studying the transient behavior of electrical networks. In this testbed, we first model the single-phase PV system as a controlled voltage source. As shown in Figure 2.8, the v_{ac} is controlled by the average model Equations (2), (3), (5) - (7), (12) - (14), (22) - (24). An R-L filter is placed in between the voltage source and distribution grid. The values of R and L are also used in designing the inner current-loop controller of the average model.

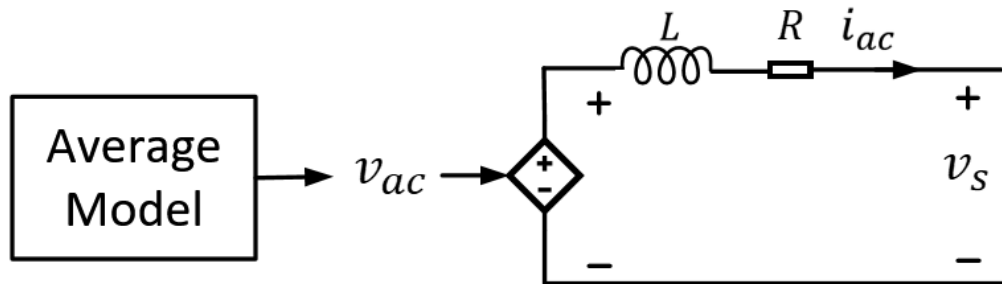


Figure 2.8. PV model in PSCAD testbed.

The IEEE 34-bus test feeder [54] is used to model the distribution system. Seven buses at different locations are selected to connect PV systems. To demonstrate the impact of PV integration on the frequency response, we also need to model the transmission system which has the synchronous generators. However, since the electro-magnetic transient simulation for large-

system is too time-consuming, we do not model the complete transmission and distribution systems. For distribution, we only model one representative test feeder in detail; for transmission, we scale down the system rating to be comparable to the representative test feeder and, instead of modeling the network detail, model only one equivalent synchronous generator. The schematic diagram for our test system is illustrated in Figure 2.9.

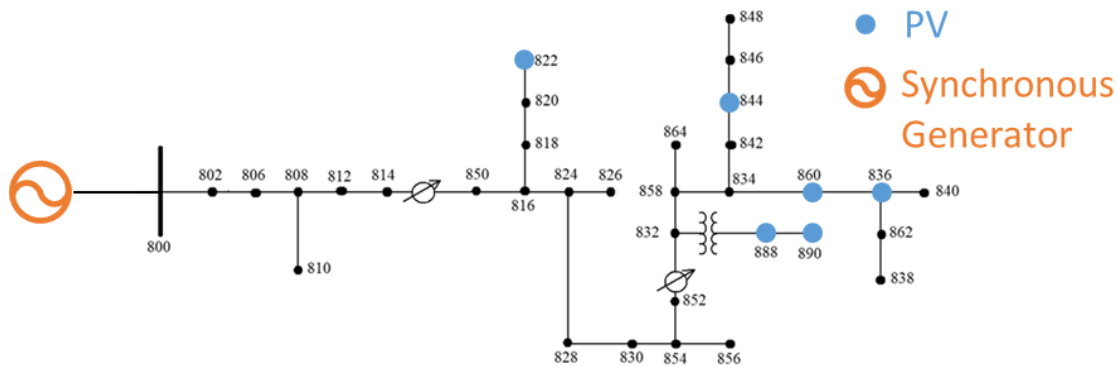


Figure 2.9. Distribution test system connected to an equivalent synchronous generator.

Different amount of PV are connected to the test feeder to simulate different levels (0%, 40%, and 60%) of PV penetration. Meanwhile, the locations are kept the same as the seven marked buses in Figure 2.9. It is also assumed that, as the PV penetration increases, the synchronous generation capacity decreases, correspondingly. This is implemented by proportionally scaling down the power rating of equivalent synchronous generator but keeping the per-unit inertia constant the same. The same event of a 0.3 MW load increase is applied to scenario with each PV penetration level. Details of the system configuration can be found in Appendix II.

2.2.2 Dynamic Co-simulation Testbed

The testbed based on PSCAD can perform detailed electro-magnetic transient simulation to demonstrate the dynamic behavior and impact of high PV penetration in distribution systems. However, this testbed is not suitable for time-efficient large system simulation. Therefore, as the compromise, the complete transmission-distribution system has to be greatly simplified. Only one

representative distribution feeder is simulated and the transmission system is modeled by an equivalent synchronous generator. To overcome these limitations, another testbed is developed using a dynamic co-simulation method which can simulate the dynamics of both transmission and distribution systems in detail. The test systems also upgrade to a 14-bus transmission system and IEEE 8500 node test feeders.

1) Co-simulation Framework

In this co-simulation testbed, we use separate transmission system simulator (TSS) and distribution system simulator (DSS). To link the TSS and DSS, we use the Hierarchical Engine for Large-Scale Infrastructure Co-simulation (HELICS) as the framework to exchange information and manage the time synchronization. HELICS [55] is an open-source tool that facilitates the co-simulation of heterogeneous simulators and provides message-exchanging and time-synchronization mechanisms. It can be used with a number of message-passing protocols including ZeroMQ, Sockets, TCP/IP, and MPI. The platform is portable across Windows, Linux, and MacOS, and users can write their co-simulation applications either in C++, C, Python, JAVA, or MATLAB. With a modular framework and an easy-to-use interface, HELICS provides the basic building blocks for co-simulation of transmission, distribution, and communication.

2) System Modeling

As studied and documented in literature, the power system can be mathematically modeled as a set of differential algebraic equations (DAEs) [56]. The differential equations represent dynamic components like synchronous generators and electronic converters while the algebraic equations model other static components and the coupling among these components which is the system network. Therefore, the nature of power system dynamic simulation is solving the set of DAEs with given initial conditions to obtain the time evolution

of interested states. Specifically, the transmission system model can be represented by equations (32) - (33) and we can also model the distribution system in the form of equations (34) - (35).

$$\dot{x}_T = f_T(x_T, y_T, u_T) \quad (32)$$

$$0 = g_T(x_T, y_T, u_T) \quad (33)$$

$$\dot{x}_D = f_D(x_D, y_D, u_D) \quad (34)$$

$$0 = g_D(x_D, y_D, u_D) \quad (35)$$

As stated earlier, separate TSS and DSS are used for transmission and distribution simulations. The HELICS framework and the federation scheme enable synchronized interactions between the simulation instances to achieve co-simulation. For TSS, the lump load should no longer be preset and fixed; instead, it should reflect the dynamic behaviors of distribution feeders. This can be accomplished by updating the bus load power, u_T , with the total power of corresponding feeders calculated from the simultaneous distribution simulation. On the other side, for DSS, the magnitude and angle of substation voltage, u_D , need to be synchronized with the calculated values from TSS throughout the co-simulation. Hence, every load bus that is to be replaced by distribution feeders is treated as a boundary bus and its voltage and load power become the boundary variables. The consistency of boundary variables for TSS and DSS are referred to as boundary conditions. They can be represented by equations (36) and (37) for transmission and distribution systems, respectively:

$$0 = h_T(u_T, r(y_D)) \quad (36)$$

$$0 = h_D(u_D, s(y_T)) \quad (37)$$

where,

$$r(y_D) = S_{T,+} \quad (38)$$

$$s(y_T) = V_{D,abc} \quad (39)$$

$S_{T,+}$ is the positive sequence apparent power of the boundary bus and $V_{D,abc}$ is the three-phase voltage of the distribution substation bus. Transformation between the positive sequence and three-phase is carried out in (38) and (39) because TSS runs a positive sequence simulation and DSS is a three-phase simulator. The transmission and distribution system models described in equations (32) - (35), along with two boundary conditions, equations (36) - (37), complete the modeling of our dynamic co-simulation.

3) Interfacing Algorithm

The goal of the proposed algorithm is to ensure the boundary conditions are met during the information exchange between TSS and DSS. The interfacing algorithm, as illustrated in Figure 2.10, is an iterative algorithm. At every time-step, the DAEs for the transmission and distribution systems are separately computed with the inputs from last time-step. The boundary condition for DSS, $0 = h_D$, is firstly solved to publish $s(y_T)$ to DSS and update the substation voltage u_D . Then DSS will re-compute the distribution power flow with the new input. However, for the sake of simulation speed, only algebraic equations (35) are solved. Afterwards, the updated values of y_D are used to calculate $r(y_D)$ and then the new transmission input u_T is subscribed from DSS by solving the other boundary condition (37). Next, the transmission algebraic states are updated. To ensure the boundary conditions are well-satisfied, the steps of solving algebraic equations in both TSS and DSS are repeated until the 2-norm of $h_D(u_D, s(y_T))$ is less than ϵ .

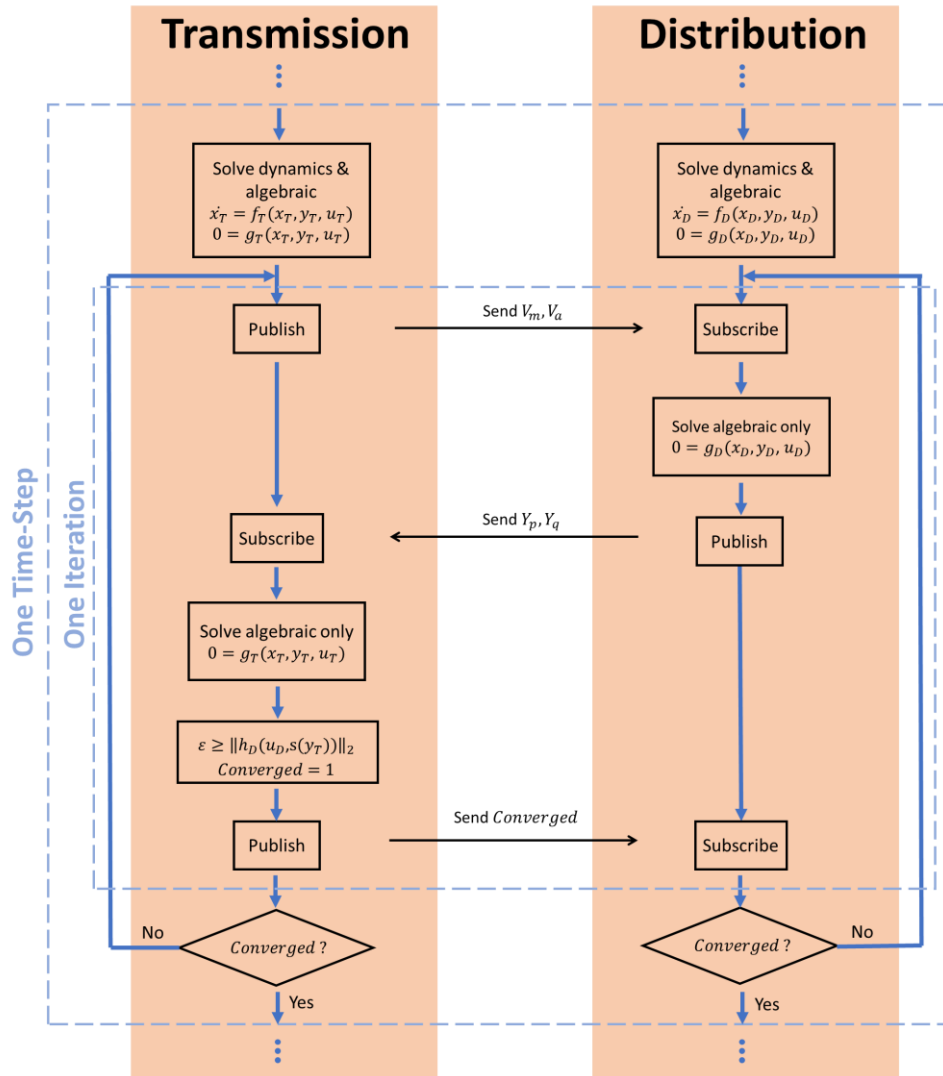


Figure 2.10. Flowchart for the interfacing algorithm.

4) Transmission System Simulator

The transmission dynamic simulator used in this work is the Dynamic Security Analysis Toolkit (DSAT) package that simulates the fundamental frequency phasor dynamics of the power grid. DSAT is a high-performance parallel package that uses the portable, extensible toolkit for scientific computation (PETSc) [57] package as its numerical core. The detailed description of DSAT's modeling and algorithmic capabilities can be found in [58].

5) Distribution System Simulator

The distribution system simulator used in this work is based on open-source OpenDSS software [59] interfaced with PV systems modeled by the dynamic PVD1 model. As illustrated in Figure 2.11, the PV system is modeled as an OpenDSS generator component in static simulation mode. The generator's output power are completely determined by the PVD1 model.

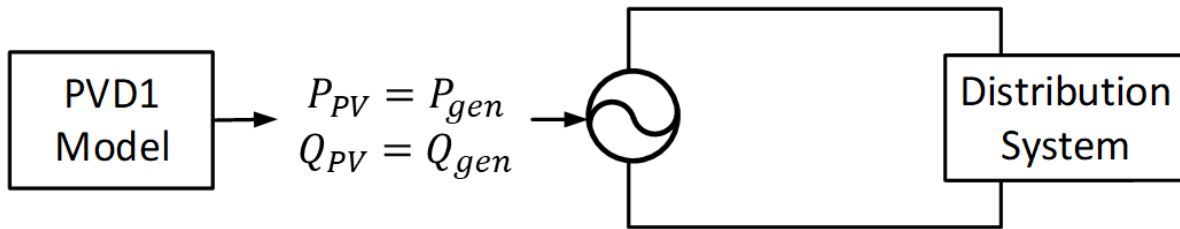


Figure 2.11. PV model in the dynamic co-simulation.

To interface the PVD1 dynamics (differential) equations with steady-state OpenDSS equations, we use a non-intrusive approach to add the dynamics on top of OpenDSS. This is akin to an alternating-explicit approach for solving DAEs where the differential equations are numerically integrated followed by the solution of the algebraic equations. For the numerical integration of the PV model differential equations, we use the PETSc package and its second-order Runge-Kutta method, which is the same as the trapezoidal integration scheme. As illustrated in Figure 2.12, the static components and system network are modeled in an OpenDSS circuit, while the dynamic component, PV, is modeled by the set of differential equations in a standalone separate code that uses the PETSc package. PETSc controls the time-stepping and performs the numerical integration of the PV differential equations, while OpenDSS solves the distribution power flow. The OpenDSS power flow solution is solved repeatedly to ensure the boundary conditions for PV bus voltage and power are consistent.

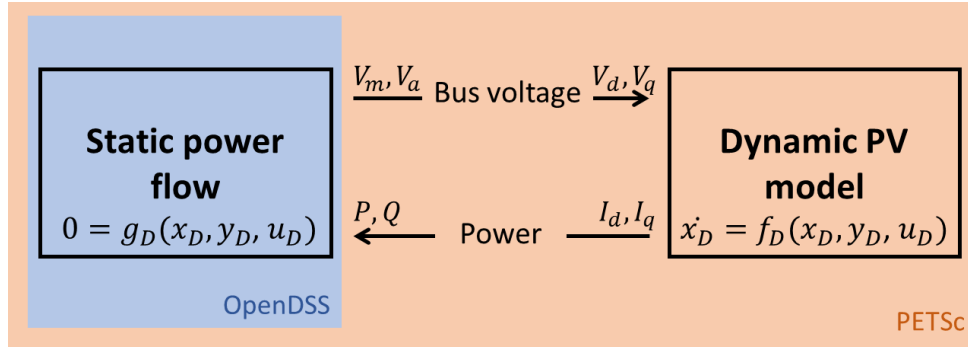


Figure 2.12. Distribution dynamic simulation using OpenDSS and PETSc.

6) Test Systems

The test system for transmission is the IEEE 14 bus system. Figure 2.13 shows the topology of this test system where 7 boundary buses are selected to be replaced with distribution feeders. The test feeder is IEEE 8500 node test feeder as shown in Figure 2.14. We choose ten different locations across the feeder to connect PV systems. All the PVs are assumed to be identical with the same power rating. The number of test feeder at each boundary bus is calculated such that the boundary bus total load stays unchanged. The total number of distribution feeder considered in this test feeder is 24. Details of the system configurations can be found in Appendix III.

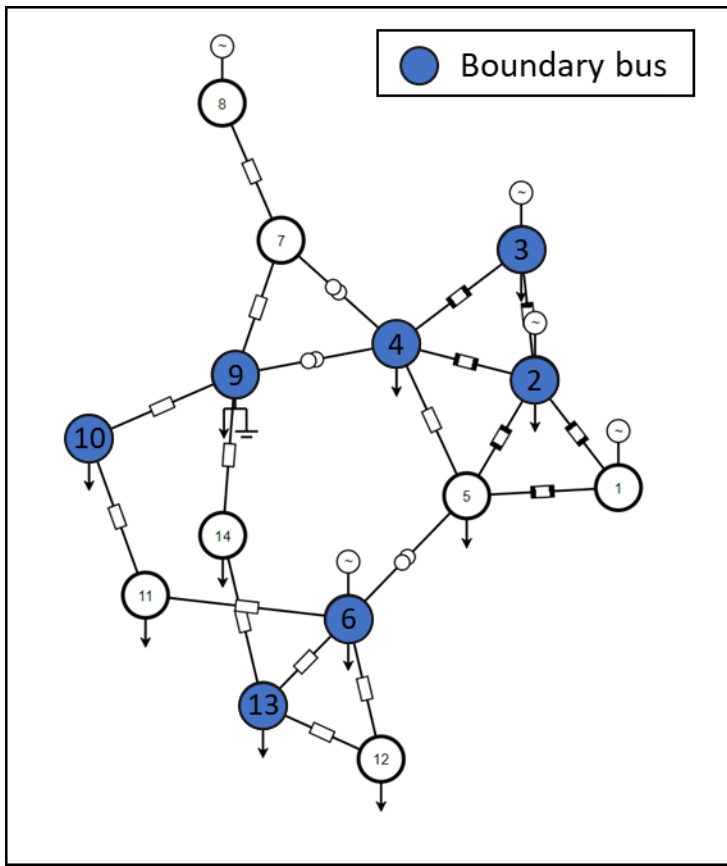


Figure 2.13. IEEE 14 bus system.

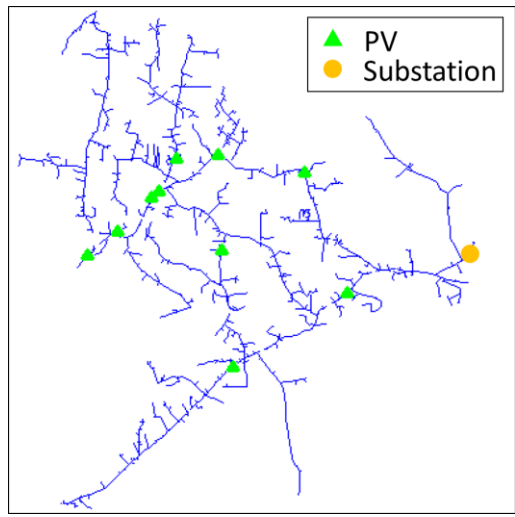


Figure 2.14. IEEE 8500-node test feeder.

2.3 Results and Evaluation of High PV Penetration Impact on Frequency Response

Using the developed testbeds, we can evaluate the impact of high PV penetration on frequency response. For each testbed, the same system disturbance event is simulated under different PV penetration levels. The performance can be evaluated using numerical metrics like RoC, nadir. The settling time is not considered since it is mainly affected by secondary control, AGC, settling time, and settling frequency.

2.3.1 Frequency Response in PSCAD

In the PSCAD testbed, we simulate the test system with the same disturbance event under different PV penetration levels from 0% to 40%, and 60%. The event is a load increase of 0.12 MW. The frequency response for each scenario is plotted in Figure 2.15 and the corresponding generation plot of synchronous generator and PV is in Figure 2.16. A summary of evaluation metrics for the frequency response is in Table 2.2.

As we increase the PV penetration, the synchronous generator capacity is also adjusted. As described in (40), the adjusted capacity is equal to the subtraction of original capacity by the amount of PV penetration power. The penetration power is calculated by total load and penetration percentage.

$$GenCap_{adjusted} = GenCap - Load_{total} \times Penetration\% \quad (40)$$

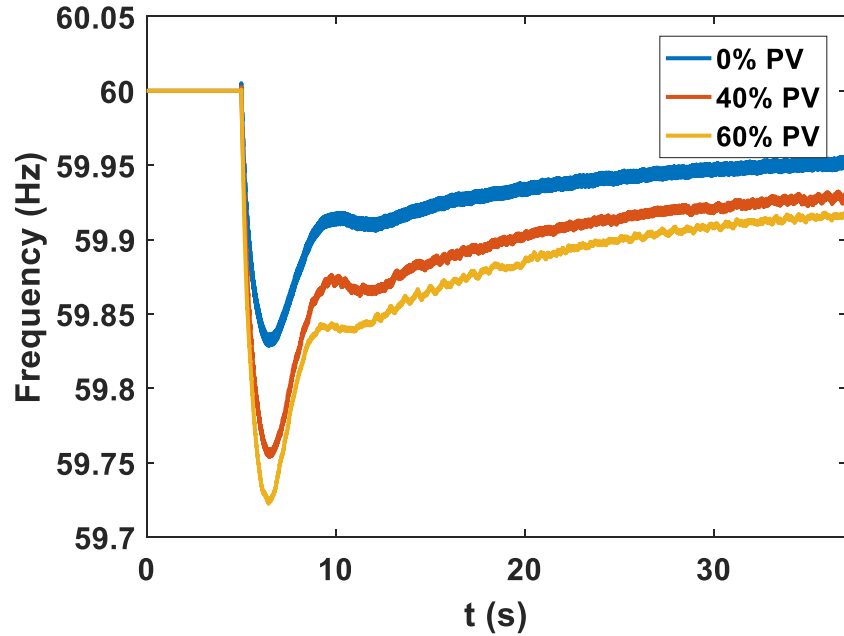


Figure 2.15. Frequency response under different PV penetration levels in PSCAD testbed.

Table 2.2. A Summary of Evaluation Metrics for PSCAD Testbed.

| PV Penetration | 0% | 40% | 60% |
|-------------------------|-----------|------------|------------|
| RoC (mHz/s) | -323.5 | -445.9 | -527.8 |
| Frequency Nadir (Hz) | 59.8287 | 59.7540 | 59.7226 |
| Settling Time (s) | ~45 | ~45 | ~45 |
| Settling Frequency (Hz) | 59.952 | 59.927 | 59.915 |

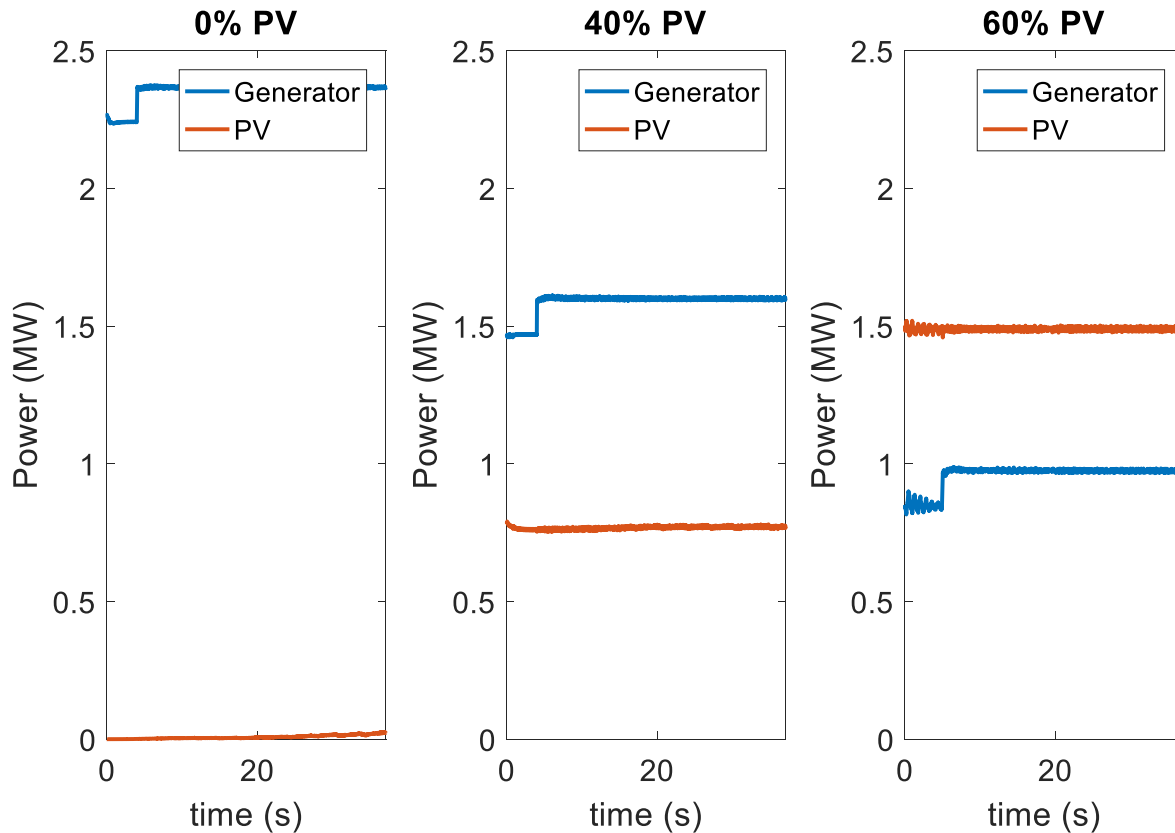


Figure 2.16. Generator and PV generation under different PV penetration levels in PSCAD testbed.

From Figure 2.15, it is evident that, with higher PV penetration in the test system, the synchronous generation capacity shrinks and therefore the frequency drops faster and reaches lower nadir in its first swing. Affected by the degraded capability of governor control, settling frequency also becomes lower. The impact on frequency response is smaller when PV increases from 40% to 60%, than that of increasing from 0% to 40%. This observation is supported by the evaluation metrics recorded in Table 2.2. In the 40% PV case, the RoC becomes worse by 122.4 mHz/s from 0% PV, while the change in RoC from 40% to 60% is only 81.9 mHz/s. For frequency nadir, 40% PV case drops 0.0747 Hz from base case, while 60% PV case drops another 0.0314 Hz, which is almost half of that for 40% PV case. This relationship between the decrements is the

same as that of the penetration increment in percentage. Similar observation can also be found in the settling frequencies. Since no secondary control is simulated, the settling time is almost identical in each case, which is around 45 seconds.

Figure 2.16 shows the power generation from synchronous generator and PV. From this figure, moving from 0% PV case to 60% PV case, we can clearly see the increased penetration level of PV generation, comparing to synchronous generation.

2.3.2 Frequency Response in Dynamic Co-simulation

To further evaluate the impact of PV penetration on the frequency response, the similar simulations are conducted in the dynamic co-simulation testbed with a much larger test system. In this testbed, we simulate a more practical disturbance event, which is a generator tripping. The same event is applied to three cases where the PV penetration increases from 0% to 20%, and 40%. The frequency response for each scenario is plotted in Figure 2.17 and the corresponding generation plot of synchronous generator and PV is in Figure 2.18. A summary of evaluation metrics for the frequency response is in Table 2.3.

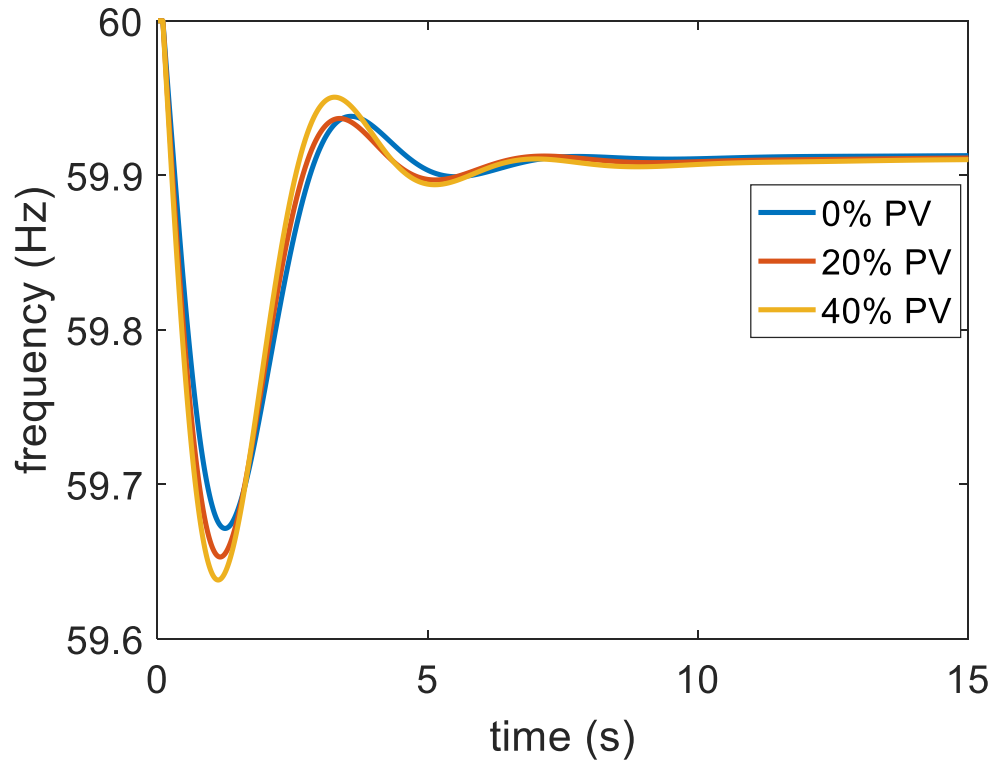


Figure 2.17. Frequency response under different PV penetration levels in dynamic co-simulation testbed.

Table 2.3. A Summary of Evaluation Metrics for Dynamic Co-simulation Testbed.

| PV Penetration | 0% | 20% | 40% |
|-------------------------|-----------|------------|------------|
| RoC (mHz/s) | -488.7 | -593.7 | -639.5 |
| Frequency Nadir (Hz) | 59.6719 | 59.6531 | 59.6379 |
| Settling Time (s) | ~16 | ~16 | ~16 |
| Settling Frequency (Hz) | 59.913 | 59.912 | 59.911 |

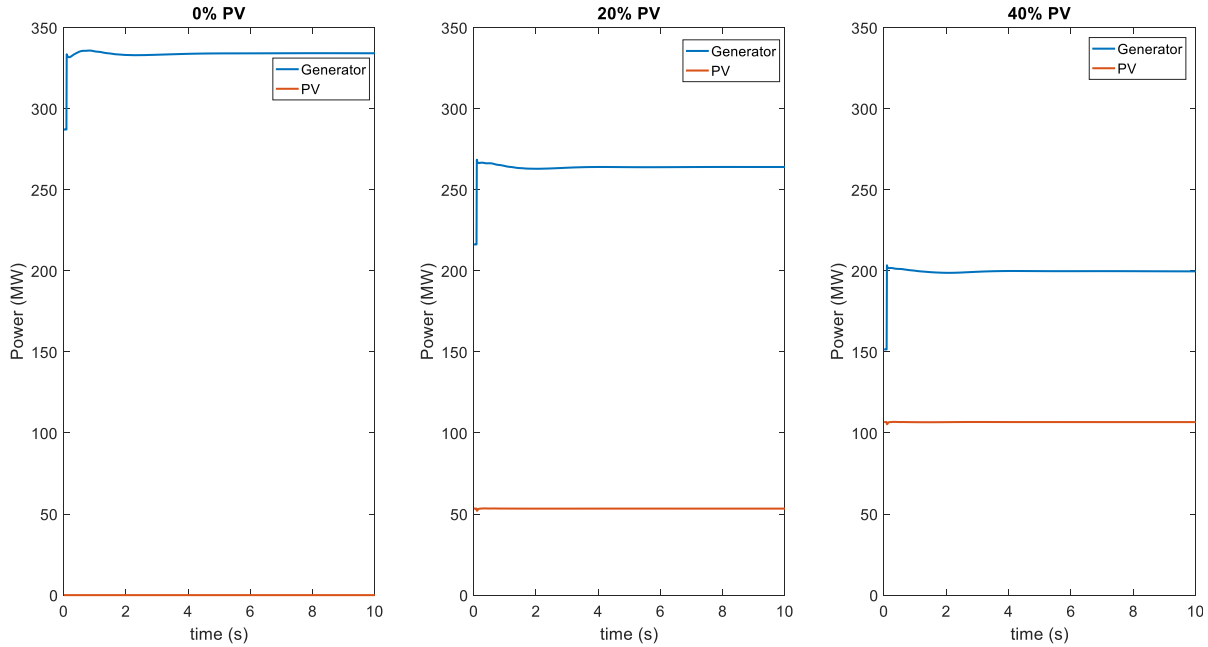


Figure 2.18. Generator and PV generation under different PV penetration levels in dynamic co-simulation testbed.

In this simulation of a large test system that contains both network details of transmission and distribution systems, the observations are very similar to what we discussed in Section 2.3.1. From the plot in Figure 2.17, the higher PV penetration results in faster drop of frequency after the disturbance and lower nadir in the first swing. In addition, the increasing PV also leads to more oscillations and lower settling frequency. These observed impacts are well-supported by the numerical evaluation metrics in Table 2.3. Similar to the previous results, the decrements in frequency nadir and settling frequency are also proportionally related to the increments in PV penetration percentage. For example, the two differences in frequency nadir from 0% to 20% PV case and from 20% to 40% PV case are 0.0188 Hz and 0.0152 Hz, which are very close to each other. For the settling frequency, we also the same decrement of 0.001 Hz between two adjacent cases.

We also notice that, in this test case, the difference between each penetration level is not as large as that in PSCAD testbed case. The reason is that the two testbed have different original synchronous generation capacity. In PSCAD testbed, the original capacity is set to 4 MVA, which is not too much greater than the total load of 2.25 MW. However, in this case, the original capacity is 1000 MVA, while the total load is only 330 MW. Therefore, the PSCAD case demonstrates a worse case where not much of reserved capacity is available. As a result, serious impact can be observed from high PV penetration. In the co-simulation case, however, the greatly increased PV penetration leads to relatively less impact on the frequency response, because of the large amount of capacity reserve.

CHAPTER 3 FREQUENCY CONTROL SCHEME FOR LARGE-SCALE PV PLANTS

As reviewed in Chapter 1, the growing level of PV generation challenges the conventional generation control in power systems, as the current PV systems do not possess inertia or governor system. Therefore, research efforts have been made to adopt new supervisory control for PV systems to provide frequency support the system, so that the output power of PV system will respond to any system disturbances and help maintain the real power balance. So far most of the existing methods focus on two main approaches: 1) de-loading control which is to first curtail PV array output power at a de-loaded level and then adjust its operating point [21-25]; and 2) DC-link voltage control which is to release/absorb power from DC-link capacitor by controlling its voltage [26-29].

However, as indicated before, most of the current methods aim at making PV system behave like a synchronous generator. One shortcoming is that these controller designs are based on local PV only. Thus, the actual system frequency response will not necessarily be that of a conventional system with desired equivalent inertia and droop constants, especially during the initial a few seconds. However, an accurate estimate of the frequency response capability is indeed very important to system operators in order to maintain it at a proper level.

To overcome the above limitation, in this chapter, we propose a novel controller whose objective is to control the PV power output such that, under a load disturbance, the system frequency response can effectively track that of a reference system with desired equivalent inertia

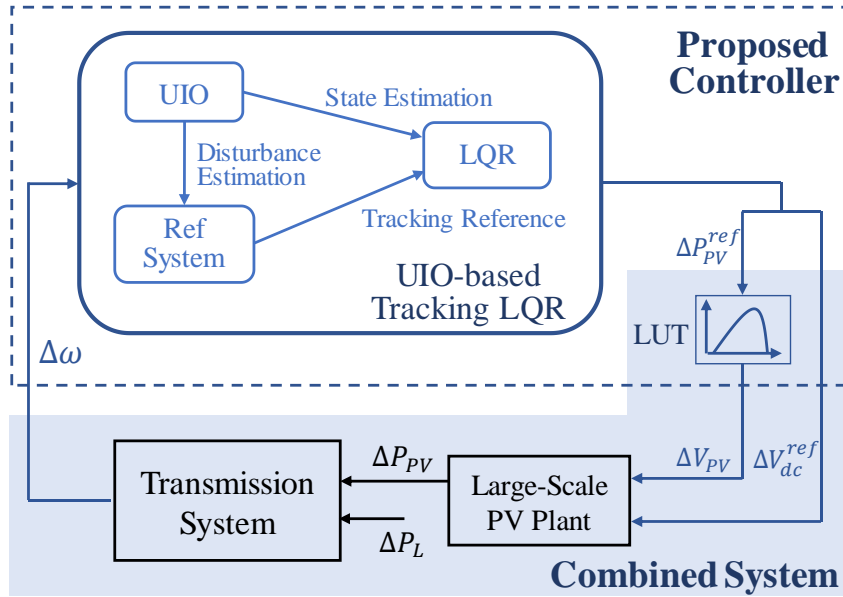


Figure 3.1. Conceptual diagram of proposed controller.

and droop constants (H^{ref} and R^{ref}) which are provided by the system operator. To achieve this objective, the proposed controller comprises an LUT and a UIO-based tracking LQR, as illustrated in Figure 3.1. The LUT is introduced to compensate the nonlinearities in the PV plant model. Also for modeling purpose, we associate the LUT together with the transmission system and PV plant and refer to the combination as the combined system so that its model can be taken as the plant model for designing the UIO-based tracking LQR. To ensure the frequency tracking, the LQR is used to minimize the error between system frequency and its reference. Since the LQR requires full state information and the system disturbance is unknown, a UIO is used. As shown in Fig. 1, the UIO also provides disturbance estimation for the reference system to generate the tracking reference. The reference system is a virtually constructed system inside of the tracking LQR and serves as a “desired version” of the transmission system with desired frequency response capability. Therefore, by following the reference system frequency with help of proposed controller, the frequency response of the whole system (the close-loop system) will be improved to as desired, i.e., close to that of the reference system.

To design the UIO and LQR, a linear combined system model containing the PV system model is needed. In addition, the PV system model should consider control inputs for designing the frequency support control. Models in [44, 45] neglect the DC-link dynamics and PV array characteristics and thus do not meet our need. Considering the DC-side dynamics, linear models are proposed in [46, 47] but without including supervisory control inputs. Reference [23] investigates the modeling of PV system with droop and inertia emulation. However, a linear model is only derived for the power control loop and does not include DC-link and inverter control. In this paper, we first propose a small-signal model (SSM) for the PV system. The main characteristics of this SSM, as it will be illustrated later, is that it captures the dynamics between the local controller set-points and the desired system output, which is the power output, and thus suits the design of frequency support functions. Then, the LUT in Figure 3.1 capturing the PV array characteristics is used to compensate the nonlinearity in the SSM so that the model for PV plant with the LUT becomes linear. Combining this linear model with the classical load frequency control (LFC) model that we used for the transmission system, we can obtain a linear combined system model for designing the UIO-based tracking LQR.

The main contributions of this chapter's work can be summarized as: 1) An SSM for the three-phase PV system which is suitable for designing frequency support controls; 2) A novel UIO-based LQR controller for the PV system to provide frequency support. The controller assures that the frequency response of combined system can track that of a reference system with given inertia and droop constants and therefore assures desired system frequency response. Next section outlines the system models adopted for the controller design. Section 3.2 introduces the design of the proposed control scheme. Section 3.2 presents the test results.

3.1 System Modeling

In this section, we introduce the models for the large-scale PV plant, transmission system, and the combined system. These models are used in the later section for the controller design.

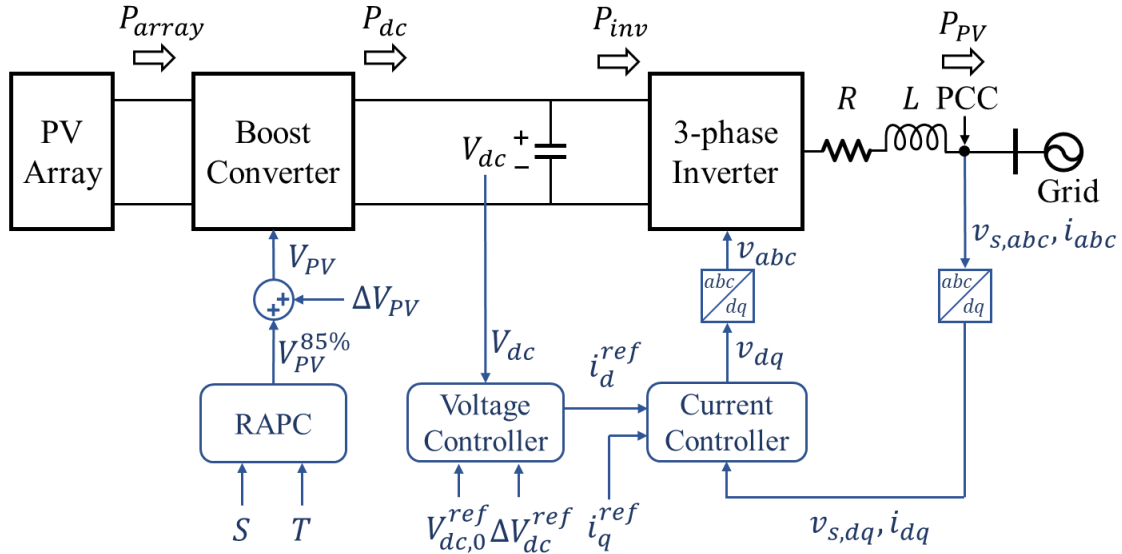


Figure 3.2. Block diagram of a two-stage three-phase PV system.

3.1.1 Large-scale PV Plant

For the large-scale PV plant, we assume that it consists of identical PV sub-systems, in which each one is a two-stage three-phase PV system as shown in Figure 3.2. For simplicity, we use the model for one PV system to represent the PV plant as it can be easily scaled up. In the following, we adopt the similar modeling approach as the average model introduced in Chapter 2 for single-phase PV system to model its three-phase counterpart. To model the electrical part, we first model the PV array by its $P - V$ characteristic function [48]. The parameters in (41) are listed in Appendix III.

$$P_{array} = f(V_{PV}, S, T) = n_p I_{ph} V_{PV} - n_p I_{rs} V_{PV} \left(e^{\frac{q}{kT} \frac{V_{PV}}{n_s}} - 1 \right) \quad (41)$$

Then we use average models for the DC-DC boost converter and three-phase inverter.

Therefore, by ignoring losses, we have the power balance equations as follows:

$$P_{array} = P_{dc}, \quad P_{inv} = P_{PV} \quad (42)$$

where P_{dc} and P_{inv} are the power flowing into and out of the DC-link. P_{PV} is the power output injected to the grid.

The DC-link dynamics can also be modeled in terms of the power balance:

$$\frac{C}{2} \left(\frac{dV_{dc}^2}{dt} \right) = P_{dc} - P_{inv} = P_{array} - P_{PV} \quad (43)$$

where P_{PV} can be further expressed in d-q frame as:

$$P_{PV} = \frac{3}{2} (i_d v_{sd} + i_q v_{sq}) = \frac{3}{2} i_d v_{sd} \quad (44)$$

in which i_d, i_q and v_{sd}, v_{sq} are the d-q components of current and voltage at point of common coupling, respectively. They can be obtained from v_{abc} and i_{abc} through the $abc - dq$ transformation where ω and θ are provided by an ideal phase-locked loop (PLL). The PLL also regulates v_{sq} to zero and thus the simplification in (44) can be made.

Combing (41)-(44), the power balance becomes:

$$\frac{C}{2} \left(\frac{dV_{dc}^2}{dt} \right) = f(V_{PV}, S, T) - \frac{3}{2} i_d v_{sd} \quad (45)$$

As Figure 3.2 illustrates, there are two parts of local controllers. One is the boost converter control which is used to determine the operating point of the PV array. Normally an MPPT controller is used here. However, this controller needs to be revised so that we can operate PV below MPP. Therefore, we adopt the rapid active power control (RAPC) method from [22] for the controller. For a given irradiance S , and temperature t , the RAPC determines our default de-loading set-point $V_{PV}^{85\%}$ (the voltage corresponding to 85% of the MPP). Then the PV array voltage will be determined as $V_{PV} = V_{PV}^{85\%} + \Delta V_{PV}$, where the control input ΔV_{PV} is received from the supervisory controller. The other part refers to the revised conventional dual-loop current mode controller for

inverter. The voltage controller regulates DC-link voltage by generating the reference of i_d for current controller through a PI controller. Here we also include ΔV_{dc}^{ref} for adjusting the DC-link voltage and being as the other control input with which we can control the power released (or absorbed) from the capacitor. For the current controller, two identical PI controllers are used to regulate inverter output currents to their references in dq-frame. Furthermore, a feedforward decoupling scheme from [47] is adopted to decouple the current control dynamics from grid voltage and also the output filter. By choosing the PI controller parameters as:

$$k_p^i = \frac{L}{\tau}, k_l^i = \frac{R}{\tau} \quad (46)$$

and combining with current dynamics at filter, the controller dynamics can be described as:

$$\frac{di_d}{dt} = -\frac{1}{\tau}i_d - \frac{k_p}{\tau}V_{dc} + \frac{k_p}{\tau}V_{dc}^{ref} + \frac{1}{\tau}x \quad (47)$$

$$\frac{di_q}{dt} = -\frac{1}{\tau}i_q + \frac{1}{\tau}i_q^{ref} \quad (48)$$

$$\frac{dx}{dt} = -k_l V_{dc} + k_l V_{dc}^{ref} \quad (49)$$

where x is the controller state which we introduce to avoid second-order derivative of state.

Equations (47)-(49), along with(45), represent the original nonlinear model of the PV system.

Next, we derive the SSM through linearization of the original model. First, (45) can be written as:

$$CV_{dc} \left(\frac{dV_{dc}}{dt} \right) = f(V_{PV}, S, T) - \frac{3}{2}i_d v_{sd} \quad (50)$$

Then we approximate the V_{dc} in the LHS coefficient and v_{sd} by their nominal values $V_{dc,0}^{ref}$ and V_{sd} which are constants. Therefore, the linearization of (50) is given as:

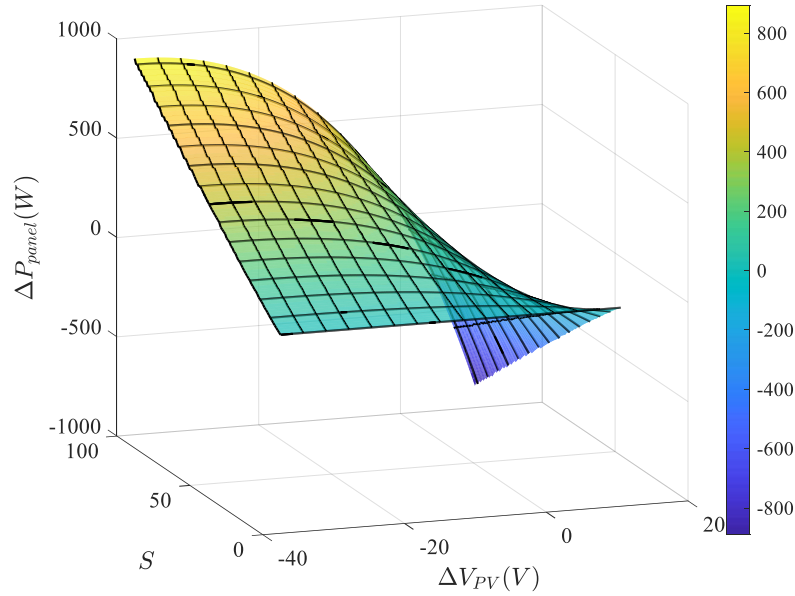


Figure 3.3. LUT surface at reference temperature ($T = 26.85^\circ\text{C}$) under different solar

irradiance levels and ΔV_{PV} .

$$\frac{d\Delta V_{dc}}{dt} = \frac{1}{CV_{dc,0}^{ref}} \underbrace{g(\Delta V_{PV}, S, T)}_{\Delta P_{array}} - \frac{1}{CV_{dc,0}^{ref}} \underbrace{\frac{3}{2} \Delta i_d V_{sd}}_{\Delta P_{PV}} \quad (51)$$

For the PV array characteristic function $f(V_{PV}, S, T)$, analytic linearization is not used for accuracy concern as the function is highly nonlinear. Instead, we create a LUT which is similar to the one used in RAPC. The difference is that this LUT maps the change in voltage, ΔV_{PV} , with the change in power, ΔP_{array} . Figure 3.3 shows an example surface of the LUT at reference temperature and various solar irradiation. The nominal PV array voltage used for constructing the LUT is $V_{PV}^{85\%}$. We use a function $g(\Delta V_{PV}, S, T)$ to represent this LUT.

In (51), we have the new state variable ΔP_{PV} representing the variation of PV system power output around the 85% of MPP. This state is of our main interest when designing frequency support functions. Therefore, we want to transform the Δi_d in (47) into ΔP_{PV} as well. Multiplying both sides of (47) by $\frac{3}{2} V_{sd}$ and linearize it, we have:

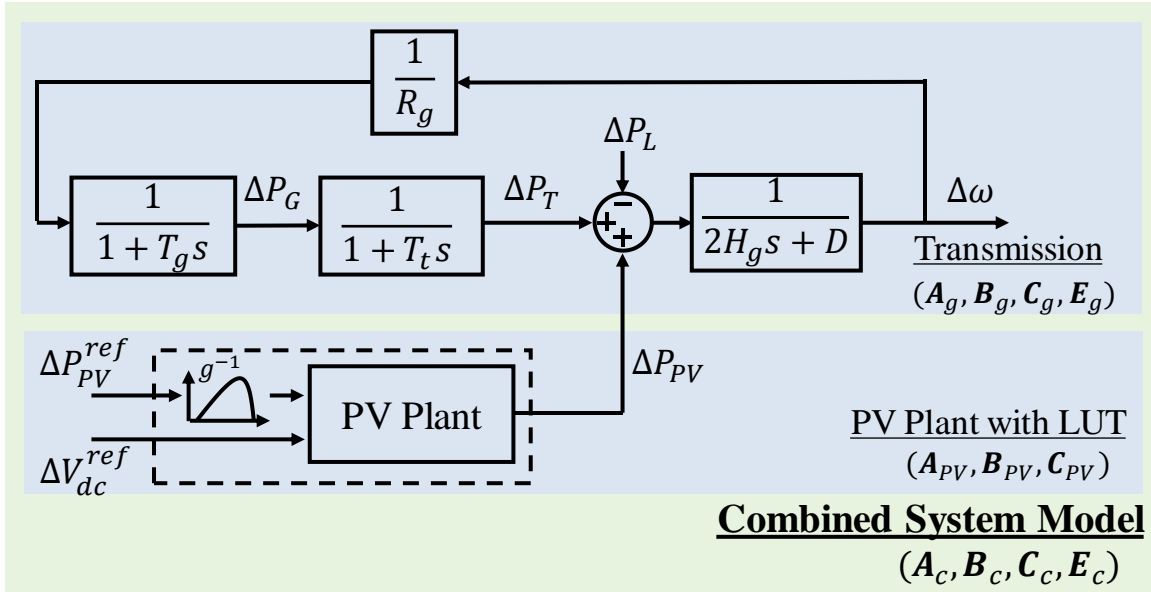


Figure 3.4. Block diagram of the system models.

$$\frac{d\Delta P_{PV}}{dt} = -\frac{1}{\tau}\Delta P_{PV} - \frac{3k_p V_{sd}}{2\tau}\Delta V_{dc} + \frac{3k_p V_{sd}}{2\tau}\Delta V_{dc}^{ref} + \frac{3V_{sd}}{2\tau}\Delta x \quad (52)$$

For (48), since the i_q dynamics is independent to others and its reference is set to zero, we can ignore it in the SSM. For (49), it can be easily linearized as:

$$\frac{d\Delta x}{dt} = -k_I \Delta V_{dc} + k_I \Delta V_{dc}^{ref} \quad (53)$$

Equations (51)-(53) complete our SSM for a two-stage three-phase PV system. However, this model still contains a nonlinear term, which is the LUT function. If we consider another LUT which is the inverse of function g :

$$\Delta V_{PV} = g^{-1}(\Delta P_{PV}^{ref}, S, T) \quad (54)$$

We can substitute (54) into (52) to get rid of the nonlinear term. Now a linear model for the PV plant with a reverse LUT is obtained and can be expressed by:

$$\begin{cases} \dot{\mathbf{x}}_{PV} = \mathbf{A}_{PV}\mathbf{x}_{PV} + \mathbf{B}_{PV}\mathbf{u}_{PV} \\ \mathbf{y}_{PV} = \mathbf{C}_{PV}\mathbf{x}_{PV} \end{cases} \quad (55)$$

3.1.2 Transmission System

For the transmission system, we use the LFC model to model the real power generation and frequency dynamics by ignoring the network details and AGC. The block diagram of this model is illustrated in Figure 3.4. Let \mathcal{G} denote the set of all synchronous generators in this system. Then the equivalent inertia and droop constants in the multi-machine LFC model can be obtained as:

$$H_g = \frac{\sum_{i \in \mathcal{G}} S_i H_i}{\sum_{i \in \mathcal{G}} S_i}, \quad \frac{1}{R_g} = \frac{\sum_{i \in \mathcal{G}} S_i / R_i}{\sum_{i \in \mathcal{G}} S_i} \quad (56)$$

For the governor and turbine dynamics, we assume the same time constants T_g and T_t for all generators in \mathcal{G} . Therefore, the LFC model for transmission system can be written as:

$$\begin{cases} \dot{\mathbf{x}}_g = \mathbf{A}_g \mathbf{x}_g + \mathbf{B}_g \mathbf{u}_g + \mathbf{E}_g \mathbf{d}_g \\ \mathbf{y}_g = \mathbf{C}_g \mathbf{x}_g \end{cases} \quad (57)$$

where we treat the increment power ΔP_{PV} from PV plant as an input (\mathbf{u}_g) to transmission system whereas the load change ΔP_L is taken as the disturbance (\mathbf{d}_g).

For some large systems, the model described by (56) and (57) may not have very accurate representation of the system dynamics. In those cases, there are two approaches to enhance the model. One is to obtain more accurate estimations of system inertia and droop using methods such as [60, 61]. The other approach is to use a more detailed full-order multi-machine model [62] to represent the system frequency response dynamics.

3.1.3 Combined System

To design the UIO-based tracking LQR, we need a linear plant model which includes models for both the transmission system and the PV plant. Although the LFC model for transmission system is linear, the SSM derived for the PV plant still contains a nonlinear term,

which is the LUT function $g(\Delta V_{PV}, S, T)$. To address this, we consider another LUT which is the inverse of function g :

$$\Delta V_{PV} = g^{-1}(\Delta P_{PV}^{ref}, S, T) \quad (58)$$

We can substitute (58) into (51) to compensate the nonlinear term and obtain a linear model for the PV plant with an LUT. The resulted linear model can be expressed by:

$$\begin{cases} \dot{\mathbf{x}}_{PV} = \mathbf{A}_{PV}\mathbf{x}_{PV} + \mathbf{B}_{PV}\mathbf{u}_{PV} \\ \mathbf{y}_{PV} = \mathbf{C}_{PV}\mathbf{x}_{PV} \end{cases} \quad (59)$$

where the output is ΔP_{PV} .

Next, if we define the combination of transmission system, PV plant, and the LUT g^{-1} as the combined system, the model for it can be derived by combing the models in (57) and (59) through the interfacing variable ΔP_{PV} , which is the output of PV plant but the input to transmission system. Since both models in (57) and (59) are linear, the combined system model is also linear and thus can be used as the plant model in the design of UIO-based tracking LQR. A block diagram for this model is illustrated in Figure 3.4 and the mathematical representation is as follows:

$$\begin{aligned} \underbrace{\begin{bmatrix} \dot{\mathbf{x}}_g \\ \dot{\mathbf{x}}_{PV} \end{bmatrix}}_{\dot{\mathbf{x}}_c} &= \underbrace{\begin{bmatrix} \mathbf{A}_g & \mathbf{B}_g \mathbf{C}_{PV} \\ 0 & \mathbf{A}_{PV} \end{bmatrix}}_{\mathbf{A}_c} \underbrace{\begin{bmatrix} \mathbf{x}_g \\ \mathbf{x}_{PV} \end{bmatrix}}_{\mathbf{x}_c} + \underbrace{\begin{bmatrix} 0 \\ \mathbf{B}_{PV} \end{bmatrix}}_{\mathbf{B}_c} \underbrace{\begin{bmatrix} \mathbf{u}_{PV} \end{bmatrix}}_{\mathbf{u}_c} \\ &+ \underbrace{\begin{bmatrix} \mathbf{E}_g \\ 0 \end{bmatrix}}_{\mathbf{E}_c} \underbrace{\begin{bmatrix} \mathbf{d}_g \end{bmatrix}}_{\mathbf{d}_c} \end{aligned} \quad (60)$$

$$\mathbf{y}_c = \mathbf{C}_c \mathbf{x}_c \quad (61)$$

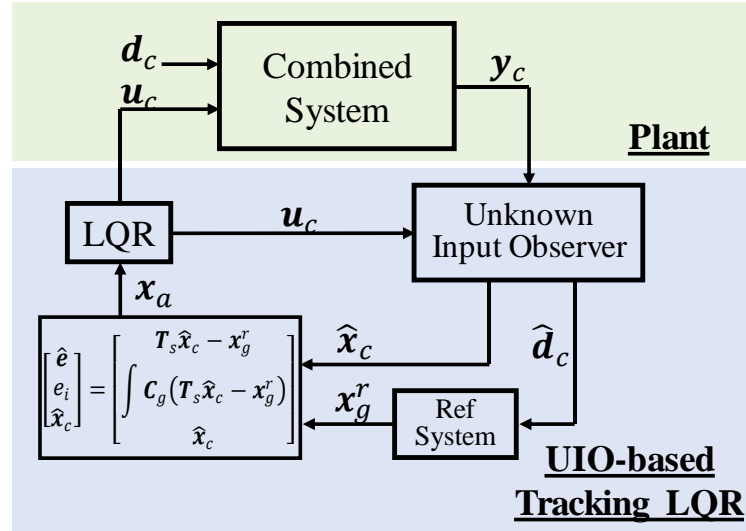


Figure 3.5. Architecture and components of the UIO-based tracking LQR..

where the output y_c is frequency deviation $\Delta\omega$.

3.2 Controller Design

In this section, we introduce the design of our proposed controller. As pointed out earlier, the control objective is to adjust the PV plant power output such that, under the same disturbance, the frequency response of the combined system (plant) can effectively track that of a reference system with given inertia and droop constants. This also implies that, by following the reference frequency, the frequency response of the combined system will be improved.

Since this is a tracking problem, we adopt an LQR-based controller to minimize the tracking error. As one part of the controller, the LUT (g^{-1}) has already been discussed in Section 3.1.3. Therefore, in the following, we focus on the other part of the proposed controller, which is the UIO-based tracking LQR. Comparing to other frequency-domain tracking methods, the proposed method is in time-domain and has its advantages for dealing with multi-input multi-output (MIMO) systems.

As shown in Figure 3.5, the UIO-based tracking LQR consists of three components: an LQR, a reference system, and a UIO. Based on the plant model, we first construct an augmented system where the tracking error and its integral are introduced as new states. Then the LQR can be designed to minimize the error states. To implement such an LQR, the UIO is designed to provide estimation of both states and disturbance of the combined system. In rest of this section, we will discuss each component in detail.

3.2.1 Unknown Input Observer

The plant we have (combined system described by (60)) has a disturbance term, load variation, which cannot be measured directly. Therefore, conventional observers with Luenberger structure cannot be adopted as they require the knowledge of all input signals, including the disturbance, to estimate the plant states. However, the unknown input observer with a different structure can effectively address the above limitation by estimating state information without any prior knowledge of the disturbance [63-65]. For the combined system in (60), the UIO can be designed as:

$$\begin{cases} \dot{\mathbf{z}} = \mathbf{F}\mathbf{z} + \mathbf{T}_o\mathbf{B}_c\mathbf{u}_c + \mathbf{K}_o\mathbf{y}_c \\ \hat{\mathbf{x}}_c = \mathbf{z} + \mathbf{H}_o\mathbf{y}_c \end{cases} \quad (62)$$

where \mathbf{z} is the newly introduced state in the UIO and $\hat{\mathbf{x}}_c$ is the estimated state of the combined system. As seen from (62), the UIO is essentially a dynamic system whose inputs are the input and output of combined system but no disturbance. The observer matrices can then be obtained as:

$$\mathbf{0} = (\mathbf{H}_o\mathbf{C}_c - \mathbf{I})\mathbf{E}_c \quad (63)$$

$$\mathbf{T}_o = \mathbf{I} - \mathbf{H}_o\mathbf{C}_c \quad (64)$$

$$\mathbf{A}_o = \mathbf{T}_o\mathbf{A}_c \quad (65)$$

$$\mathbf{F} = \mathbf{A}_o - \mathbf{K}_o^1\mathbf{C}_c \quad (66)$$

$$\mathbf{K}_o = \mathbf{K}_o^1 + \mathbf{F}\mathbf{H}_o \quad (67)$$

where \mathbf{K}_o^1 is the designed gain matrix such that all eigenvalues of \mathbf{F} are stable.

According to [63], the necessary and sufficient conditions for the existence of a UIO are given as:

- (i) $\text{rank}(\mathbf{C}_c\mathbf{E}_c) = \text{rank}(\mathbf{E}_c)$
- (ii) $(\mathbf{C}_c, \mathbf{A}_o)$ is a detectable pair.

It can be shown that (63) is solvable if and only if the Condition (i) is met. If this condition is not satisfied, then the UIO does not exist. For our combined system, both ranks in condition (i) are equal to 1. Next, Condition (ii) is required for the existence of gain matrix \mathbf{K}_o^1 . For this condition, the observability can first be checked for the pair $(\mathbf{C}_c, \mathbf{A}_o)$. If this pair is observable, then it is also detectable and pole-placement techniques can be directly used to obtain \mathbf{K}_o^1 . Otherwise, the detectability must be checked additionally. In our case, the pair $(\mathbf{C}_c, \mathbf{A}_o)$ is not observable but detectable. Therefore, a revised procedure is needed for calculating \mathbf{K}_o^1 . The idea [34] is to perform an observable canonical form decomposition of matrix \mathbf{A}_o and then do pole-placement only for stabilizing the observable states. Other non-observable states should all correspond to stable eigenvalues as guaranteed by the detectability.

In addition to estimating the plant states under the presence of unknown disturbance, another advantage of the UIO is that it can also estimate the disturbance. From [66], the estimated disturbance can be obtained as:

$$\hat{\mathbf{d}}_c = (\mathbf{C}_c\mathbf{E}_c)^+ (\hat{\mathbf{y}}_c - \mathbf{C}_c\mathbf{A}_c\hat{\mathbf{x}}_c - \mathbf{C}_c\mathbf{B}_c\mathbf{u}_c) \quad (68)$$

The disturbance estimation is indeed very important for our design. As shown in Figure 3.5, the estimated disturbance is needed for the reference system to generate the “desired” frequency response which is used as the tracking reference in the LQR design. However, one

difficulty of obtaining the estimated disturbance is that (68) contains the derivative of $\hat{\mathbf{y}}_c$. To address this problem, we implement a second-order filter $\mathbf{H}_w(s)$ as:

$$\mathbf{w} = \mathbf{H}_w(s)\hat{\mathbf{y}}_c = \frac{s}{(\tau_1 s + 1)(\tau_2 s + 1)}\hat{\mathbf{y}}_c \quad (69)$$

where τ_1 and τ_2 can be designed sufficiently small such that $\mathbf{H}_w(s)$ behaves very similar to the derivative at low frequencies. Therefore, \mathbf{w} can be used as $\dot{\hat{\mathbf{y}}}_c$ to calculate $\hat{\mathbf{d}}_c$. Equation (69) can also be written as:

$$\begin{cases} \dot{w}_1 = -\frac{\tau_1 + \tau_2}{\tau_1 \tau_2} w_1 - \frac{1}{\tau_1 \tau_2} w_2 + \frac{1}{\tau_1 \tau_2} \hat{\mathbf{y}}_c \\ \dot{w}_2 = w_1 \end{cases} \quad (70)$$

Equations (62), (68), and (70) represent our UIO.

3.2.2 Reference System

The reference system is also represented by the LFC model, but with desired inertia and droop constants (H^{ref} and R^{ref}). Hence, similar to (57), the state-space model for reference system is:

$$\begin{cases} \dot{\mathbf{x}}_g^r = \mathbf{A}_g^r \mathbf{x}_g^r + \mathbf{E}_g^r \mathbf{d}_g^r \\ \mathbf{y}_g^r = \mathbf{C}_g^r \mathbf{x}_g^r \end{cases} \quad (71)$$

where the input term is not included since reference system does not have PV.

Note that the role of this reference system is to provide a reference frequency response, for the plant to track. Or in other words, it helps us to translate the design objective from achieving certain frequency response capability into tracking specific system trajectories.

3.2.3 LQR

The LQR is a well-known state feedback controller based on optimal control theory [67, 68]. With the LQR gain, we can guarantee the stability of close-loop system while minimizing the cost function. Therefore, in this case, we can apply LQR to minimize the tracking error. To design

such an LQR, as mentioned earlier, an augmented system must be constructed as the plant model.

Let us define the error state as:

$$\mathbf{e} = \mathbf{x}_g - \mathbf{x}_g^r \quad (72)$$

$$\begin{aligned} \dot{\mathbf{e}} &= \dot{\mathbf{x}}_g - \dot{\mathbf{x}}_g^r \\ &= \mathbf{A}_g \mathbf{x}_g + \mathbf{B}_g \mathbf{u}_g + \mathbf{E}_g \mathbf{d}_g - (\mathbf{A}_g^r \mathbf{x}_g^r + \mathbf{E}_g^r \mathbf{d}_g^r) \\ &= \mathbf{A}_g^r \mathbf{e} + (\mathbf{A}_g - \mathbf{A}_g^r) \mathbf{x}_g + \mathbf{B}_{PV} \mathbf{C}_{PV} \mathbf{x}_{PV} + \mathbf{E}_g \mathbf{d}_g - \mathbf{E}_g^r \mathbf{d}_g^r \end{aligned} \quad (73)$$

Now we can form an initial augmented system as:

$$\begin{aligned} \begin{bmatrix} \dot{\mathbf{e}} \\ \dot{\mathbf{x}}_c \end{bmatrix} &= \begin{bmatrix} \mathbf{A}_g^r & [\mathbf{A}_g - \mathbf{A}_g^r \mid \mathbf{B}_g \mathbf{C}_{PV}] \\ \mathbf{0} & \mathbf{A}_c \end{bmatrix} \begin{bmatrix} \mathbf{e} \\ \mathbf{x}_c \end{bmatrix} \\ &+ \begin{bmatrix} \mathbf{0} \\ \mathbf{B}_c \end{bmatrix} [\mathbf{u}_c] + \begin{bmatrix} \mathbf{E}_g \\ \mathbf{0} \end{bmatrix} [\mathbf{d}_g] - \begin{bmatrix} \mathbf{E}_g^r \\ \mathbf{0} \end{bmatrix} [\mathbf{d}_g^r] \end{aligned} \quad (74)$$

For the system in (74), we can design the LQR by minimizing the frequency tracking error, which is one of the states in \mathbf{e} . However, one limitation of this design is that, under the presence of disturbances in (74), the steady-state values of states including the tracking error do not converge to zero. Therefore, zero tracking error is not guaranteed, even though the designed optimal state feedback gain still minimizes the error. To address this limitation, we can introduce another new state which is the integral of frequency tracking error

$$\dot{\mathbf{e}}_i = \mathbf{C}_g \mathbf{e} \quad (75)$$

and the augmented system becomes:

$$\begin{cases} \begin{bmatrix} \dot{\mathbf{e}} \\ \dot{\mathbf{e}}_i \\ \dot{\mathbf{x}}_c \end{bmatrix} = \underbrace{\begin{bmatrix} \mathbf{A}_g^r & \mathbf{0} & [\mathbf{A}_g - \mathbf{A}_g^r | \mathbf{B}_g \mathbf{C}_{PV}] \\ \mathbf{C}_g & \mathbf{0} & \mathbf{0} \\ \mathbf{0} & \mathbf{0} & \mathbf{A}_c \end{bmatrix}}_{\mathbf{A}_a} \begin{bmatrix} \mathbf{e} \\ \mathbf{e}_i \\ \mathbf{x}_c \end{bmatrix} \\ + \underbrace{\begin{bmatrix} \mathbf{0} \\ \mathbf{0} \\ \mathbf{B}_c \end{bmatrix}}_{\mathbf{B}_a} \underbrace{[\mathbf{u}_c]}_{\mathbf{u}_a} + \underbrace{\begin{bmatrix} \mathbf{E}_g \\ \mathbf{0} \\ \mathbf{0} \end{bmatrix}}_{\mathbf{E}_a^1} \underbrace{[\mathbf{d}_g]}_{\mathbf{d}_a^1} - \underbrace{\begin{bmatrix} \mathbf{E}_g^r \\ \mathbf{0} \\ \mathbf{0} \end{bmatrix}}_{\mathbf{E}_a^2} \underbrace{[\mathbf{d}_g^r]}_{\mathbf{d}_a^2} \\ \mathbf{y}_a = \mathbf{C}_a \mathbf{x}_a \end{cases} \quad (76)$$

$$\mathbf{C}_a = \left[\begin{array}{cccc|c} 0 & 0 & 1 & 0 & \mathbf{0}_{2 \times 6} \\ 0 & 0 & 0 & 1 & \end{array} \right] \quad (77)$$

With the choice of \mathbf{C}_a , the output for augmented system only contains frequency tracking error and its integral. Now for system in (76), we can obtain the optimal control input $\mathbf{u}_a = -\mathbf{K}\mathbf{x}_a$ by minimizing the cost function given as [67, 68]:

$$J = \int_0^{\infty} (\mathbf{y}_a^T \mathbf{Q} \mathbf{y}_a^T + \mathbf{u}_a^T \mathbf{R} \mathbf{u}_a^T) dt \quad (78)$$

where \mathbf{Q} and \mathbf{R} are the positive weighting matrices which represent the relative importance of output and control input in the cost function, respectively. Higher values of \mathbf{Q} mean smaller transient regimes of output, whereas higher values of R result in less control effort. The optimal feedback gain \mathbf{K} is calculated as: $\mathbf{K} = \mathbf{R}^{-1} \mathbf{B}_a^T \mathbf{P}$, where \mathbf{P} is the solution to the algebraic Riccati equation:

$$\mathbf{A}_a^T \mathbf{P} + \mathbf{P} \mathbf{A}_a - \mathbf{P} \mathbf{B}_a \mathbf{R}^{-1} \mathbf{B}_a^T \mathbf{P} + \mathbf{Q} = \mathbf{0} \quad (79)$$

With the above LQR, we can guarantee zero tracking error in steady-state. Moreover, the tracking error is minimized by the optimization of objective function along the state trajectories towards the steady-state.

3.2.4 Analysis of Close-loop System

In this subsection, we combine all the designed components together along with our plant model to obtain the complete close-loop system model, with which we can justify that the design of our controller can be done independently component-by-component.

Recall that in the LQR design, all of the states are assumed to be known. Therefore, we first need to replace the states by their estimations from UIO. Specifically, the state feedback control input now becomes:

$$\begin{aligned}
 \mathbf{u}_c &= \mathbf{u}_a = -\mathbf{K}\hat{\mathbf{x}}_a \\
 &= -[\mathbf{K}_1 \quad \mathbf{K}_2 \quad \mathbf{K}_3][\hat{\mathbf{e}} \quad \mathbf{e}_i \quad \hat{\mathbf{x}}_c]^T \\
 &= -\mathbf{\Gamma}\mathbf{H}_o\mathbf{y}_c - \mathbf{\Gamma}\mathbf{z} - \mathbf{K}_2\mathbf{e}_i + \mathbf{K}_1\mathbf{x}_g^r
 \end{aligned} \tag{80}$$

where $\mathbf{\Gamma} = (\mathbf{K}_1\mathbf{T}_s + \mathbf{K}_3)$, $\mathbf{T}_s = [\mathbf{I}_{3 \times 3} \quad \mathbf{0}_{3 \times 3}]$, and $\dot{\mathbf{e}}_i = \mathbf{C}_g\mathbf{e} = \mathbf{C}_g(\mathbf{T}_s\hat{\mathbf{x}}_c - \mathbf{x}_g^r) = \mathbf{C}_g(\mathbf{T}_s(\mathbf{z} + \mathbf{H}_o\mathbf{y}_c) - \mathbf{x}_g^r)$.

In addition, the disturbance to the reference system, \mathbf{d}_g^r , also needs to be substituted by its estimation given by (68):

$$\begin{aligned}
 \mathbf{d}_g^r &= (\mathbf{C}_c\mathbf{E}_c)^\dagger[\mathbf{w} + \mathbf{C}_c(\mathbf{B}_c\mathbf{\Gamma} - \mathbf{A}_c)(\mathbf{H}_o\mathbf{y}_c + \mathbf{z}) \\
 &\quad + \mathbf{C}_c\mathbf{B}_c(\mathbf{K}_2\mathbf{e}_i - \mathbf{K}_1\mathbf{x}_g^r)]
 \end{aligned} \tag{81}$$

Now with (60)-(62), (69), (71), and (80) we can form the complete close-loop system in the form of:

$$\dot{\mathbf{x}}_{cl} = \mathbf{A}_{cl}\mathbf{x}_{cl} + \mathbf{E}_{cl}\mathbf{d}_{cl} \tag{82}$$

where \mathbf{A}_{cl} , \mathbf{E}_{cl} , \mathbf{x}_{cl} , \mathbf{d}_{cl} are given in (85) with $\mathbf{\Lambda} = \mathbf{E}_g^r(\mathbf{C}_c\mathbf{E}_c)^\dagger$. The system in (82) does not have input term since we have closed the feedback loop by our controller. Therefore, there is only a disturbance term which represents the load change to the combined system (plant).

Now let us consider two transformation matrices as:

$$\mathbf{T}_1 = \begin{bmatrix} \mathbf{I} & \mathbf{0} & \mathbf{0} & \mathbf{0} & \mathbf{0} & \mathbf{0} \\ \mathbf{0} & \mathbf{I} & \mathbf{0} & \mathbf{0} & \mathbf{0} & \mathbf{0} \\ \mathbf{0} & \mathbf{0} & \mathbf{I} & \mathbf{0} & \mathbf{0} & \mathbf{0} \\ \mathbf{0} & -\mathbf{T}_o & \mathbf{0} & \mathbf{I} & \mathbf{0} & \mathbf{0} \\ \mathbf{0} & \mathbf{0} & \mathbf{0} & \mathbf{0} & \mathbf{I} & \mathbf{0} \\ \mathbf{0} & \mathbf{0} & \mathbf{0} & \mathbf{0} & \mathbf{0} & \mathbf{I} \end{bmatrix}, \quad \mathbf{T}_2 = \begin{bmatrix} \mathbf{I} & \mathbf{0} & \mathbf{0} & \mathbf{0} & \mathbf{0} & \mathbf{0} \\ \mathbf{0} & \mathbf{I} & \mathbf{0} & \mathbf{0} & \mathbf{0} & \mathbf{0} \\ \mathbf{0} & \mathbf{0} & \mathbf{I} & \mathbf{0} & \mathbf{0} & \mathbf{0} \\ \mathbf{0} & -\mathbf{T}_o & \mathbf{0} & \mathbf{I} & \mathbf{0} & \mathbf{0} \\ \mathbf{0} & \mathbf{0} & \mathbf{0} & \mathbf{0} & \mathbf{I} & \mathbf{0} \\ \mathbf{0} & \mathbf{C}_c \mathbf{H}_o \mathbf{C}_c & \mathbf{0} & \mathbf{0} & \mathbf{0} & \mathbf{I} \end{bmatrix} \quad (83)$$

With \mathbf{T}_1 and \mathbf{T}_2 , we can perform a transformation of the close-loop system matrix \mathbf{A}_{cl} :

$$\mathbf{A}'_{cl} = \mathbf{T}_1 \mathbf{A}_{cl} \mathbf{T}_2 = \begin{bmatrix} \mathbf{A}'_{cl11} & \mathbf{A}'_{cl12} \\ \mathbf{0} & \mathbf{A}'_{cl22} \end{bmatrix} \quad (84)$$

where \mathbf{A}'_{cl} is a upper triangular matrix. Therefore the eigenvalues of \mathbf{A}'_{cl} are composed by the eigenvalues of \mathbf{A}'_{cl11} and \mathbf{A}'_{cl22} . As seen from (86), other than the combined and reference systems, $eig(\mathbf{A}'_{cl11})$ are only affected by the LQR gain whereas $eig(\mathbf{A}'_{cl22})$ are only related to the design of UIO. In other words, none of the close-loop system modes is jointly determined by both LQR and UIO. Therefore, we can design the LQR and UIO separately and independently.

$$\left\{ \begin{array}{l}
\mathbf{A}_{cl} = \begin{bmatrix}
\mathbf{B}_c \mathbf{K}_1 & \mathbf{A}_c - \mathbf{B}_c \boldsymbol{\Gamma} & -\mathbf{B}_c \mathbf{K}_2 & -\mathbf{B}_c \boldsymbol{\Gamma} & \mathbf{0} & \mathbf{0} \\
\mathbf{A}_g^r - \boldsymbol{\Lambda} \mathbf{C}_c \mathbf{B}_c \mathbf{K}_1 & \boldsymbol{\Lambda} (\mathbf{C}_c \mathbf{B}_c \boldsymbol{\Gamma} - \mathbf{C}_c \mathbf{A}_c) \mathbf{H}_o \mathbf{C}_c & \boldsymbol{\Lambda} \mathbf{C}_c \mathbf{B}_c \mathbf{K}_2 & \boldsymbol{\Lambda} (\mathbf{C}_c \mathbf{B}_c \boldsymbol{\Gamma} - \mathbf{C}_c \mathbf{A}_c) & \boldsymbol{\Lambda} & \mathbf{0} \\
-\mathbf{C}_g & \mathbf{C}_g \mathbf{T}_s \mathbf{H}_o \mathbf{C}_c & \mathbf{0} & \mathbf{C}_g \mathbf{T}_s & \mathbf{0} & \mathbf{0} \\
\mathbf{T}_o \mathbf{B}_c \mathbf{K}_1 & \mathbf{K}_o \mathbf{C}_c - \mathbf{T}_o \mathbf{B}_c \boldsymbol{\Gamma} \mathbf{H}_o \mathbf{C}_c & -\mathbf{T}_o \mathbf{B}_c \mathbf{K}_2 & \mathbf{F} - \mathbf{T}_o \mathbf{B}_c \boldsymbol{\Gamma} & \mathbf{0} & \mathbf{0} \\
\mathbf{0} & \frac{1}{\tau_1 \tau_2} \mathbf{C}_c \mathbf{H}_o \mathbf{C}_c & \mathbf{0} & \frac{1}{\tau_1 \tau_2} \mathbf{C}_c & -\frac{\tau_1 + \tau_2}{\tau_1 \tau_2} & -\frac{1}{\tau_1 \tau_2} \\
\mathbf{0} & \mathbf{0} & \mathbf{0} & \mathbf{0} & \mathbf{1} & \mathbf{0}
\end{bmatrix} \\
\mathbf{E}_{cl} = [\mathbf{E}_c \ \mathbf{0} \ \mathbf{0} \ \mathbf{0} \ \mathbf{0} \ \mathbf{0}]^T \\
\mathbf{x}_{cl} = [\mathbf{x}_c \ \mathbf{x}_g^r \ \mathbf{e}_i \ \mathbf{z} \ \mathbf{w}_1 \ \mathbf{w}_2]^T, \mathbf{d}_{cl} = [\mathbf{d}_c]
\end{array} \right. \quad (85)$$

$$\mathbf{A}'_{cl} = \begin{bmatrix}
\mathbf{B}_c \mathbf{K}_1 & \mathbf{A}_c - \mathbf{B}_c \boldsymbol{\Gamma} (\mathbf{H}_o \mathbf{C}_c + \mathbf{I}) & -\mathbf{B}_c \mathbf{K}_2 & -\mathbf{B}_c \boldsymbol{\Gamma} & \mathbf{0} & \mathbf{0} \\
\mathbf{A}_g^r - \boldsymbol{\Lambda} \mathbf{C}_c \mathbf{B}_c \mathbf{K}_1 & \boldsymbol{\Lambda} (\mathbf{C}_c \mathbf{B}_c \boldsymbol{\Gamma} - \mathbf{C}_c \mathbf{A}_c) (\mathbf{H}_o \mathbf{C}_c + \mathbf{I}) & \boldsymbol{\Lambda} \mathbf{C}_c \mathbf{B}_c \mathbf{K}_2 & \boldsymbol{\Lambda} (\mathbf{C}_c \mathbf{B}_c \boldsymbol{\Gamma} - \mathbf{C}_c \mathbf{A}_c) & \boldsymbol{\Lambda} & \mathbf{0} \\
-\mathbf{C}_g & \mathbf{C}_g \mathbf{T}_s \mathbf{H}_o \mathbf{C}_c & \mathbf{0} & \mathbf{C}_g \mathbf{T}_s & \mathbf{0} & \mathbf{0} \\
\mathbf{0} & \mathbf{0} & \mathbf{0} & \mathbf{F} & \mathbf{0} & \mathbf{0} \\
\mathbf{0} & \mathbf{0} & \mathbf{0} & \frac{1}{\tau_1 \tau_2} \mathbf{C}_c & -\frac{\tau_1 + \tau_2}{\tau_1 \tau_2} & -\frac{1}{\tau_1 \tau_2} \\
\mathbf{0} & \mathbf{0} & \mathbf{0} & \mathbf{0} & \mathbf{1} & \mathbf{0}
\end{bmatrix} \quad (86)$$

3.3 Test Results

In this section, we first present the validation results to show that our proposed SSM can very well represent the small-signal dynamics of the PV system. Then we demonstrate the design of our controller for a test system and assess its effectiveness in accurately providing desired frequency support. In the end, we also discuss some practical concerns about the implementation of proposed controller.

3.3.1 Model Validation

To validate the proposed SSM, a PV plant as illustrated in Figure 3.2 is built in MATLAB/Simulink using the original nonlinear average model. We use this system as the benchmark and compare its dynamics with proposed SSM. Key parameters of the PV system are given in Appendix IV. Since the primary application of the SSM is to design the controller, we are particularly interested in the dynamics of two quantities: PV system output power and DC-link voltage, following a change in the control inputs.

For testing, the benchmark system is set to be operating at 85% of its MPP (nominal de-loading condition) with $S = 1$ and $T = 300\text{ K}$. In the first test case, we decrease the PV array voltage by 10 V at $t = 1.5\text{ s}$. Since $V_{PV}^{85\%}$ is greater than V_{PV}^{MPP} , $\Delta V_{PV} = -10\text{ V}$ moves the operating point closer to the MPP and causes the power generated by PV array to increase. Figure 3.6 (b) shows this response and verifies that the response obtained from the SSM is very close to that of the detailed model. In the meantime, the absolute error, shown in Figure 3.6 (d) is also very small. Figure 3.6 (a) and (c) show the DC-link voltage profiles and the corresponding absolute error, respectively. These results show that ΔV_{dc} from SSM is also a

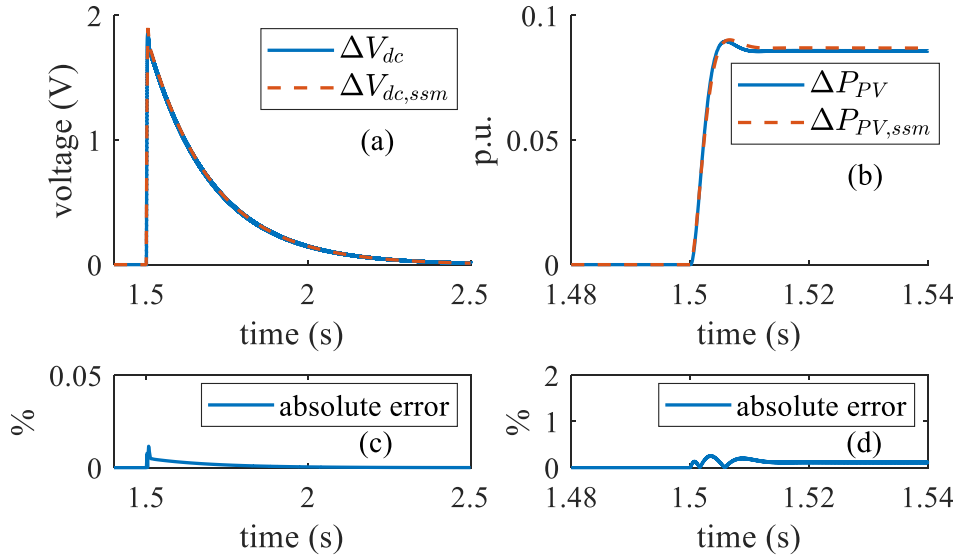


Figure 3.6. When $\Delta V_{PV} = -10$ V, (a), (c) comparison of DC-link voltages and the absolute error; (b), (d) comparison of output power and the absolute error.

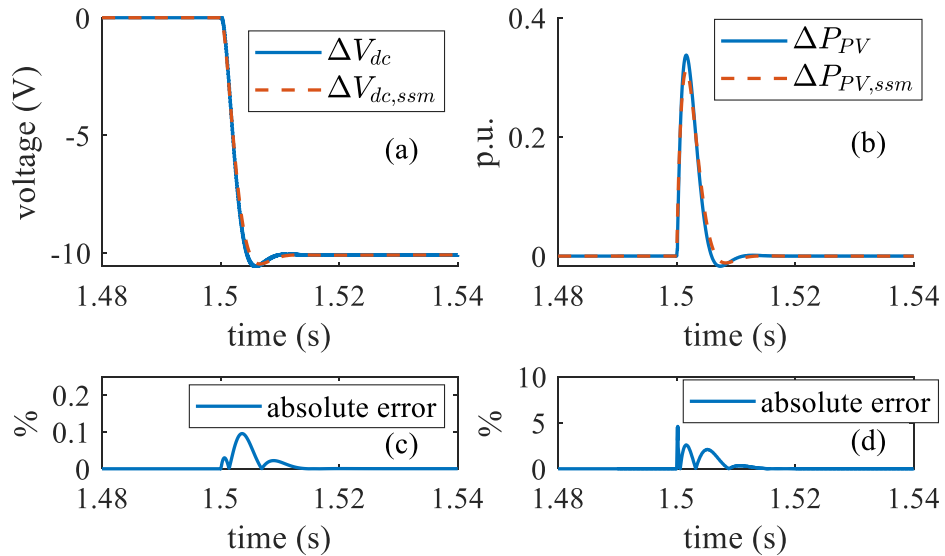


Figure 3.7. When $\Delta V_{dc}^{ref} = -10$ V, (a), (c) comparison of DC-link voltages and the absolute error; (b), (d) comparison of output power and the absolute error.

very accurate approximation to that of detail model and the associated absolute error is much smaller compared to the active power comparison.

In the second test case, we perturb the other control input which is ΔV_{dc}^{ref} . When we decrease the voltage reference by 10 V, we observe immediate power release from Figure 3.7 (b), and shortly after that, the power decreases to zero as the DC-link voltage shown in Figure 3.7 (a) settles to its steady-state. Figure 3.7 (a) and (b) show that the voltage and power profiles from SSM are again very close to those from the detailed model. The absolute errors for these two signals shown in Figure 3.7 (c) and (d) further confirm this with the maximum error being no greater than 5%.

3.3.2 Controller Performance

In order to demonstrate the effectiveness of proposed controller, we considered the standard three-machine-nine-bus WECC system and modified it by connecting a 20-MW PV plant at bus 6. The one-line diagram of this test system is shown in Figure 3.8. The system total capacity has also be rescaled to 195 MVA such that the PV penetration level is around 10%. The test system is built in MATLAB/Simulink and time-domain simulations were run for the following cases with 5 μ s time resolution.

To design the controller for this test system, we first need to determine the inertia and droop constants of the reference system. In this case, we assume that system inertia and droop constants have proportionally changed due to the integration of PV. Then, if we let the reference system represent the original system before adding PV, the H^{ref} and R^{ref} can be calculated as:

$$H^{ref} = H_g \frac{(S_b + P_{PV}^r)}{S_b}, \quad \frac{1}{R^{ref}} = \frac{1}{R_g} \frac{(S_b + P_{PV}^r)}{S_b} \quad (87)$$

where S_b is the test system MVA base and P_{PV}^r is the rated power of PV plant.

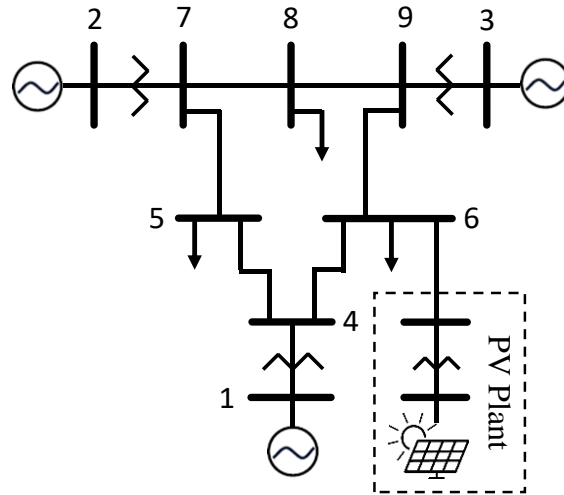


Figure 3.8. Modified WECC 9-bus system with PV plant.

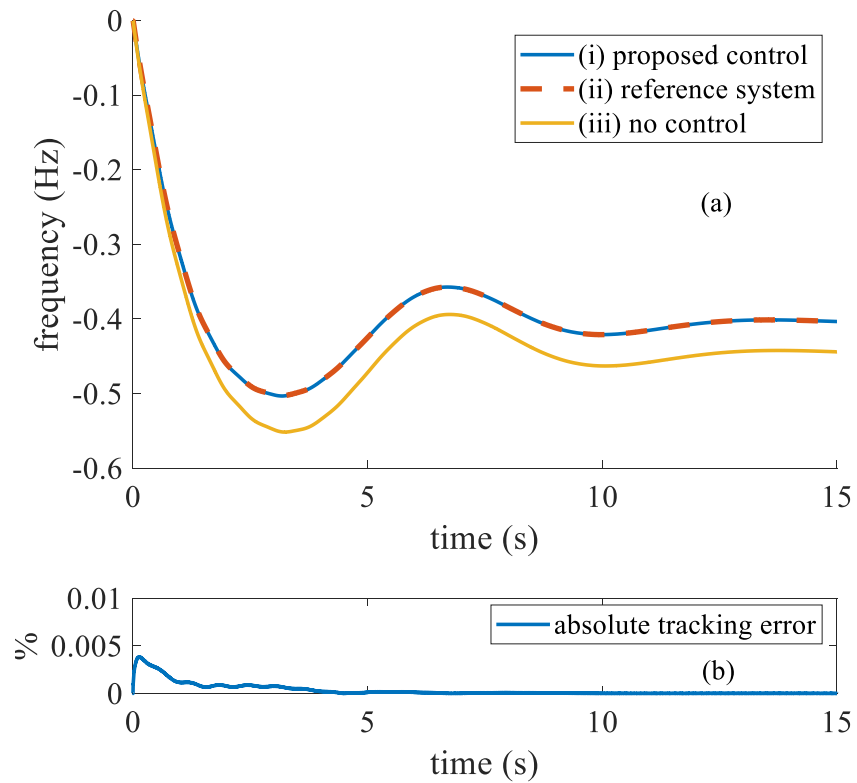


Figure 3.9. (a) Frequency response comparison under load disturbance; (b) Absolute error between test system frequency and reference system frequency.

The next important design parameters are the weighting matrices \mathbf{Q} and \mathbf{R} in the objective function (78). As discussed in Section 3.2.3, we need to select relatively large values for \mathbf{Q} in order to minimize the tracking error. We followed this guide and chose the weighting factors for \mathbf{Q} to be much higher than those for \mathbf{R} , as shown in TABLE 3.1. This selection also address the fact that the plant outputs in the model are in per unit while the control inputs are real values. With selected \mathbf{Q} and \mathbf{R} , the LQR is designed using *lqr* function in MATLAB.

For designing the UIO, since the plant model is only detectable but not observable, we used the MATLAB function *obsvf* to perform the observable canonical form decomposition. Then,

Table 3.1. Controller Design Parameters

| | |
|--|--|
| \mathbf{Q} Output weighting matrix | $diag(3 \times 10^4 \quad 3 \times 10^4)$ |
| \mathbf{R} Input weighting matrix | $diag(0.01 \quad 5)$ |
| λ Eigenvalues of UIO, $eig(F)$ | $-497.47 \pm j472.22,$ $-5.05, -1.25, -3.33, -80$ |
| $\tau_1 \tau_2$ Derivative filter time constants | 0.001, 0.001 |
| H_g Test system inertia | 5.9746 s |
| R_g Test system droop | 8% |
| H^{ref} Reference system inertia | 6.5874 s |
| R^{ref} Reference system droop | 7.26% |

command *place* is used to place poles only for the decoupled observable states. TABLE 3.1 shows the obtained eigenvalues.

To test the performance of the designed controller, we consider a large disturbance by applying a load disturbance of 0.1 pu at bus 8. Figure 3.9 (a) plots the frequency profiles after load disturbance for three cases: (i) system with proposed controller; (ii) reference system; and (iii) system without controller. We can easily observe that the frequency of test system with proposed controller effectively tracks that of our desired reference system and the performance is so good that we can barely see any difference. In support of above observation, the absolute tracking error between frequencies from (i) and (ii) is plotted in Figure 3.9 (b). The tracking error reaches the maximum, which is no greater than 0.005%, right after the disturbance and then settles to zero at steady-state. Comparing the frequency responses of cases (i) and (iii), we can also see that the proposed controller improves the frequency response in terms of rate of change of frequency (RoCoF), nadir, and settling frequency.

It is noted that the controller performance is also closely related to the estimation from the UIO. Figure 3.10 shows the comparison between real and estimated values from UIO. In Figure 3.10 (a), we plot the real disturbance by measuring the sum of power increments at all generators ($d_c = \sum \Delta P_{gen,i}$), and compare it with the estimated disturbance from UIO. Clearly, the estimation of disturbance is very accurate from the figure. Therefore, the generated frequency response from the reference system can indeed be used as a proper tracking reference. Since the LQR relies on estimated state variables, we also plotted these values in comparison with measured values in Figure 3.10 (b) and (c) for ΔV_{dc} and ΔP_{PV} , respectively. Again, the UIO shows very good estimation performance.

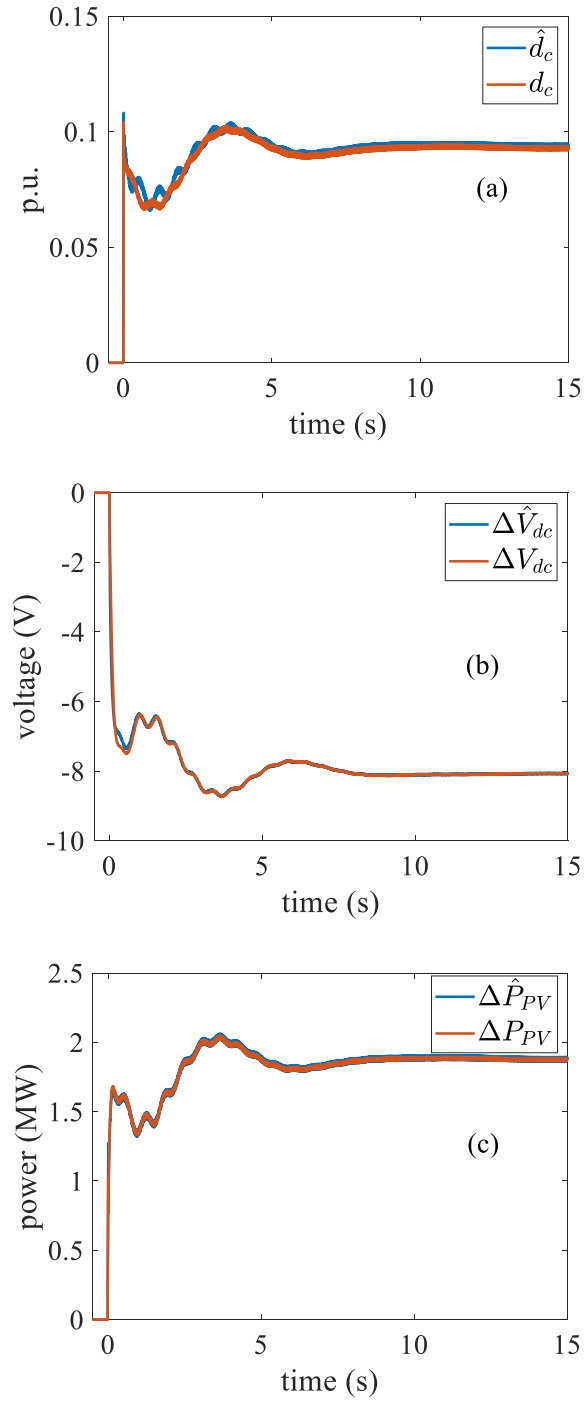
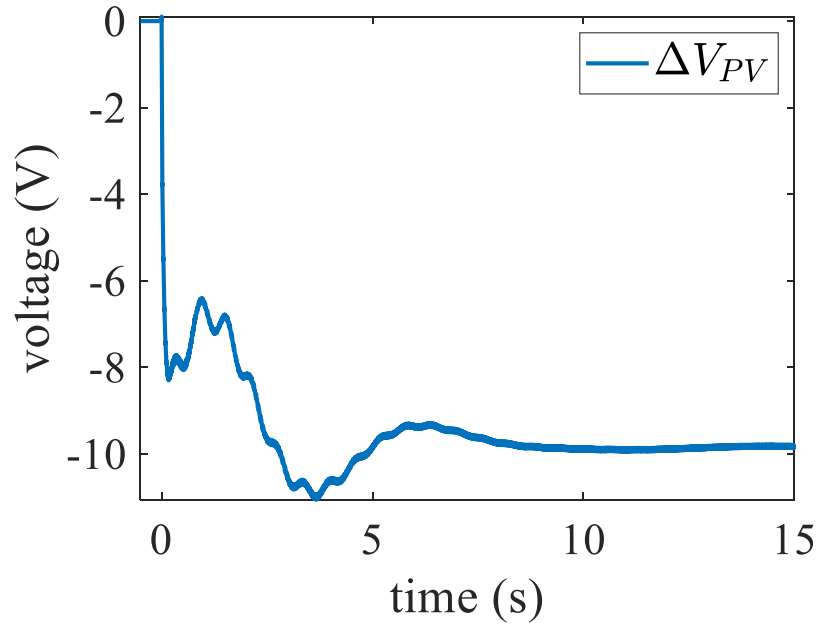
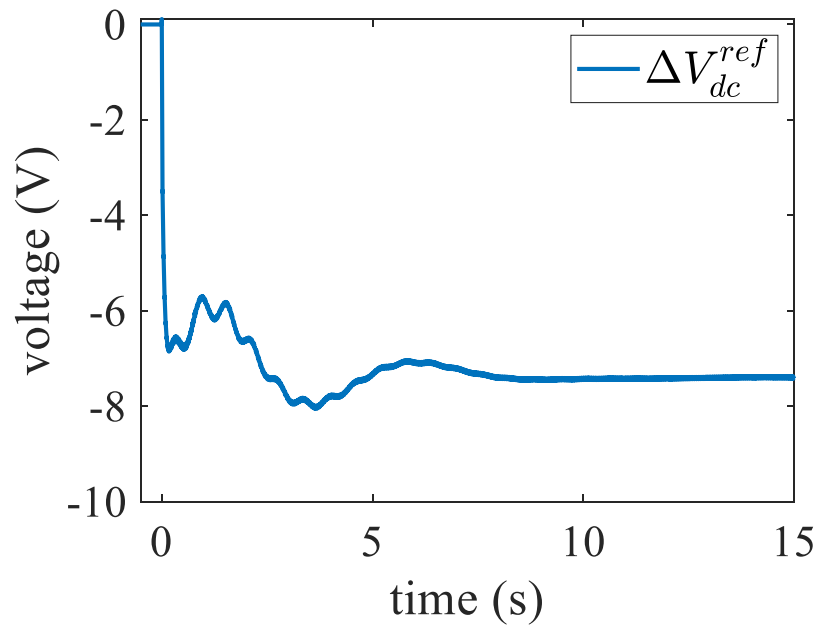


Figure 3.10. (a) Comparison of d_c and \hat{d}_c ; (b) Comparison of ΔV_{dc} and $\Delta \hat{V}_{dc}$; (c) Comparison of ΔP_{PV} and $\Delta \hat{P}_{PV}$.

In the meantime, we are interested in the actual control input sent to the PV system from our controller. In Figure 3.11, the PV array voltage are controlled to be lower than its nominal deloaded level. Since the PV are operating on the right-hand-side of the MPP, the decrease is expected to provide more power in response to the frequency drop. Similarly, as plotted in Figure 3.12, the DC-link voltage reference is also dropped to release instantaneous power from the capacitor. Both of the input signals are within reasonable range, without any spikes or unrealistic overshoot.

Figure 3.11. Control input ΔV_{PV} Figure 3.12. Control input ΔV_{dc}^{ref}

We also simulated an over-frequency event in which the load drops by 0.1 pu at bus 8. Figure 3.13 (a) plots the frequency responses. Similar to our observations in Figure 3.9, the frequency response of test system with proposed controller closely follows the reference frequency and is clearly improved when compared to (iii). The very good tracking performance is again supported by the absolute error shown in Figure 3.13 (b). Therefore, the proposed controller also performs very well under over-frequency events.

3.3.3 Comparison with Alternative Method

To compare the performance of the proposed method with an alternative method from literature, we adopted the method based on [23], where the PV is controlled to emulate a

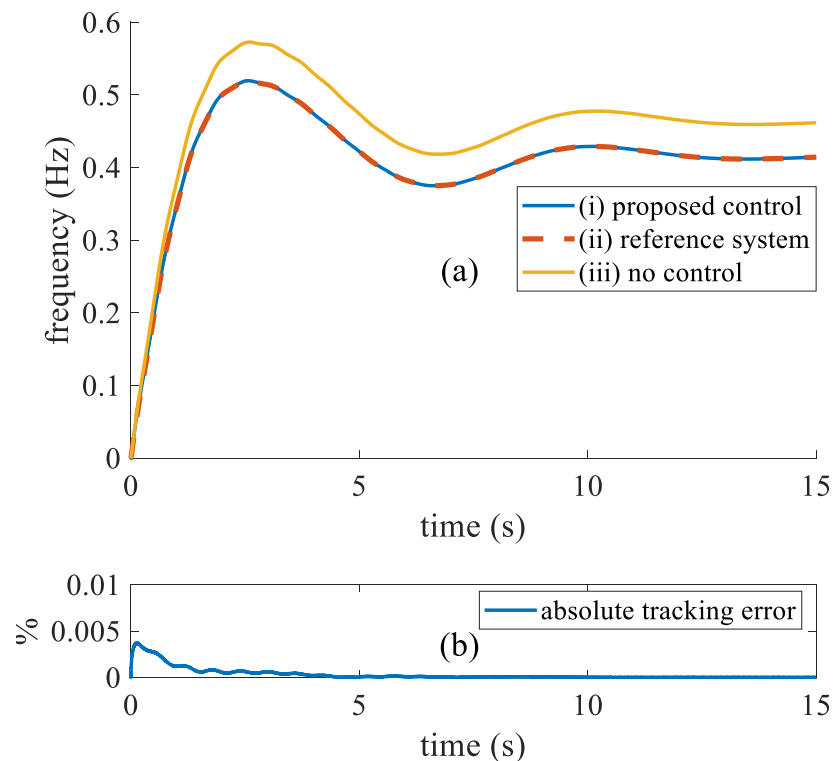


Figure 3.13. (a) Frequency response comparison with load drop; (b) Absolute error between test system frequency and reference system frequency.

generator's response with given inertia and droop. In our implementation, instead of using PI controller, we use LUT-based approach for achieving desired ΔP_{PV}^{ref} in de-loading control, and the derivative filter $H_\omega(s)$ (69) to obtain $\dot{\omega}$ for emulating inertial response. This alternative method is illustrated in Figure 3.14. To keep the same desired system equivalent inertia and droop as H^{ref} and R^{ref} using this method, the inertia and droop that the PV needs to emulate should be:

$$H^{alt} = H^{ref} - H_g, \quad \frac{1}{R^{alt}} = \frac{1}{R^{ref}} - \frac{1}{R_g} \quad (88)$$

where the H^{alt} and R^{alt} are with the same base S_b .

Then we implement this alternative method on the test system and simulate under the same 0.1 pu load disturbance. As seen from Figure 3.15, the frequency from alternative method does not accurately track the reference frequency response. It is also noted that, the alternative method actually results in over-compensation of the frequency response. Compared to the frequency response with proposed method, even though this over-compensation can slightly improve the RoCoF and nadir, it also comes with unnecessary cost. As illustrated in Figure 3.16, the alternative method requires 22.5% higher peak power response (0.45 MW) from PV than that of proposed method, which is 15% of the total available headroom (15% of MPP in this case). This difference is significant and can become more critical during worse events where the headroom is very limited. Therefore, if we consider the same desired frequency response capability under the same disturbance, the proposed method requires less power reserve to be de-loaded from the PV plant

than the alternative method. In other words, the proposed method demonstrates important economic advantage as well.

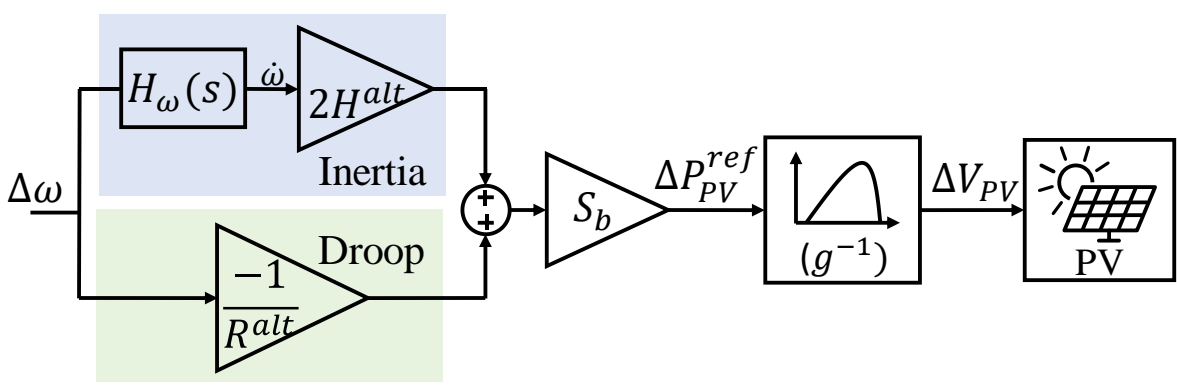


Figure 3.14. Conceptual diagram of the alternative method.

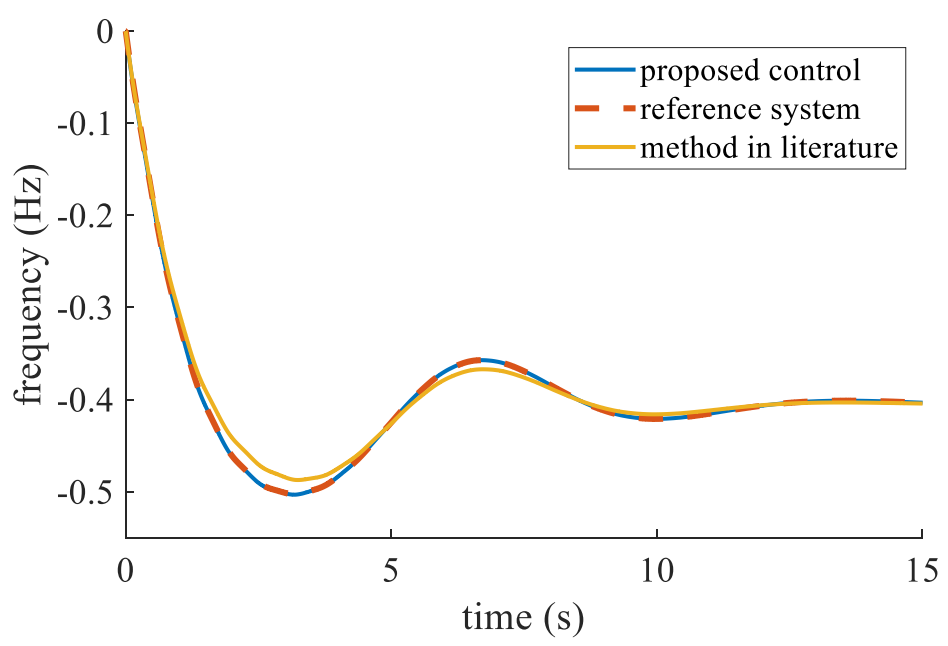


Figure 3.15. Frequency response comparison between proposed controller and alternative method.

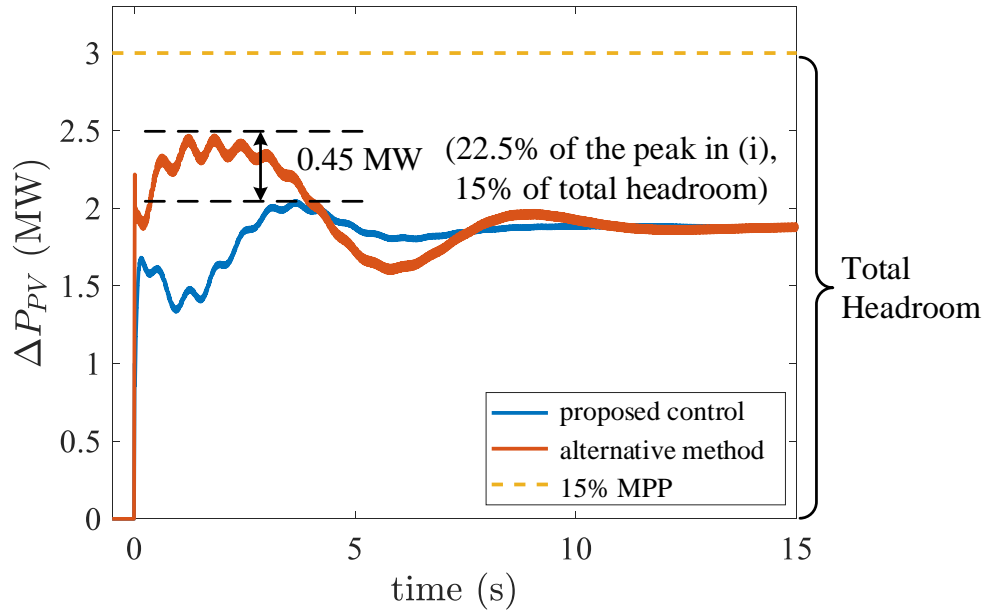


Figure 3.16. Comparison of ΔP_{PV} from the cases (a) with proposed control and (b) with alternative method.

3.3.4 Implementation

In this subsection, we discuss about some implementation issues about the proposed controller.

1) Frequency Measurement

As illustrated in Figure 3.1, the proposed controller relies on the feedback of system frequency. In simulations above, we assume it can be ideally obtained from generator speeds, but in practice it may not be easily available. One of the approaches to obtain this information is to use PLL's output frequency as an estimate of system frequency. However, since the input measurements are typically noisy, the output frequency from PLL is very likely to have noise. Noisy frequency can affect the performance of our controller, especially the UIO. As the common practice, a filter can be introduced for the controller to mitigate the noise impact.

To investigate the controller's performance in noisy environment, we corrupt the input measurement of PLL block in Simulink with white noise at signal-to-noise ratio of 50 dB. This results in PLL frequency having a peak steady-state oscillatory error of 12 mHz, which is at the average level as reported in [69, 70]. The noisy frequency is then passed to the controller through a second-order low-pass filter. We then repeat the simulation in which the load increases by 0.1 pu. As shown in Figure 3.17, the estimated disturbance does become noisy due to the noisy frequency. However, the estimation noise is not large and the estimated disturbance still closely follows the actual disturbance. For the controller performance, we can see from Figure 3.18 that the two system frequencies, both under the proposed controller but with and without noise, are very close to each other as the corresponding absolute error being less than 0.01%. Note that Figure 3.18 (a) compares the actual system frequencies from the two cases, not the PLL frequency measurements. This comparison implies that the normal frequency noise from PLL will not greatly affect the controller's performance.

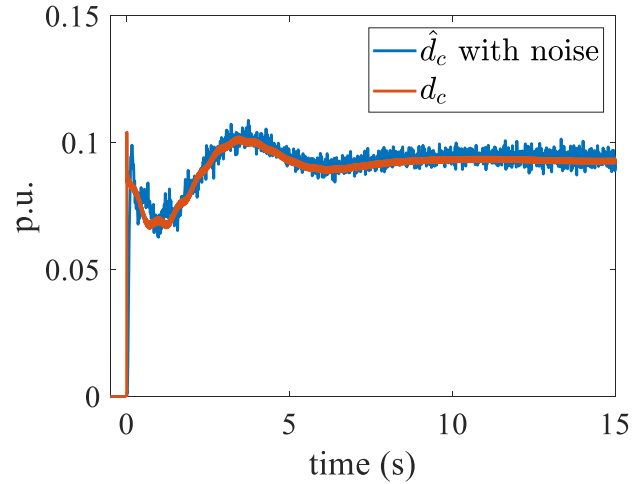


Figure 3.17. Comparison between the estimated disturbance with noise and the actual disturbance.

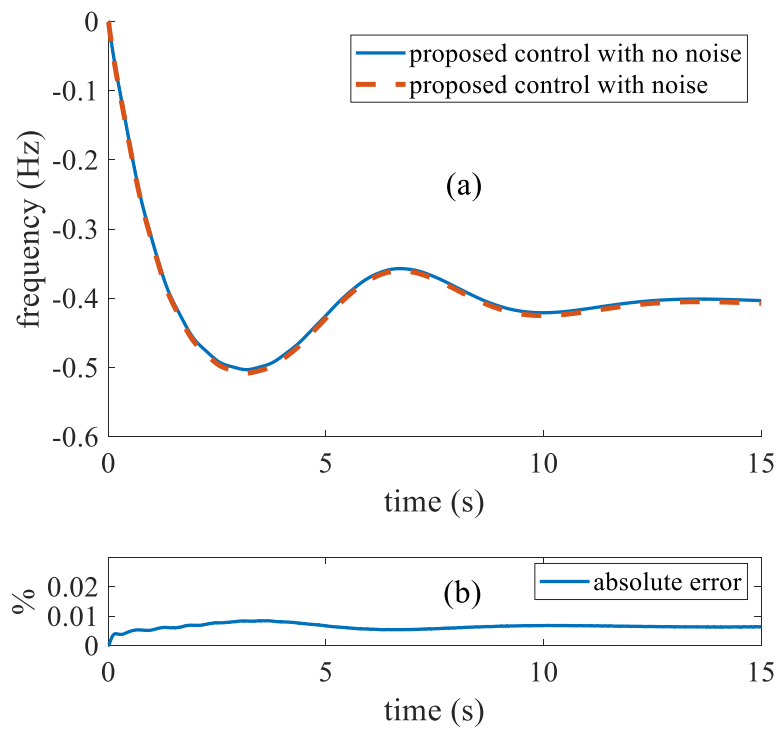


Figure 3.18. Under proposed controller, (a) comparison of system frequencies with and without noise; (b) corresponding absolute error.

2) Estimation of System Inertia

In practice, the system inertia may be subject to change due to different system operating conditions. Therefore, knowing the system inertia is required not only in the design stage, but also in the operation stage of the proposed controller. In this paper, we assume that the system operators can continuously monitor the on-line units so that the system equivalent inertia can be calculated using (56). A practical example is reported in [16] where ERCOT takes a network-model-driven approach to track on-line status of all synchronous resources and thus monitor the system inertia in real-time.

3) Scalability

The proposed controller is introduced earlier for one PV plant. When there are multiple PV plants, the proposed controller can still be adopted separately for each PV plant. Specifically, the controller designed for a new PV plant should be based on the updated LFC model which can represent the frequency response capability of the current system with all the other existing controllers, and the reference system for the new controller will also have the updated desired inertia and droop constants. In the meantime, the existing controllers do not need to be revised.

3.4 Conclusion

In this chapter, we propose a novel control method, designed from bulk-system-level, for PV plants to provide frequency support. In order to achieve the desired frequency response, a tracking LQR is designed to help system frequency accurately follow that from a reference system under the same load disturbance. The controller also contains a UIO from which both the system states and disturbance can be estimated. Test results strongly indicate the effectiveness the proposed control method by the very good performance of both frequency tracking and variable

estimation. Test results also show that the proposed method requires less de-loading of PV plant than the conventional method, which is of great significance in term of economics.

This chapter also introduces a new SSM for the three-phase two-stage PV system. This model is suitable for designing frequency support controls for PV and can be extended to a linear model for PV system with an LUT. Model validation results indicate that the SSM provides a close match of system dynamics with that of the detailed nonlinear PV system model.

CHAPTER 4 : FREQUENCY SUPPORT CONTROL SCHEME FOR DISTRIBUTED PV

In Chapter 3, we propose a frequency control scheme for large-scale PV plants. However, apart from large-scale PV plants, a considerable portion of the increasing PV installation are the small-size distributed PV in distribution systems which are projected to continue growing [30, 31]. Meanwhile, leveraging distributed PV for grid services has also become imperative, especially for small-scale power systems with high penetration of distributed PV. For example, the Hawaiian Electric is seeking frequency support from aggregators of distributed rooftop PV [71].

In this chapter, we focus on the use of small-scale distributed PV (such as rooftop PV) to provide similar frequency support function. Since distributed PV systems are easier to manage by aggregators (at community or distribution level), we consider a control scheme for a large group of distributed PV. The goal is to aggregate the small PV together to act like a large-scale PV plant with which control scheme can be designed to provide effective frequency support. In addition, aggregating distributed PV for control purpose can also simplify the control design and reduce the communication requirements. Following this approach, a fuzzy controller is proposed in [43] to regulate system frequency using distributed PV. However, the PV system model is simplified by neglecting control dynamics and only the insolation difference is considered among the PV systems.

The main challenge in aggregating a group of distributed PV, which are mainly single-phase, is the variation in their capacities, control parameters and working conditions. In this paper, we first propose a new reduced-order aggregate model to represent the overall dynamic behavior of a group of distributed PV by considering the variation among individual PV. Then, using this model, we adopt a frequency-tracking controller proposed in Chapter 3 to provide supervisory control for these distributed PV. This controller contains an unknown input observer (UIO) based

tracking LQR and an LUT. The main motivation of choosing this method is that it can assure the overall system frequency response to be as desired. In this proposed control scheme, which is illustrated in Figure 4.1, we also propose an effective inversion method to invert the aggregate control signal to individual ones for each PV system.

In the literature, however, there is limited work on aggregate models for PV systems. An aggregate model for distributed PV with synchronous power controllers is proposed in [72]. However, the electrical part of PV system is modeled as just a current source with a first-order filter. Considering full components, study in [73] derives an aggregate model but only for multiple identical PV systems. For the case with different parameters, order reduction techniques are only suggested but no further details or examples are provided. In this paper, we derive a reduced-order aggregate model which addresses the above shortcomings. The obtained aggregate model is very similar to the small-signal model (SSM) for one PV system and with the same order. Thus, the advantages are that, 1) model variables still have physical meanings which greatly facilitate control design and its implementation to real systems; 2) computation effort is reduced by retaining the same order as one PV system model.

The contributions of this chapter can be summarized as: 1) An aggregate model that can represent the dynamics of a group of distributed PV; 2) An aggregate-model-based control scheme for distributed PV to provide frequency support to the grid.

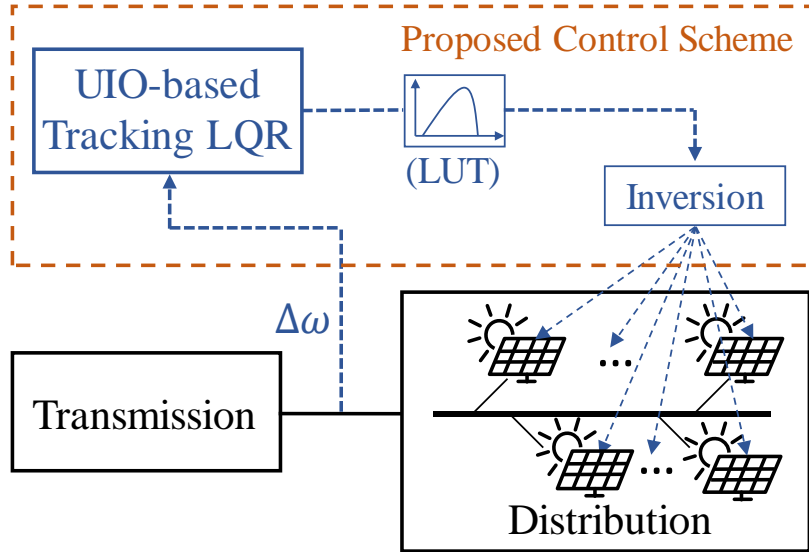


Figure 4.1. Conceptual diagram of proposed control scheme.

Section 4.1 of the paper introduces the new aggregate model. Section 4.2 summarizes the proposed controller and Section 0 provides the test results. Conclusions are included in Section 4.4.

4.1 System Modeling

In this section, we first introduce the SSM for one single-phase PV system. Then we derive its aggregate version for a group of distributed PV with different power ratings, control parameters, and solar irradiation. Then, a linear model for the combined system (plant for the controller) is presented in the last subsection.

4.1.1 The Single-phase Two-stage PV System

For one of the single-phase distributed PV, we consider it as a two-stage PV system whose topology is suitable for utilizing DC-link capacitor's energy as its control of DC-link voltage and

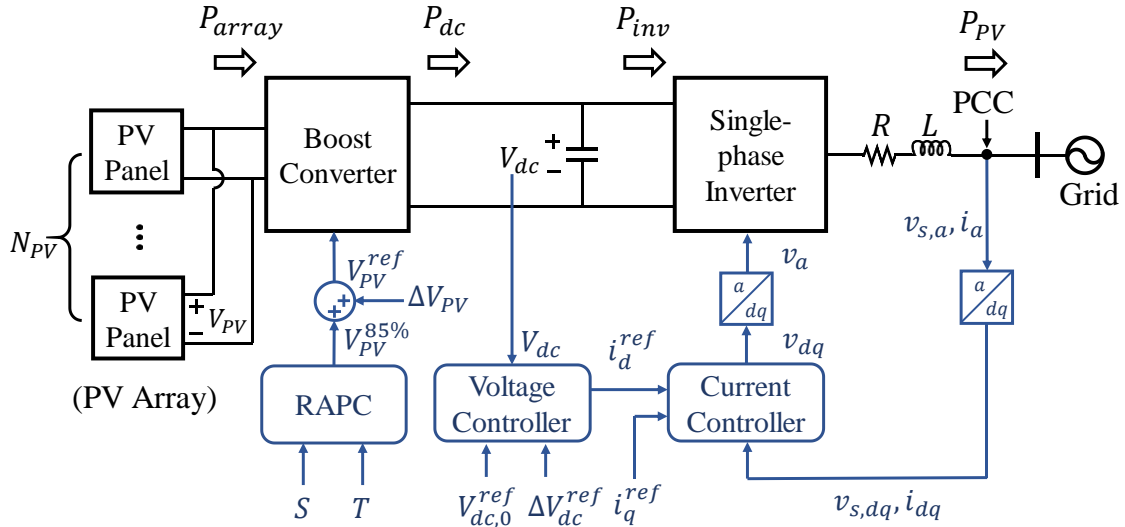


Figure 4.2. Diagram for one single-phase two-stage PV system.

PV array voltage are decoupled. In Figure 4.2, we illustrate the diagram for this PV system. For the electrical part, starting from the left, we assume the PV array consists of N_{PV} identical PV panels connected in parallel. Its terminal voltage V_{PV} is raised by a boost converter. The DC-link serving as the energy buffer is in between of the converter and a single-phase inverter. An $R - L$ filter is then used to interface with grid at point of common coupling (PCC).

We model the PV panel by its $P - V$ characteristic curve described by the function as [47]:

$$P_{array} = N_{PV} f(V_{PV}, S, T) = N_{PV} (n_p I_{ph} V_{PV} - n_p I_{rs} V_{PV} (e^{\frac{q V_{PV}}{k T A_i n_s}} - 1)) \quad (89)$$

For the DC-DC boost converter and single-phase inverter, we use average models without considering switching details. Therefore, by ignoring losses, we have the average power balance equations as follows:

$$P_{array} = P_{dc}, \quad P_{inv} = P_{PV} \quad (90)$$

where P_{dc} and P_{inv} are the power flowing into and out of the DC-link. P_{PV} is the power output injected to the grid. Note that, at bulk system level, the frequency is determined by the average power balance. If we consider the group of PV to be evenly distributed among three phases, their

impact to the frequency also depends on the total average power, which is equivalent to the sum of average power from each phase. Therefore, for each single-phase PV, we focus on the average power, instead of instantaneous power, to capture its link to the system frequency.

Similarly, we can model the DC-link dynamics in terms of the power balance as:

$$\frac{C}{2} \left(\frac{dV_{dc}^2}{dt} \right) = P_{dc} - P_{inv} = P_{array} - P_{PV} \quad (91)$$

where the DC-link voltage is also the averaged value over the same period ($\frac{1}{120}$ s). For notational simplicity, we still denote this averaged voltage as V_{PV} . In (91), P_{PV} can be further expressed in d-q frame as:

$$P_{PV} = \frac{1}{2} (i_d v_{sd} + i_q v_{sq}) = \frac{1}{2} i_d v_{sd} \quad (92)$$

in which i_d , i_q and v_{sd} , v_{sq} are the dq components of current and voltage at point of common coupling, respectively. Different than three-phase, single-phase dq transformation often requires creating an imaginary β component which is orthogonal to the system voltage [74]. Then $\alpha\beta - dq$ transformation is performed with the help of the phase-locked loop (PLL). Here in the modeling, we assume the ideal PLL and the dq components can be directly obtained. The PLL also regulates v_{sq} to zero and thus the simplification in (92) can be made.

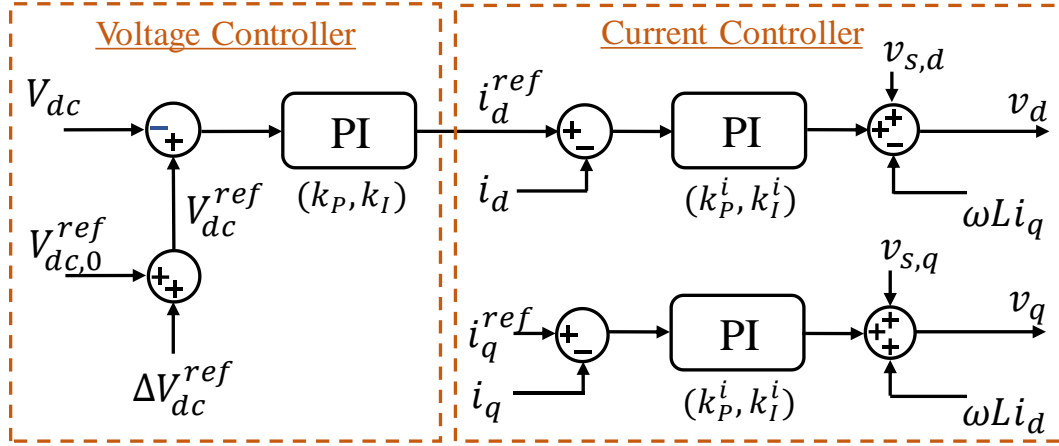


Figure 4.3. Diagram of the dual-loop current mode controller.

Combing (89)-(92) and expanding the left-hand-side (LHS) derivative term, the power balance equation becomes:

$$CV_{dc} \left(\frac{dV_{dc}}{dt} \right) = N_{PV} f(V_{PV}, S, T) - \frac{1}{2} i_d v_{sd} \quad (93)$$

For the local control of PV system, we adopt the same control scheme as used for three-phase two-stage PV system in Chapter 3. In this control scheme, as shown in Figure 4.2, the rapid active power control (RAPC) method from [22] is used at boost converter to determine the operating point of PV array. Other than commonly used MPPT control, RAPC sets the default operating voltage of PV at a de-loaded level (corresponding to 85% of the MPP in our case). Then we include control input ΔV_{PV} from supervisory control which can be used to adjust the PV power output. Since RAPC is an LUT-based approach and we neglect switching details of converter, we assume the final voltage set-point V_{PV}^{ref} can be ideally achieved without any dynamics. For the inverter control, a revised dual-loop current mode controller is adopted and illustrated in Figure 4.3. ΔV_{dc}^{ref} is included in this controller as the control input with which we can control the power released (or absorbed) from the capacitor. The feedforward compensation scheme from [47] is used at inner current control loop to decouple the current control dynamics from grid voltage and

also the output filter. Following the derivation in Chapter 3 and choosing the PI controller parameters for current loop as

$$k_P^i = \frac{L}{\tau}, k_I^i = \frac{R}{\tau} \quad (94)$$

we can describe the controller dynamics by:

$$\frac{di_d}{dt} = -\frac{1}{\tau}i_d - \frac{k_P}{\tau}V_{dc} + \frac{k_P}{\tau}V_{dc}^{ref} + \frac{1}{\tau}x \quad (95)$$

$$\frac{di_q}{dt} = -\frac{1}{\tau}i_q + \frac{1}{\tau}i_q^{ref} \quad (96)$$

$$\frac{dx}{dt} = -k_I V_{dc} + k_I V_{dc}^{ref} \quad (97)$$

where τ is the current control time constant which we choose to be sufficiently small and x is the controller state which we introduce to avoid second-order derivative of the state. Equations (95)-(97), along with (93), represent the original nonlinear model of one single-phase two-stage PV system.

Next, we derive the SSM through linearization of the original model. Let us consider (93) and approximate the V_{dc} in LHS coefficient and v_{sd} by their nominal values $V_{dc,0}^{ref}$ and V_{sd} which are constants. Therefore, the linearization of (93) is given as:

$$\frac{d\Delta V_{dc}}{dt} = \frac{1}{CV_{dc,0}^{ref}} \left(\underbrace{N_{PV}g(\Delta V_{PV}, S, T)}_{\Delta P_{array}} - \frac{1}{2} \underbrace{\Delta i_d V_{sd}}_{\Delta P_{PV}} \right) \quad (98)$$

where the function $g(\Delta V_{PV}, S, T)$ represents for a LUT which maps the change of PV array voltage to the change of PV panel's output power under given conditions. The reason of using LUT is that function f is highly nonlinear and analytical linearization can result in considerable error.

Following the same idea as in Chapter 3, we want to modify the state Δi_d into ΔP_{PV} as we are more interested in the increment of power. Therefore, we multiply both sides of (95) by $\frac{1}{2}V_{sd}$ and linearize it, we have:

$$\frac{d\Delta P_{PV}}{dt} = -\frac{1}{\tau}\Delta P_{PV} - \frac{k_P V_{sd}}{2\tau}\Delta V_{dc} + \frac{k_P V_{sd}}{2\tau}\Delta V_{dc}^{ref} + \frac{V_{sd}}{2\tau}\Delta x \quad (99)$$

Equation (96) is ignored as the i_q dynamics is independent of others and its reference is set to zero. For (97), it can be easily linearized as:

$$\frac{d\Delta x}{dt} = -k_I\Delta V_{dc} + k_I\Delta V_{dc}^{ref} \quad (100)$$

Equations (98)-(100) complete our SSM for a two-stage single-phase PV system.

4.1.2 The Reduced-order Aggregate Model

Let $\mathcal{P} = \{1, 2, 3, \dots, N\}$ denote the set of distributed PV in an area of distribution system.

For one PV system $i \in \mathcal{P}$, we have its SSM in the form of:

$$\frac{d\Delta V_{dc,i}}{dt} = \frac{1}{C_i V_{dc,0,i}^{ref}} \left(\frac{P_{r,i}}{P_{pa}} g_i(\Delta V_{PV,i}, S_i, T_i) - \Delta P_{PV,i} \right) \quad (101)$$

$$\frac{d\Delta P_{PV,i}}{dt} = -\frac{1}{\tau_i}\Delta P_{PV,i} - \frac{k_{P,i} V_{sd,i}}{2\tau_i}\Delta V_{dc,i} + \frac{k_{P,i} V_{sd,i}}{2\tau_i}\Delta V_{dc,i}^{ref} + \frac{V_{sd,i}}{2\tau_i}\Delta x_i \quad (102)$$

$$\frac{d\Delta x_i}{dt} = -k_{I,i}\Delta V_{dc,i} + k_{I,i}\Delta V_{dc,i}^{ref} \quad (103)$$

where $P_{r,i}$ and $P_{pa,i}$ are the rated power of the PV system and one PV panel, respectively, and $N_{PV,i} = P_{r,i}/P_{pa,i}$. Before aggregating the SSMs for all PV systems in \mathcal{P} , we need to make a few assumptions on the parameters in the above model.

a.1) PV Panel

It is assumed that the basic unit of PV array, PV panel, is the same for all PV systems in \mathcal{P} . Therefore, for the rated power and characteristic functions, we have $\forall i \in \mathcal{P}$:

$$P_{pa,i} = P_{pa} \quad (104)$$

$$g_i(\Delta V_{PV,i}, S_i, T_i) = g(\Delta V_{PV,i}, S_i, T_i) \quad (105)$$

a.2) Environment

Since the distributed PV are within the same area of distribution system, the ambient temperature for PV array does not vary a lot. So, $\forall i \in \mathcal{P}$:

$$T_i = T \quad (106)$$

For solar irradiance, however, we keep the variance among each PV system because the cloud distribution can be different within the area.

a.3) System Voltage

To ensure proper functionality of the connected equipment, the voltage in a distribution system needs to be regulated within a close range around its nominal value. For example, the ANSI C84.1 standard [75] requires voltage range in distribution to be 0.95 p.u. – 1.05 p.u.. In this case, we assume the system voltage is well-regulated across the distribution network and thus neglect the small variations. Therefore, $\forall i \in \mathcal{P}$:

$$V_{sd,i} = V_{sd} \quad (107)$$

a.4) Control Parameters

The first control parameter under assumption is the $V_{dc,0,i}^{ref}$, which sets the nominal value of DC-link voltage. The choice of this voltage mainly depends on the magnitude of inverter output voltage. Since all the PV systems are in the same distribution system with the same voltage level, we assume identical DC-link voltage references for each one and $\forall i \in \mathcal{P}$:

$$V_{dc,0,i}^{ref} = V_{dc,0}^{ref} \quad (108)$$

The other parameter is the current control loop time constant τ_i . According to [47], τ_i has to be chosen as a very small value (e.g. 0.001) such that the current loop is sufficiently fast to

incorporate with outer voltage loop. Therefore, comparing to the parameters in the slower voltage loop ($k_{P,i}, k_{I,i}$), we decide to neglect the variations on the fast current loop time constants because the former ones are more dominant in system dynamics. So, $\forall i \in \mathcal{P}$:

$$\tau_i = \tau \quad (109)$$

a.5) DC-link Capacitor

The DC-link capacitor also serves as the output capacitor for the boost converter. A common practice of choosing the capacitance is to stabilize DC-link voltage such that the voltage ripples are within a desired range [76, 77]. Following the design in [77], $\forall i \in \mathcal{P}$, we have:

$$C_i = P_{r,i} \frac{D_i^{max} \times T_{s,i}^{max}}{\alpha_i \% \times V_{dc,i}^2} = P_{r,i} \frac{D^{max} \times T_s^{max}}{\underbrace{\alpha \% \times (V_{dc,0}^{ref})^2}_{constant}} = P_{r,i} \times C_d \quad (110)$$

where $D_i^{max} \times T_{s,i}^{max}$ are the maximum values of the boost converter's duty cycle and switching period, respectively, which we assume to be the same for each PV system. The maximum voltage ripple level, $\alpha_i \%$, is also chosen to be the same. Moreover, if we use its nominal value, $V_{dc,0}^{ref}$, to represent the DC-link voltage, as shown in (110), the capacitance, C_i , for the i -th PV system can be written as a product of the rated power, $P_{r,i}$, and a constant unit capacitance, C_d .

Now with aforementioned assumptions (104)-(110), the SSM described in (101)-(103) becomes:

$$P_{r,i} \frac{d\Delta V_{dc,i}}{dt} = \frac{P_{r,i}}{C_d V_{dc,0}^{ref} P_{pa}} g_i(\Delta V_{PV,i}, S_i, T_i) - \frac{1}{C_d V_{dc,0}^{ref}} \Delta P_{PV,i} \quad (111)$$

$$\frac{d\Delta P_{PV,i}}{dt} = -\frac{1}{\tau} \Delta P_{PV,i} - \frac{k_{P,i} V_{sd}}{2\tau} \Delta V_{dc,i} + \frac{k_{P,i} V_{sd}}{2\tau} \Delta V_{dc,i}^{ref} + \frac{V_{sd}}{2\tau} \Delta x_i \quad (112)$$

$$\frac{d\Delta x_i}{dt} = -k_{I,i} \Delta V_{dc,i} + k_{I,i} \Delta V_{dc,i}^{ref} \quad (113)$$

Next, to obtain the aggregate model, we first define some aggregate variables as:

$$\begin{aligned}
P_r^a &= \sum_{i \in \mathcal{P}} P_{r,i}, \quad \Delta P_{PV}^a = \sum_{i \in \mathcal{P}} \Delta P_{PV,i}, \quad \Delta x^a = \sum_{i \in \mathcal{P}} \Delta x_i \\
\Delta V_{dc}^a &= \frac{\sum_{i \in \mathcal{P}} P_{r,i} \Delta V_{dc,i}}{\sum_{i \in \mathcal{P}} P_{r,i}}, \quad \Delta V_{dc}^{ref,a} = \frac{\sum_{i \in \mathcal{P}} P_{r,i} \Delta V_{dc,i}^{ref}}{\sum_{i \in \mathcal{P}} P_{r,i}} \\
\Delta V_{PV}^a &= \frac{\sum_{i \in \mathcal{P}} P_{r,i} \Delta V_{PV,i}}{\sum_{i \in \mathcal{P}} P_{r,i}}, \quad S^a = \frac{\sum_{i \in \mathcal{P}} P_{r,i} S_i}{\sum_{i \in \mathcal{P}} P_{r,i}}
\end{aligned}$$

Then by summing up the SSMs of all PV systems in \mathcal{P} and replacing some summations by the aggregate variables, we can obtain:

$$\frac{d\Delta V_{dc}^a}{dt} = \frac{1}{C_d V_{dc,0}^{ref} P_{pa}} \underbrace{\frac{\sum_{i \in \mathcal{P}} P_{r,i} g(\Delta V_{PV,i}, S_i, T)}{P_r^a}}_{S.1} - \frac{1}{C_d V_{dc,0}^{ref} P_r^a} \Delta P_{PV}^a \quad (114)$$

$$\frac{d\Delta P_{PV}^a}{dt} = -\frac{1}{\tau} \Delta P_{PV}^a - \frac{V_{sd}}{2\tau} \underbrace{\sum_{i \in \mathcal{P}} k_{P,i} \Delta V_{dc,i}}_{S.2} + \frac{V_{sd}}{2\tau} \underbrace{\sum_{i \in \mathcal{P}} k_{P,i} \Delta V_{dc,i}^{ref}}_{S.3} + \frac{V_{sd}}{2\tau} \Delta x^a \quad (115)$$

$$\frac{d\Delta x^a}{dt} = -\underbrace{\sum_{i \in \mathcal{P}} k_{I,i} \Delta V_{dc,i}}_{S.4} + \underbrace{\sum_{i \in \mathcal{P}} k_{I,i} \Delta V_{dc,i}^{ref}}_{S.5} \quad (116)$$

In (114)-(116), there are still some summation terms (S.1-S.5) on the right-hand-side (RHS) which mean that the model's order has not been fully reduced. Therefore, we want to further represent these summation terms with aggregate variables to reduce the order. In the following, we will discuss about the corresponding treatments for each of them.

b.1) S.1

Considering the variables in this summation and their defined aggregate versions, we approximate S.1 as:

$$\frac{\sum_{i \in \mathcal{P}} P_{r,i} g(\Delta V_{PV,i}, S_i, T)}{P_r^a} \approx g(\Delta V_{PV}^a, S^a, T) \quad (117)$$

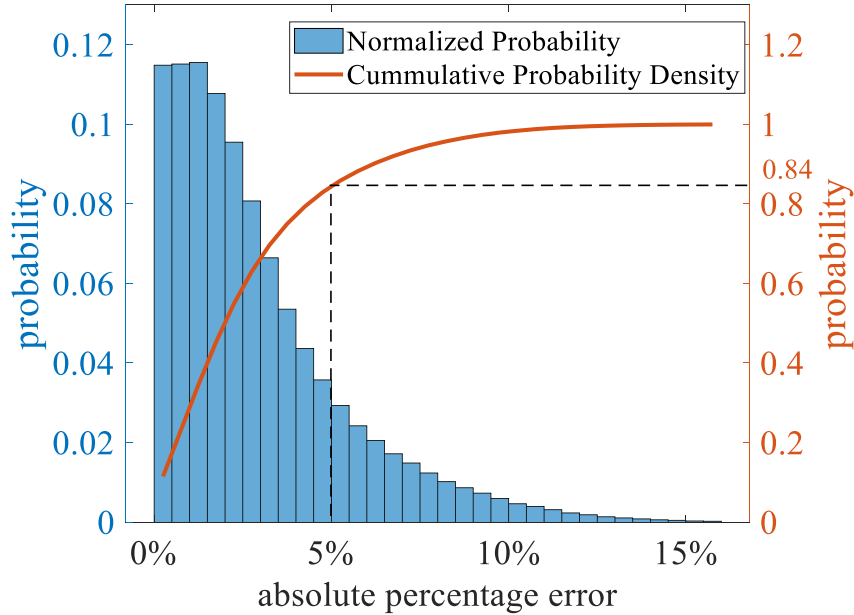


Figure 4.4. Probability distribution of the absolute percentage approximation error from MCS.

The original summation on the LHS of (117) is basically taking the weighted average of each PV's g function value with respect to their power ratings. So the idea of this approximation is to move the weighted averaging into g on the variables $\Delta V_{PV,i}$ and S_i . Since the function g represents an LUT, it is very difficult to mathematically evaluate the error of this approximation. Therefore, we take the numerical approach, which is Monte Carlo simulation (MCS), to demonstrate the error level.

In order to conduct MCS, we first assume that all the variables ($P_{r,i}$, $\Delta V_{PV,i}$ and S_i) follow normal distributions with certain means and variances. Moreover, to enhance the credibility of MCS, we consider the means and variances to be random samples from corresponding uniform distributions. Details about the distributions are summarized in Table 4.1. Note that, for $\Delta V_{PV,i}$, we choose the distribution of μ_V and σ_V such that most of the $\Delta V_{PV,i}$ samples are within $[\Delta V_{PV}^{+15\%}, 0]$, where $\Delta V_{PV}^{+15\%}$ is the voltage change corresponding to $15\%P^{MPP}$ in ΔP_{array} . In addition, we only

sample from either $[\Delta V_{PV}^{+15\%}, 0]$ or $[0, \Delta V_{PV}^{-15\%}]$ because, with the considered frequency support control function, it is not likely to have certain PV systems increase power while others decrease power at the same time. Since $[0, \Delta V_{PV}^{-15\%}]$ is shorter than $[\Delta V_{PV}^{+15\%}, 0]$, here we consider the later one as the worst case and conduct MCS.

Table 4.1. Variable Distributions and Corresponding Parameters.

| | | |
|-------------------|---|--|
| $P_{r,i}$ | $P_{r,i} \sim \mathcal{N}(\mu_p, \sigma_p^2)$ | $\mu_p \sim \mathcal{U}(150000, 250000),$ $\sigma_p \sim \mathcal{U}(10, 30)$ |
| $\Delta V_{PV,i}$ | $\Delta V_{PV,i} \sim \mathcal{N}(\mu_v, \sigma_v^2)$ | $\mu_v \sim \mathcal{U}(-30, -7.5),$ $\sigma_v \sim \mathcal{U}(2, 7)$ |
| S_i | $S_i \sim \mathcal{N}(\mu_s, \sigma_s^2)$ | $\mu_s \sim \mathcal{U}(40, 70),$ $\sigma_s \sim \mathcal{U}(1, 10)$ |

In the MCS, we set the number of trials to be 500,000. At each trial, we sample 50 sets of the three variables and compute the approximation error for (117). Figure 4.4 shows the probability distribution of calculated absolute percentage error, as well as the cumulative probability density curve. From the plot, the error is very small for most of the cases, and we have the probability of 84% to get an error below 5%. Therefore, (117) is a good approximation with satisfactory accuracy.

b.2) S.2-S.5

Summation terms S.2-S.5 are discussed together because they share the same structure, as well as their corresponding aggregate variables. Therefore, the same treatment can be applied to all of them. Taking S.2 as an example and we have:

$$\sum_{i \in \mathcal{P}} k_{P,i} \Delta V_{dc,i} = \sum_{i \in \mathcal{P}} \frac{k_{P,i}}{P_{r,i}} P_r^a \Delta V_{dc}^a - \sum_{i \in \mathcal{P}} \left(\sum_{j \in \mathcal{P}, j \neq i} \frac{k_{P,j}}{P_{r,j}} \right) P_{r,i} \Delta V_{dc,i} \quad (118)$$

From (118), we wish that $\sum_{j \in \mathcal{P}, j \neq i_1} \frac{k_{P,j}}{P_{r,j}} = \sum_{j \in \mathcal{P}, j \neq i_2} \frac{k_{P,j}}{P_{r,j}}, \forall i_1, i_2 \in \mathcal{P}$. If the desired equation holds, it implies that

$$\frac{k_{P,i}}{P_{r,i}} = c_P, \forall i \in \mathcal{P} \quad (119)$$

where c_P is a constant parameter. However, equation (119) may not hold in practice. Therefore, we want to find the value of c_P which can minimize the Euclidean norm of the error between each $\frac{k_{P,i}}{P_{r,i}}$ and c_P . To achieve this, we may construct an optimization problem to determine c_P as follows:

$$\text{Minimize}_{c_P} \sum_{i \in \mathcal{P}} \left(c_P - \frac{k_{P,i}}{P_{r,i}} \right)^2 \quad (120)$$

Solving the optimization problem in (120), we can obtain:

$$c_P = \frac{\sum_{i \in \mathcal{P}} \left(\frac{k_{P,i}}{P_{r,i}} \right)}{|\mathcal{P}|} \quad (121)$$

where $|\mathcal{P}|$ is the cardinality of set \mathcal{P} . Substitute (119) into (118) to obtain:

$$\sum_{i \in \mathcal{P}} k_{P,i} \Delta V_{dc,i} \approx c_P P_r^a \Delta V_{dc}^a \quad (122)$$

where S.2 has been successfully expressed by the aggregate variables. The same treatment can also be adopted on S.3-S.5 to have:

$$\sum_{i \in \mathcal{P}} k_{P,i} \Delta V_{dc,i}^{ref} \approx c_P P_r^a \Delta V_{dc}^{ref,a} \quad (123)$$

$$\sum_{i \in \mathcal{P}} k_{I,i} \Delta V_{dc,i} \approx c_I P_r^a \Delta V_{dc}^a \quad (124)$$

$$\sum_{i \in \mathcal{P}} k_{l,i} \Delta V_{dc,i}^{ref} \approx c_l P_r^a \Delta V_{dc}^{ref,a} \quad (125)$$

where

$$c_l = \frac{\sum_{i \in \mathcal{P}} \left(\frac{k_{l,i}}{P_{r,i}} \right)}{|\mathcal{P}|} \quad (126)$$

Now we have the reduced-order aggregate model as:

$$\frac{d\Delta V_{dc}^a}{dt} = \frac{1}{C_d V_{dc,0}^{ref} P_{pa}} g(\Delta V_{PV}^a, S^a, T) - \frac{1}{C_d V_{dc,0}^{ref} P_r^a} \Delta P_{PV}^a \quad (127)$$

$$\frac{d\Delta P_{PV}^a}{dt} = -\frac{1}{\tau} \Delta P_{PV}^a - \frac{V_{sd}}{2\tau} c_p P_r^a \Delta V_{dc}^a + \frac{V_{sd}}{2\tau} c_p P_r^a \Delta V_{dc}^{ref,a} + \frac{V_{sd}}{2\tau} \Delta x^a \quad (128)$$

$$\frac{d\Delta x^a}{dt} = -c_l P_r^a \Delta V_{dc}^a + c_l P_r^a \Delta V_{dc}^{ref,a} \quad (129)$$

We can notice that, comparing to the SSM of one PV system (51)-(53), the derived aggregate model in (127)-(129) is in a very similar structure and also with the same order. In other words, the collective dynamics of a group of distributed PV can be viewed as that of one large-scale PV system described by the reduced-order aggregate model. Furthermore, the aggregate states and input correspond to physical quantities which can facilitate the later control design, such as ΔP_{PV}^a , which is the total increment power of the distributed PV. The state ΔP_{PV}^a , which is chosen as the model's output, can also represent for the coupling among individual PVs.

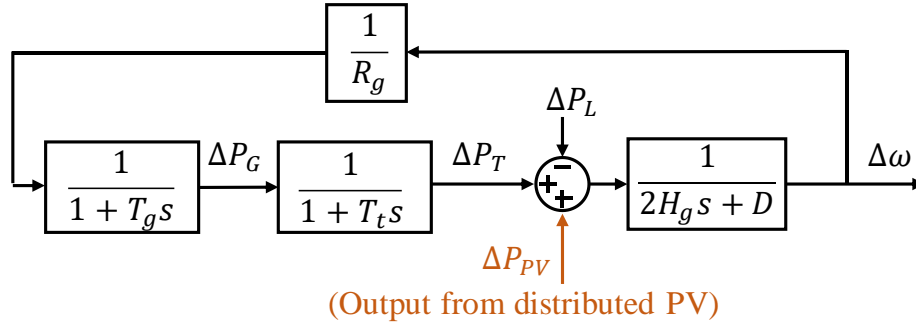


Figure 4.5. LFC model including distributed PV.

4.1.3 Transmission System

We use the classical load frequency control (LFC) model to describe the real power and frequency dynamics in transmission system. Here since we focus on primary frequency response, the automatic generation control (AGC) system is not included. We also revised the LFC model to incorporate distributed PV, as shown in Figure 4.5.

Define \mathcal{G} as the set of all synchronous generators in this system. Then the equivalent inertia and droop constants for the multi-machine LFC model can be obtained as:

$$H_g = \frac{\sum_{i \in \mathcal{G}} S_i H_i}{\sum_{i \in \mathcal{G}} S_i}, \quad \frac{1}{R_g} = \frac{\sum_{i \in \mathcal{G}} S_i / R_i}{\sum_{i \in \mathcal{G}} S_i} \quad (130)$$

where S_i denotes the capacity of generator i . For the governor and turbine dynamics, we assume the same time constants T_g and T_t for all generators in \mathcal{G} . Therefore, the LFC model shown in for transmission system can be written as:

$$\begin{cases} \dot{\mathbf{x}}_g = \mathbf{A}_g \mathbf{x}_g + \mathbf{B}_g \mathbf{u}_g + \mathbf{E}_g \mathbf{d}_g \\ \mathbf{y}_g = \mathbf{C}_g \mathbf{x}_g \end{cases} \quad (131)$$

where we treat the increment power ΔP_{PV} from distributed PV as an input (\mathbf{u}_g) to the transmission system whereas the load change ΔP_L is taken as the disturbance (\mathbf{d}_g).

4.2 Proposed Control Scheme

In this section, we introduce the proposed control scheme which contains three main components: a UIO-based tracking LQR, an LUT, and an inversion function, as illustrated in Figure 4.1. The tracking LQR is designed to assure that the system frequency can effectively track that of a reference system with given inertia and droop constants (H^{ref} and R^{ref}), under the same unknown disturbance. So that the desired close-loop frequency response capability is achieved. The LUT is introduced to remove the nonlinearity in the aggregate PV system model and thus obtain a linear plant model for designing the tracking LQR. At last, the inversion function inverts the aggregate control signal, which corresponds to the aggregate model, to individual ones for each distributed PV.

This control scheme is similar to the one in Chapter 3 where the UIO-based tracking LQR is proposed for frequency support from the large-scale PV plant. However, the differences between our work and Chapter 3 are that, 1) a new reduced-order aggregate model is developed and adopted in the tracking LQR for frequency support from distributed PV; 2) an inversion method is developed to obtain the individual control input. In the following subsections, we discuss each component in detail.

4.2.1 LUT and the Combined System Model

The derived reduced-order aggregate model in (127)-(129) still contains a nonlinear term which is the LUT function $g(\Delta V_{PV}^a, S^a, T)$. However, for the LQR design, a linear plant model is preferred. Therefore, consider another LUT function which is the inverse of g :

$$\Delta V_{PV}^a = g^{-1}(\Delta P_{PV}^{ref,a}, S^a, T) \quad (132)$$

We can substitute (132) into (127) to get rid of the nonlinearity and obtain a linear model which can be written in the state-space form as:

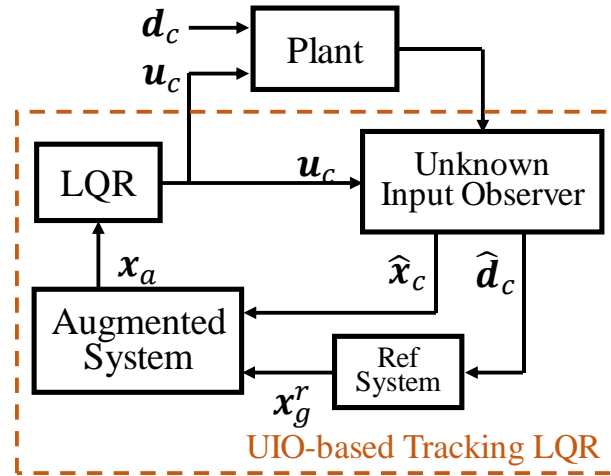


Figure 4.6. Architecture and components of the UIO-based tracking LQR.

$$\begin{cases} \dot{\mathbf{x}}_{PV} = \mathbf{A}_{PV}\mathbf{x}_{PV} + \mathbf{B}_{PV}\mathbf{u}_{PV} \\ \mathbf{y}_{PV} = \mathbf{C}_{PV}\mathbf{x}_{PV} \end{cases} \quad (133)$$

where $\mathbf{x}_{PV} = [\Delta V_{dc}^a \ \Delta P_{PV}^a \ \Delta x^a]^T$, $\mathbf{u}_{PV} = [\Delta P_{PV}^{ref,a} \ \Delta V_{dc}^{ref,a}]^T$, and $\mathbf{y}_{PV} = [\Delta P_{PV}^a]$.

Now we can combine the two linear models for both transmission system (57) and distributed PV (with an LUT) (133) through the interfacing variable ΔP_{PV}^a . The obtained model is referred to as the combined system model, which is used as the plant model for the following design of tracking LQR. The combined system model can also be described in state-space as:

$$\begin{aligned} \underbrace{\begin{bmatrix} \dot{\mathbf{x}}_g \\ \dot{\mathbf{x}}_{PV} \end{bmatrix}}_{\dot{\mathbf{x}}_c} &= \underbrace{\begin{bmatrix} \mathbf{A}_g & \mathbf{B}_g \mathbf{C}_{PV} \\ 0 & \mathbf{A}_{PV} \end{bmatrix}}_{\mathbf{A}_c} \underbrace{\begin{bmatrix} \mathbf{x}_g \\ \mathbf{x}_{PV} \end{bmatrix}}_{\mathbf{x}_c} + \underbrace{\begin{bmatrix} 0 \\ \mathbf{B}_{PV} \end{bmatrix}}_{\mathbf{B}_c} \underbrace{\begin{bmatrix} \mathbf{u}_{PV} \end{bmatrix}}_{\mathbf{u}_c} \\ &+ \underbrace{\begin{bmatrix} \mathbf{E}_g \\ 0 \end{bmatrix}}_{\mathbf{E}_c} \underbrace{\begin{bmatrix} \mathbf{d}_g \\ \mathbf{d}_c \end{bmatrix}}_{\mathbf{d}_c} \end{aligned} \quad (134)$$

$$\mathbf{y}_c = \mathbf{C}_c \mathbf{x}_c \quad (135)$$

where the output \mathbf{y}_c is frequency deviation $\Delta\omega$.

4.2.2 The UIO-based Tracking LQR

As noted earlier, the control objective is to let the system frequency track that of a reference system under the same load disturbance. Since this is essentially a tracking problem, we can adopt LQR to minimize the tracking error. However, to obtain the proper tracking reference in this case, the load disturbance must be estimated. To address this difficulty, the adopted method uses a UIO, and the resulting control architecture is shown in Figure 4.6, which also contains the reference system, an augmented system, and an LQR.

Different than the conventional observers with Luenberger structure, the UIO can effectively estimate the system states with the presence of unknown disturbances. Moreover, the disturbance can also be estimated from UIO with the input and output information [63, 64]. The estimated disturbance, $\hat{\mathbf{d}}_c$, is sent to a reference system to generate tracking reference. The reference system represents a “desired version” of the transmission system with desired inertia and droop constants. Therefore, by following the frequency of this reference system, the close-loop system frequency response can be improved to the desired level. With the reference state, \mathbf{x}_g^r , and estimated plant states, $\hat{\mathbf{x}}_c$, the augmented system can be formed, which contains the tracking error and its integral. Then, a standard LQR can be designed based on this augmented system to minimize and eventually eliminate the tracking error. Further details about the design can be found in Chapter 3.

4.2.3 Inversion of Control Signal

As illustrated in Figure 4.6, the UIO-based tracking LQR is designed for the combined system (plant). Therefore, the control signals should also correspond to the inputs of the combined

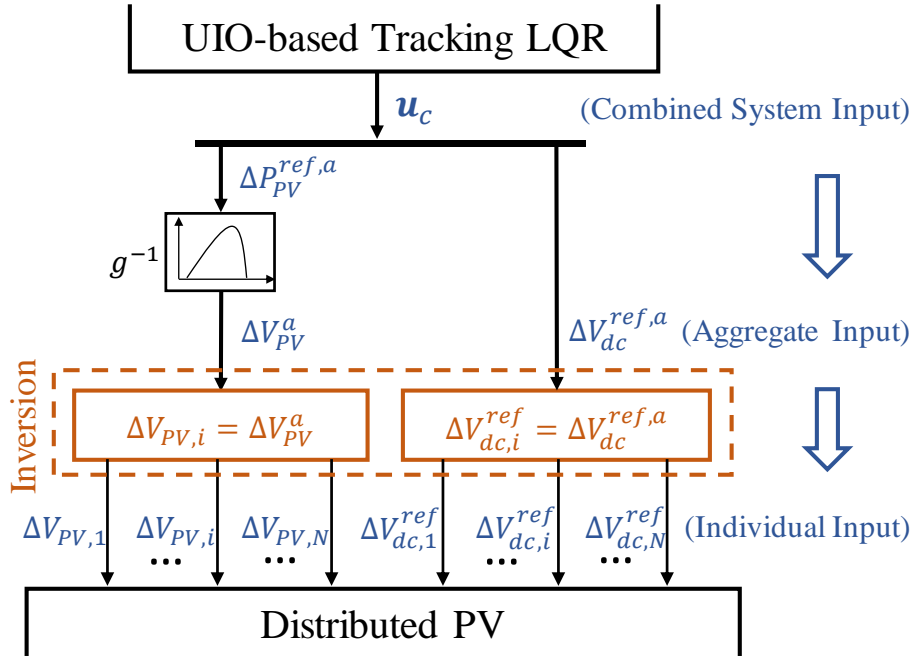


Figure 4.7. Inversion of control signals.

system model. From (134), the control input \mathbf{u}_c is actually \mathbf{u}_{PV} which comprises two inputs: $\Delta P_{PV}^{ref,a}$ and $\Delta V_{dc}^{ref,a}$, where $\Delta P_{PV}^{ref,a}$ is to be converted to ΔV_{PV}^a by the LUT function g^{-1} . So eventually, the control signals \mathbf{u}_c are mapped to aggregate inputs ($\mathbf{u}^a = [\Delta V_{PV}^a \ \Delta V_{dc}^{ref,a}]^T$) in the aggregate model. However, to implement the controller, we need to obtain the individual control input ($\mathbf{u}_i = [\Delta V_{PV,i} \ \Delta V_{dc,i}^{ref}]^T$) for each of the distributed PV.

Unfortunately, there is no unique way of inverting \mathbf{u}^a back to \mathbf{u}_i , by the definition of \mathbf{u}^a . In other words, any inversion would work, as long as satisfying the definition of \mathbf{u}^a . However, since the amount of power support that a distributed PV can make in practice mainly depend on its capacity and solar irradiance, a good strategy is to have the PV systems with higher capability to contribute with more power. Adopting this objective, we propose the following inversion rule:

$$\Delta V_{PV,i} = \Delta V_{PV}^a, \quad \Delta V_{dc,i}^{ref} = \Delta V_{dc}^{ref,a} \quad (136)$$

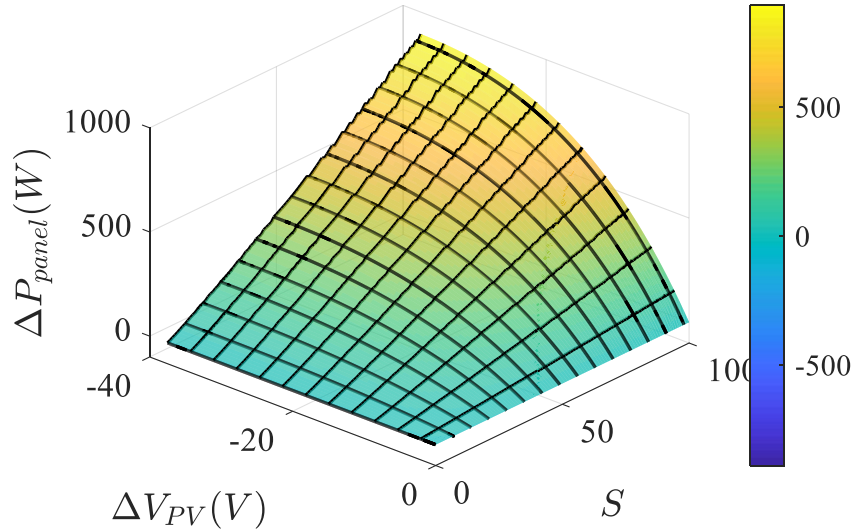


Figure 4.8. The LUT surface of $g(\Delta V_{PV}, S, T)$ for a 5695 W PV panel at 26.85 °C.

which corresponds to setting all the individual inputs equal to the aggregate input. This inversion is also illustrated in Figure 4.7. We can easily verify that the definition of \mathbf{u}^a still holds with (136). Furthermore, we will show that this simple, easy-to-implement method can also achieve the aforementioned objective.

c.1) $\Delta V_{PV,i}$

$\Delta V_{PV,i}$ determines the new operating point and thus the steady-state power output of the PV system. Considering several PV systems with different capacities, since their PV arrays all consist of identical PV panels connected in parallel (as shown in Figure 4.2), the same $\Delta V_{PV,i}$ will result in different $\Delta P_{PV,i}$, which are in proportion to the number of PV panels, or equivalently, the rated power.

Solar irradiance S is the other main variable that effects the power support capability of a PV system. The LUT surface plotted in Figure 4.8 describes the relationship among ΔP_{panel} , ΔV_{PV} , and S . We can easily observe that, for the same value of ΔV_{PV} , the ΔP_{panel} increases as the S

becomes higher. Therefore, with the same $\Delta V_{PV,i}$, PV systems under higher S will have more power change in each of their PV panel and thus in the total output as well.

c.2) $\Delta V_{dc,i}^{ref}$

The other control input $\Delta V_{dc,i}^{ref}$ adjusts the DC-link voltage to obtain power from the capacitor. According to (91), this power is proportionally related to the capacitance. We also know that the capacitance should be chosen in proportion to the PV system rated power. Therefore, with the same $\Delta V_{dc,i}^{ref}$, the PV system with larger capacity, and thus capacitance, will have more power released, or absorbed, from its DC-link capacitor.

4.3 Test Results

In this section, we first validate that the reduced-order aggregate model can effectively represent the dynamics of a group of distributed PV. Then we demonstrate that the aggregate model can be successfully applied in the UIO-based tracking LQR to provide frequency support during frequency event. Moreover, we also illustrate the effectiveness of proposed inversion method.

4.3.1 Reduced-order Aggregate Model Validation

To validate the proposed reduced-order aggregate model, we first built an IEEE 34 node test feeder in MATLAB/Simulink to represent an area of distribution system. Then, 10 single-phase PV systems are connected to different locations. Each PV system is as illustrated in Figure 4.2. We use this test feeder as the benchmark system and compare its overall dynamics with that from the aggregate model. Key parameters of the PV system are given in Appendix V, where we assume the basic parameters are the same for all the distributed PV. But for the solar irradiance, capacity, and control parameters, they vary from each PV system.

Since the aggregate model is primarily derived for designing frequency support control functions, we are particularly interested in the dynamics of two relevant quantities: total PV system output power (ΔP_{PV}^a) and aggregate DC-link voltage ($\Delta V_{dc}^{ref,a}$), following the changes in the control inputs. To test, the distributed PV in the benchmark system are set to be operating at 85% of their MPPs (nominal de-loading condition). In the first test case, at $t = 1.5$ s, we decrease the PV array voltages by different values as listed in Appendix V. In this case, we consider that the distributed PV are expected to output more power. Therefore, all the $\Delta V_{PV,i}$ are negative. In the meantime, we calculate the corresponding aggregate control input (ΔV_{PV}^a) and inject it to the aggregate model. Finally, we can compare the dynamics of the aggregate model with calculated aggregate dynamics from the benchmark system. In Figure 4.9 (a), the total increment power from the aggregate model

provides very good approximation to that calculated from original distributed PV. There is slight difference in the steady-state value which is caused by the LUT approximation we made in b.1). Figure 4.9 (b) shows the aggregate DC-link voltage profiles and verifies that the response obtained from the aggregate model is very close to that of the benchmark system.

In the second test case, we perturb the other control input which is $\Delta V_{dc,i}^{ref}$. Similarly, we want to obtain power from DC-link, and thus decrease the voltage references by different values. We observe immediate total power release from Figure 4.10 (a), and shortly after that, the power decreases to zero as the aggregate DC-link voltage shown in Figure 4.10 (b) settles to its steady-state. Figure 4.10 (a) and (b) show that the voltage and power profiles from the aggregate model are again very close to those from the original distributed PV.

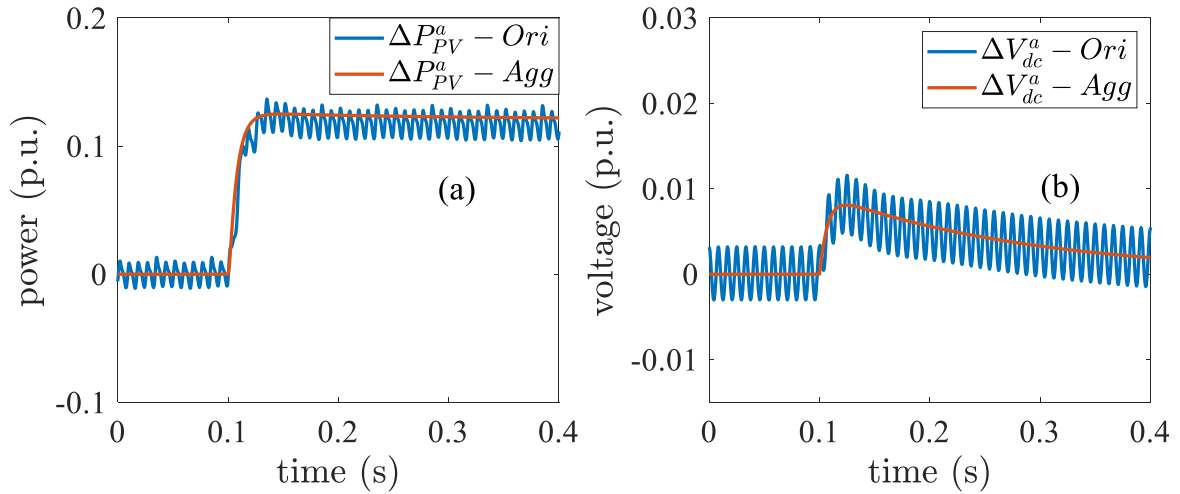


Figure 4.9. When $\Delta V_{PV}^a = -12.775$ V, (a) comparison of total increment power ΔP_{PV}^a ; (b) comparison of aggregate DC-link voltage ΔV_{dc}^a .

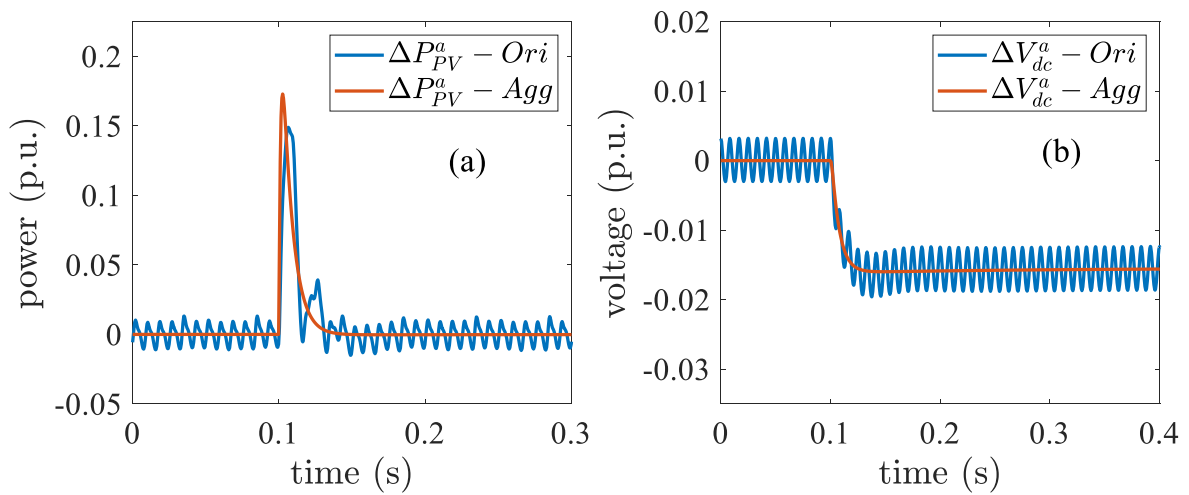


Figure 4.10. When $\Delta V_{dc}^{ref,a} = -7.730$ V, (a) comparison of total increment power ΔP_{PV}^a ; (b) comparison of aggregate DC-link voltage ΔV_{dc}^a .

4.3.2 Controller Performance

To demonstrate the effectiveness of proposed control scheme, we consider the standard three-machine-nine-bus WECC system but modify its capacity down to 116 MVA (S_b) to represent a small-scale power system. Then we add four of the IEEE 34 node test feeders at bus 6, as shown in Figure 4.11, with each feeder having 10 distributed PV. Each feeder has 10 distributed PV. So in this test system, we have 40 distributed PV whose basic parameters are listed in Appendix V and other parameters with variations are listed in Appendix VI, and their total capacity is 8.189 MW (P_r^{tot}). The test system is built in MATLAB/Simulink where we conduct time-domain simulations with 5 μ s time resolution for the following study.

To design the UIO-based tracking LQR, we follow the design steps in Chapter 3. The same design parameters are chosen, except for H^{ref} and R^{ref} of the reference system as they should be related to the PV penetration level. In this case, the calculated inertia and droop constants for reference system are provided in Table 4.2, along with those for the original test system without proposed control.

For the test case, we apply a large load disturbance of 0.086 pu at bus 8. In Figure 4.12 (a), we plot and compare the frequency responses obtained from (i) system with proposed control scheme; (ii) reference system; and (iii) system with no frequency support control from distributed PV. From the figure we can clearly see that the frequency with proposed control effectively tracks that of the reference system frequency. The figure also indicates that, by closely following the reference system frequency, the frequency response of the system is improved as desired, specifically in terms of nadir, RoCoF, and settling frequency, compared to that of the original system without control. Therefore, we can confirm that the distributed PV under proposed control scheme can provide frequency support to improve the frequency response as designed. To support

the very good tracking performance observed in Figure 4.12 (a), we also plot the absolute tracking error between frequencies from (i) and (ii) in Figure 4.12 (b). We can see that the error is very small with the maximum value being still less than 0.005%.

Next, we want to verify that the proposed inversion method can achieve its design objective. In order to do this, we first select 4 distributed PV systems from the above simulation

Table 4.2. Part of the Control Design Parameters

| | Test System | | Reference System | |
|----------------|-------------|----------|------------------|----------|
| Inertia | H_g | 5.9746 s | H^{ref} | 6.2365 s |
| Droop | R_g | 8% | R^{ref} | 7.66% |

with the same rated power but different solar irradiance, and plot their power responses in Figure 4.13 (a). Per the control signal inversion in (136), they all share the same control inputs. But as shown in the plot, the PV system with higher solar irradiance generate more power as expected, under the same event. In the second case, we choose another set of 4 PV systems with the same irradiance but different rated power. Again, we can see from Figure 4.13 (c) that the increment power output are positively correlated to the PV systems' capacities. In addition, as indicated in Figure 4.13 (b) and (d), both of the positive correlations between steady-state ΔP_{PV} and solar irradiance S are almost linear.

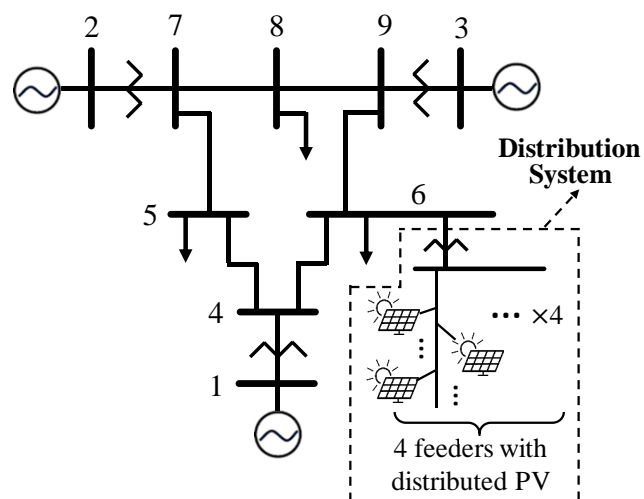


Figure 4.11. Modified WECC 9-bus system with distributed PV.

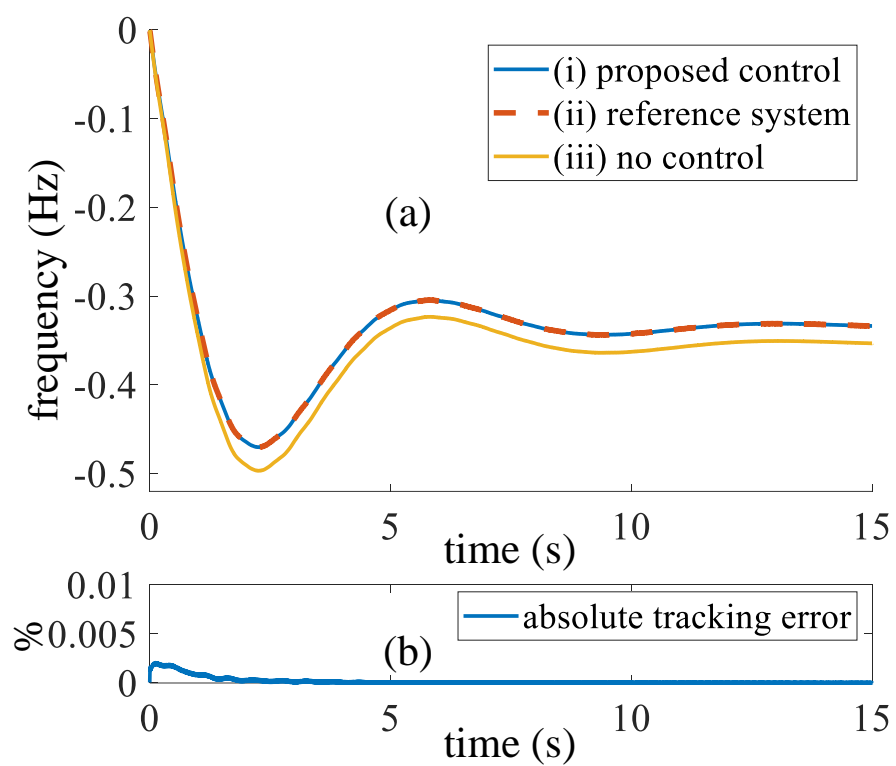


Figure 4.12. (a) Frequency response comparison under load disturbance; (b) Absolute error between frequencies of (i) and (ii).

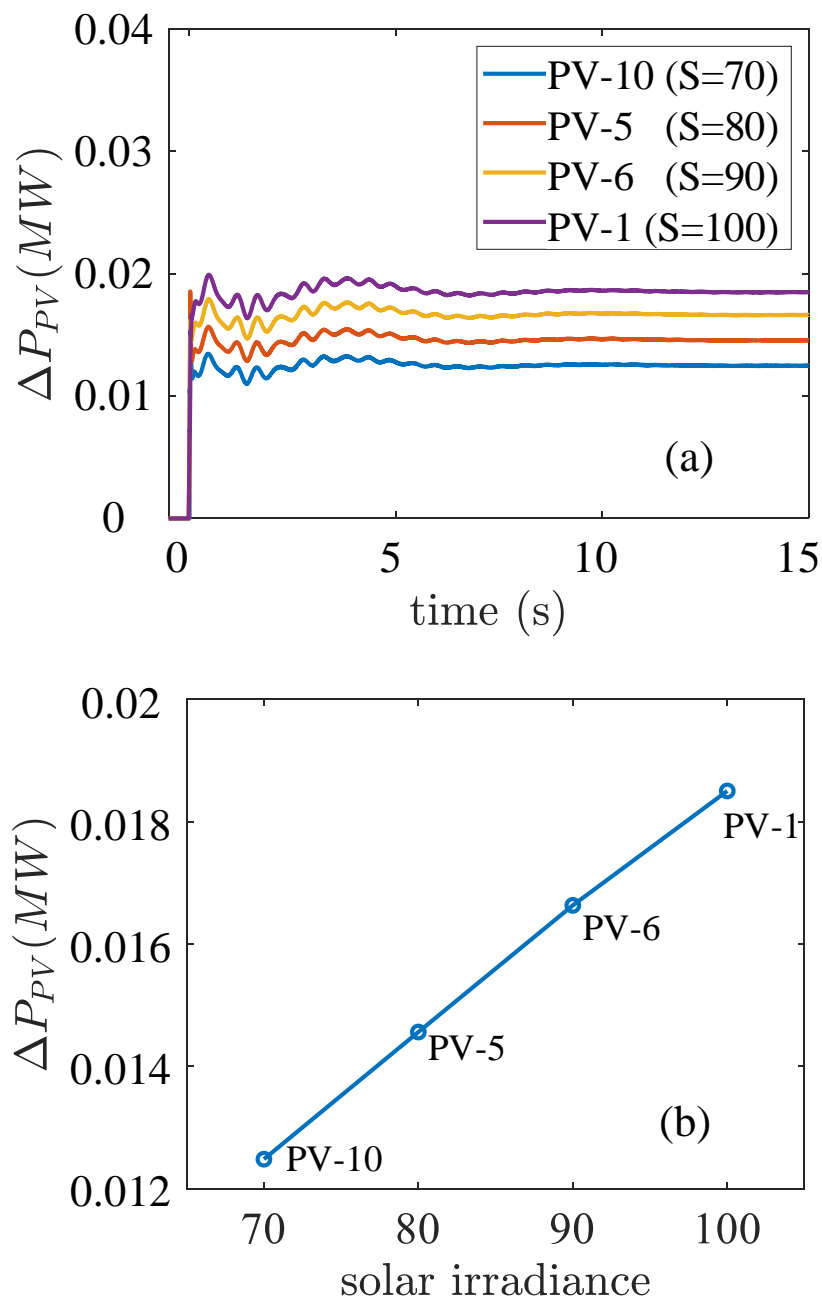


Figure 4.13. For PV systems with the same rated power (200 KW), but different solar irradiance: (a) comparison of power responses; (b) correlation between steady-state ΔP_{PV} and

S.

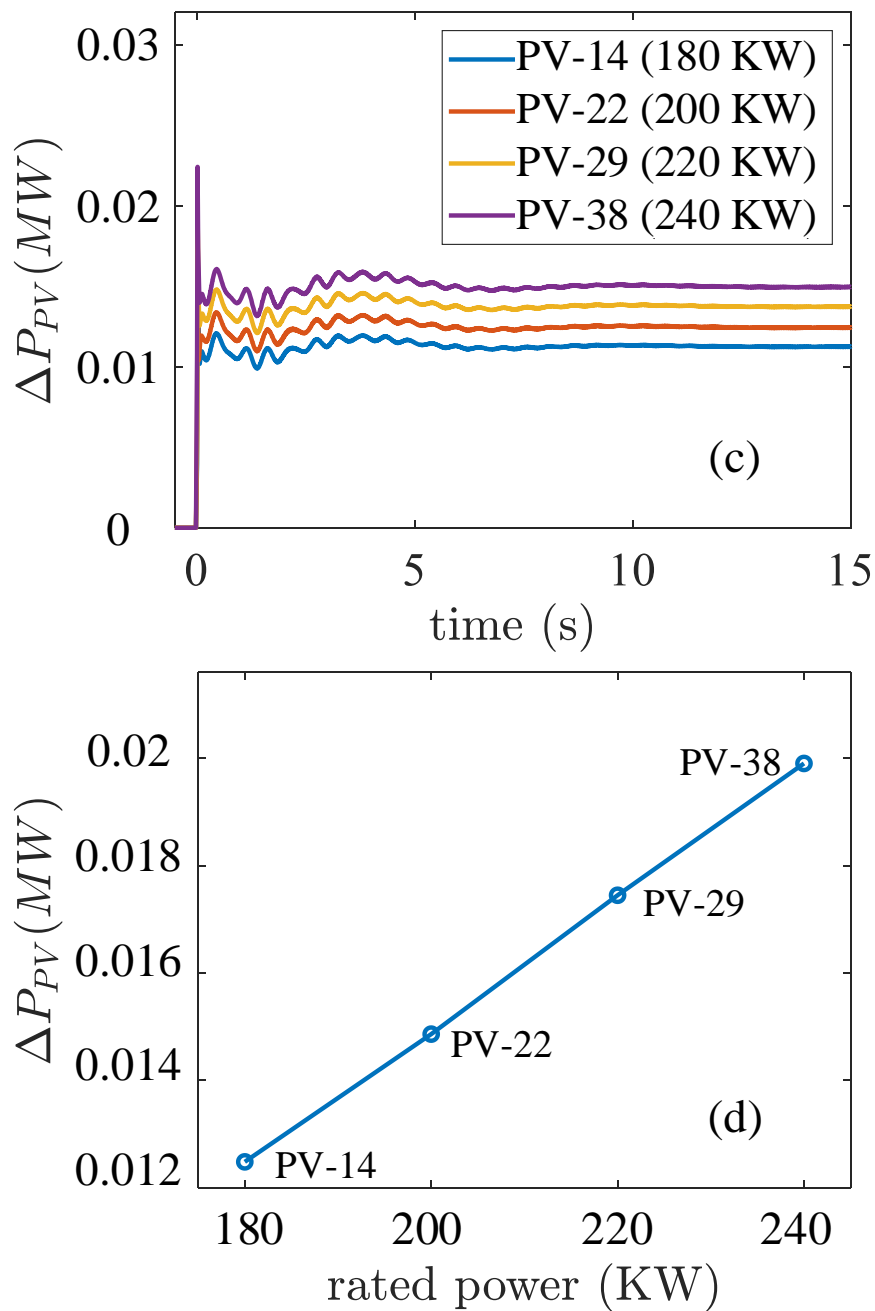


Figure 4.14. For PV systems with the same solar irradiance ($S=70$), but different rated power:

(c) comparison of power responses; (b) correlation between steady-state ΔP_{PV} and rated power.

4.4 Conclusion

This chapter focuses on utilizing distributed PV to provide primary frequency support to the bulk system. For this purpose, we first propose a reduced-order aggregate model to represent the overall dynamic behaviors of a group of distributed PV with different capacities, irradiance, and control parameters. The derived model preserves the same structure and order as those of the SSM for one PV system. Moreover, supervisory control inputs are also considered in the aggregate model. The above features greatly facilitate the design of frequency support control.

Based on the proposed aggregate model, the UIO-based tracking LQR method from literature is adopted and revised to incorporate distributed PV for providing frequency support. Filling the gap between this model-based controller and the practical systems, we also propose an inversion method to obtain individual control input for each distributed PV from the aggregate control signal. Test results have indicated the effectiveness of both frequency tracking and improvement of the test system frequency response. It is also demonstrated that, with the proposed inversion method, PV systems with higher potential (larger capacity or higher irradiance) respond with more power under the same event. Therefore, the proposed control scheme can indeed be adopted by distribution system operators or aggregators for providing frequency support service, especially to small-scale systems with high penetration of distributed PV.

CHAPTER 5 : SUMMARY AND FUTURE WORK

5.1 Summary of Current Work

In this dissertation, under the challenges of PV penetration on the conventional generation control, new control schemes that can enable PV systems to provide frequency support to the electric power systems are proposed.

To identify and assess the impact of increasing PV penetration on system frequency response, two simulation testbeds are developed in PSCAD and dynamic co-simulation environment, respectively. The testbed in PSCAD is suited for time-domain simulations of small systems, while the co-simulation testbed shows its advantage for phasor-domain simulations of very large scale systems. Using these two testbeds, we simulated frequency events under increasing levels of PV penetration. Simulations results clearly reveal the negative impacts from higher PV penetration on the system frequency response, in terms of frequency nadir, RoCoF, and settling frequency.

In order to enable frequency support functions from PV, we first consider large-scale PV plants and propose a novel control method which is designed from bulk-system-level. In order to achieve the desired frequency response, a tracking LQR is designed to help system frequency accurately follow that from a reference system under the same load disturbance. The controller also contains a UIO from which both the system states and disturbance can be estimated. Test results strongly indicate the effectiveness the proposed control method by the very good performance of both frequency tracking and variable estimation. Test results also show that the proposed method requires less de-loading of PV plant than the conventional method, which is of great significance in term of economics. To facilitate the design of this control method, we also propose a new SSM for the three-phase two-stage PV system. This model is suitable for designing

frequency support controls for PV and can be extended to a linear model for PV system with an LUT. Model validation results indicate that the SSM provides a close match of system dynamics with that of the detailed nonlinear PV system model.

Other than large-scale PV plants which consist of identical subsystems, distributed PV are also under the scope of this dissertation. In order to utilize distributed PV to provide the frequency support to the bulk system, we first propose a reduced-order aggregate model to represent the overall dynamic behaviors of a diverse group of distributed PV with varying capacities, solar irradiance, and control parameters. The derived model preserves the same structure and order as that of one PV system. Moreover, inputs needed for the supervisory control are also preserved in the aggregate model. These features greatly facilitate the design of frequency support control. Test results show that the model provides a very close approximation of the response, even under quite large diversity among the distributed PV systems.

Then, we show that the UIO-based tracking LQR method can be tailored for a group of distributed PV to achieve supervisory frequency support control. An inversion method is also proposed to obtain individual control input for each distributed PV from the aggregate control signal. Simulation results on the test system confirm the effectiveness of both frequency tracking and improvement of the test system frequency response. It is also demonstrated that the proposed inversion method provides an effective way to allocate the total control effort to individual PV systems.

These results also indicate that the proposed control scheme can indeed be adopted by distribution system operators or aggregators for providing frequency support service from distributed PV, especially to small-scale systems with high penetration of distributed PV.

5.2 Future Work

- **Limitation of power reserve from PV**

The proposed control methods assume sufficient power reserves in PV systems in order to achieve desired frequency response performance. However, this assumption may be difficult to hold in practice. When more power is needed than the current reserve, control performance will be inevitably affected. A potential solution is to consider the presence of energy storage systems in the control to coordinately assure desired frequency response capability.

- **Uncertainties in PV system modeling**

The PV system models used in the control design, especially the reduced-order aggregate model for distributed PV, requires information such as rated power and control parameters. In practice, these information may not be available and are also subject to changes. Therefore, models with exact parameters may be very difficult to obtain and thus affect control performance. One solution is to use the adaptive control theory to bypass the need of exact information of model parameters, as the model structures are fixed and known.

- **Communication requirements for distributed PV**

The proposed control method for distributed PV assumes communication links from each PV to the controller to receive the control signals. This way of communication is simple but liable to high cost considering the distributed geographical locations and vulnerability as one link's failure will fail the control objective. The potential solution is to exploit distributed control techniques, such as consensus control, to implement the individual control signals for each distributed PV.

REFERENCES

- [1] NERC, "BAL-003-1.1: Frequency Response and Frequency Bias Setting."
<https://www.nerc.com/pa/Stand/Reliability%20Standards/BAL-003-1.1.pdf>.Nov. 2015.
- [2] P.W. Sauer and M.A. Pai, "Power system dynamics and stability," *Urbana*, 1998.
- [3] A.J. Wood and B.F. Wollenberg, Power generation, operation, and control, John Wiley & Sons, 2012, .
- [4] U.S. Energy Information Administration, "Annual Energy Outlook 2018,"
2018.<https://www.eia.gov/outlooks/aeo/pdf/AEO2018.pdf>.
- [5] U.S. Energy Information Administration, "Today in Energy,"
<https://www.eia.gov/todayinenergy/detail.php?id=38752#>.Mar 19. 2019. Accessed on
April 09.2019.
- [6] T. Esmam and P.L. Chapman, "Comparison of photovoltaic array maximum power point tracking techniques," *IEEE Transactions on Energy Conversions*, vol. 22, no.2,pp. 439-449, 2007.
- [7] S. You, Y. Liu, X. Zhang, Y. Su, L. Wu, Y. Liu and S.W. Hadley, "Impact of high PV penetration on US eastern interconnection frequency response," In *Power & Energy Society General Meeting, 2017 IEEE*, pp. 1-5, 2017.
- [8] N.W. Miller, M. Shao, S. Pajic and R. D'Aquila, "Eastern frequency response study,"
National Renewable Energy Lab.(NREL), Golden, CO (United States)., 2013.

- [9] C. Seneviratne and C. Ozansoy, "Frequency response due to a large generator loss with the increasing penetration of wind/PV generation—A literature review," *Renewable and Sustainable Energy Reviews*, vol. 57, pp. 659-668, 2016.
- [10] Y. Liu, S. You, J. Tan, Y. Zhang and Y. Liu, "Frequency Response Assessment and Enhancement of the US Power Grids Toward Extra-High Photovoltaic Generation Penetrations—An Industry Perspective," *IEEE Transactions on Power System*, vol. 33, no.3, pp. 3438-3449, 2018.
- [11] S. You, Y. Liu, G. Kou, X. Zhang, W. Yao, Y. Su, S.W. Hadley and Y. Liu, "Non-invasive identification of inertia distribution change in high renewable systems using distribution level PMU," *IEEE Transactions on Power System*, vol. 33, no.1, pp. 1110-1112, 2018.
- [12] Q. Li and S. Abhyankar, "Evaluation of High Solar Penetration Impact on Bulk System Stability through a Transmission-Distribution Dynamics Co-simulation," In *2019 IEEE Power and Energy Society General Meeting (PESGM)*, 2019.
- [13] Hydro Quebec, "Transmission Provider Technical Requirements for the Connection of Power Plants to the Hydro Quebec Transmission System," http://www.hydroquebec.com/transenergie/fr/commerce/pdf/exigence_raccordement_fev_09_en.pdf.
- [14] FERC, "Essential Reliability Services and the Evolving Bulk-Power System—Primary Frequency Response," <https://elibrary.ferc.gov/IDMWS/common/downloadOpen.asp?downloadfile=20180215%2D3099%2832695275%29%2Epdf&folder=15219837&fileid=14823757&trial=1>. Feb 15, 2018.

- [15] E.N. Code, "Requirements for grid connection applicable to all generators," *ENTSO-E: Brussels, Belgium*, 2013.
- [16] ERCOT, "Critical Inertia System Operating Limit," http://www.ercot.com/content/wcm/lists/144927/Inertia_Basic_Concepts_Impacts_On_ER_COT_v0.pdf.
- [17] S. You, Y. Liu, J. Tan, M.T. Gonzalez, X. Zhang, Y. Zhang and Y. Liu, "Comparative Assessment of Tactics to Improve Primary Frequency Response Without Curtailing Solar Output in High Photovoltaic Interconnection Grids," *IEEE Transactions on Sustainable Energy*, 2018.
- [18] N. Kakimoto, S. Takayama, H. Satoh and K. Nakamura, "Power modulation of photovoltaic generator for frequency control of power system," *IEEE Transactions on Energy Conversions.*, vol. 24, no.4,pp. 943-949, 2009.
- [19] M. Datta, T. Senjyu, A. Yona, T. Funabashi and C. Kim, "A frequency-control approach by photovoltaic generator in a PV–diesel hybrid power system," *IEEE Transactions on Energy Conversions*, vol. 26, no.2,pp. 559-571, 2011.
- [20] W.A. Omran, M. Kazerani and M. Salama, "Investigation of methods for reduction of power fluctuations generated from large grid-connected photovoltaic systems," *IEEE Transactions on Energy Conversions*, vol. 26, no.1,pp. 318-327, 2011.
- [21] H. Xin, Y. Liu, Z. Wang, D. Gan and T. Yang, "A new frequency regulation strategy for photovoltaic systems without energy storage," *IEEE Transactions on Sustainable Energy*, vol. 4, no.4,pp. 985-993, 2013.
- [22] A.F. Hoke, M. Shirazi, S. Chakraborty, E. Muljadi and D. Maksimovic, "Rapid Active Power Control of Photovoltaic Systems for Grid Frequency Support," *IEEE Journal of*

- Emerging and Selected Topics in Power Electronics (2017)*, vol. 5, no.3,pp. 1154-1163, Sep. 2017.
- [23] S.I. Nanou, A.G. Papakonstantinou and S.A. Papathanassiou, "A generic model of two-stage grid-connected PV systems with primary frequency response and inertia emulation," *Electric Power System Research*, vol. 127, pp. 186-196, 2015.
- [24] B. Crăciun, T. Kerekes, D. Séra and R. Teodorescu, "Frequency support functions in large PV power plants with active power reserves," *IEEE Journal of Emerging and Selected Topics in Power Electronics*, vol. 2, no.4,pp. 849-858, 2014.
- [25] P. Rodriguez, I. Candela and A. Luna, "Control of PV generation systems using the synchronous power controller," In *2013 IEEE Energy Conversion Congress and Exposition*, pp. 993-998, 2013.
- [26] M.F.M. Arani and E.F. El-Saadany, "Implementing virtual inertia in DFIG-based wind power generation," *IEEE Transactions on Power System*, vol. 28, no.2,pp. 1373-1384, 2013.
- [27] D. Ochoa and S. Martinez, "Fast-frequency response provided by DFIG-wind turbines and its impact on the grid," *IEEE Transactions on Power System*, vol. 32, no.5,pp. 4002-4011, 2017.
- [28] X. Lyu, Z. Xu, J. Zhao and K. P. Wong, "Advanced frequency support strategy of photovoltaic system considering changing working conditions," *IET Generation, Transmission & Distribution*, vol. 12, pp. 363-370, 2018.ID: 1.
- [29] W. Im, C. Wang, W. Liu, L. Liu and J. Kim, "Distributed virtual inertia based control of multiple photovoltaic systems in autonomous microgrid," *IEEE/CAA Journal of Automatica Sinica*, vol. 4, no.3,pp. 512-519, 2017.

- [30] B. Palmintier, R. Broderick, B. Mather, M. Coddington, K. Baker, F. Ding, M. Reno, M. Lave and A. Bharatkumar, "On the path to SunShot. Emerging issues and challenges in integrating solar with the distribution system," National Renewable Energy Lab.(NREL), Golden, CO (United States)., 2016.
- [31] G. Barbose, N. Darghouth, D. Millstein, S. Cates, N. DiSanti and R. Widiss, "Tracking the Sun IX: The installed price of residential and non-residential photovoltaic systems in the United States," Lawrence Berkeley National Lab.(LBNL), Berkeley, CA (United States)., 2016.
- [32] H. Saadat, *Power System Analysis McGraw-Hill Series in Electrical Computer Engineering*, 1999.
- [33] N. Jaleeli, L.S. VanSlyck, D.N. Ewart, L.H. Fink and A.G. Hoffmann, "Understanding automatic generation control," *IEEE Transactions on Power System*, vol. 7, no.3, pp. 1106-1122, 1992.
- [34] D.B. Eidson and M.D. Ilic, "Advanced generation control with economic dispatch," In *Decision and Control, 1995., Proceedings of the 34th IEEE Conference on*, pp. 3450-3458, 1995.
- [35] Eto, J., J. Undrill, P. Mackin, R. Daschmans, B. Williams, B. Haney, R. Hunt, et al. 2010. "Use of Frequency Response Metrics to Assess the Planning and Operating Requirements for Reliable Integration of Variable Renewable Generation". LBNL-4142E. Berkeley, California: Lawrence Berkeley National Laboratory.
- [36] V. Gevorgian and B. O'Neill, "Advanced grid-friendly controls demonstration project for utility-scale PV power plants," 2016. United States. doi:10.2172/1236761.

- [37] M. Munsell, "US solar market sets new record, installing 7.3 GW of solar PV in 2015," *Greentech Media*, 2016.
- [38] Solar Energies Industry Association, "U.S. Solar Market Insight (Technical Report)," December 13,. 2016.
- [39] U.S. Energy Information Administration, "Electric Power Monthly," December 23,. 2016.
- [40] A. Sieminski, "Annual energy outlook 2015," *US Energy Information Administration*, 2015.
- [41] National Renewable Energy Laboratory and U.S. Department of Energy, "SunShot Vision Study," 2017.<https://www1.eere.energy.gov/solar/pdfs/47927.pdf>.
- [42] Huajie Gu, Ruifeng Yan and T.K. Saha, "Minimum Synchronous Inertia Requirement of Renewable Power Systems," *IEEE Transactions on Power Delivery*, vol. 33, no.2,pp. 1533-1543, Mar. 2018.
- [43] M. Datta and T. Senjyu, "Fuzzy Control of Distributed PV Inverters/Energy Storage Systems/Electric Vehicles for Frequency Regulation in a Large Power System," *IEEE Transactions on Smart Grid*, vol. 4, pp. 479-488, 2013.ID: 1.
- [44] P.G. Bueno, J.C. Hernández and F.J. Ruiz-Rodriguez, "Stability assessment for transmission systems with large utility-scale photovoltaic units," *IET Renewable Power Generation*, vol. 10, no.5,pp. 584-597, 2016.
- [45] Task Force, WECC Renewable Energy Modeling Task, "*WECC solar plant dynamic modeling guidelines*," 2014.
- [46] H. Cai, J. Xiang and W. Wei, "Modelling, analysis and control design of a two-stage photovoltaic generation system," *IET Renewable Power Generation*, vol. 10, no.8,pp. 1195-1203, 2016.

- [47] A. Yazdani and P.P. Dash, "A Control Methodology and Characterization of Dynamics for a Photovoltaic (PV) System Interfaced With a Distribution Network," *IEEE Transactions on Power Delivery*, vol. 24, no.3,pp. 1538-1551, Jul. 2009.
- [48] K.H. Hussein, I. Muta, T. Hoshino and M. Osakada, "Maximum photovoltaic power tracking: an algorithm for rapidly changing atmospheric conditions," *IEE Proceedings-Generation, Transmission and Distribution*, vol. 142, no.1,pp. 59-64, 1995.
- [49] J. Salaet, S. Alepuz, A. Gilabert and J. Bordonau, "Comparison between two methods of DQ transformation for single phase converters control. Application to a 3-level boost rectifier," In *Power Electronics Specialists Conference, 2004. PESC 04. 2004 IEEE 35th Annual*, pp. 214-220, 2004.
- [50] L.D. Watson, J.W. Kimball and S. Atcitty, "Linear single phase inverter model for Battery Energy Storage System evaluation and controller design," *Applied Power Electronics Conference and Exposition (APEC), 2012. IEEE..*
- [51] Task Force, WECC Renewable Energy Modeling Task, "WECC solar plant dynamic modeling guidelines," 2014.
- [52] D.G. Photovoltaics and E. Storage, "IEEE Standard for Interconnection and Interoperability of Distributed Energy Resources with Associated Electric Power Systems Interfaces," .
- [53] H. Manitoba, "Research centre," *PSCAD/EMTDC: Electromagnetic Transients Program Including Dc Systems*, 1994.
- [54] W.H. Kersting, "Radial distribution test feeders," *IEEE Transactions on Power System.*, vol. 6, no.3,pp. 975-985, 1991.

- [55] B. Palmintier, D. Krishnamurthy, P. Top, S. Smith, J. Daily and J. Fuller, "Design of the HELICS high-performance transmission-distribution-communication-market co-simulation framework," In *Proc. 2017 Workshop on Modeling and Simulation of Cyber-Physical Energy Systems, Pittsburgh, PA, 2017*.
- [56] P. Kundur, N.J. Balu and M.G. Lauby, *Power system stability and control*, McGraw-hill New York, 1994, .
- [57] S. Balay, S. Abhyankar, M. Adams, J. Brown, P. Brune, K. Buschelman, L.D. Dalcin, V. Eijkhout, W. Gropp and D. Kaushik, "No title," *Petsc Users Manual Revision 3.8*, 2017.
- [58] A. Shrirang, "Power grid dynamics modeling, simulation, and visualization capabilities," 2016.
- [59] R.C. Dugan and T.E. McDermott, "An open source platform for collaborating on smart grid research," In *Power and Energy Society General Meeting, 2011 IEEE*, pp. 1-7, 2011.
- [60] P. Wall and V. Terzija, "Simultaneous Estimation of the Time of Disturbance and Inertia in Power Systems," *IEEE Transactions on Power Delivery*, vol. 29, pp. 2018-2031, 2014.ID: 1.
- [61] D. Apostolopoulou, P.W. Sauer and A.D. Dominguez-Garcia, "Balancing Authority Area Model and its Application to the Design of Adaptive AGC Systems," *IEEE Transactions on Power Delivery*, vol. 31, no.5, pp. 3756-3764, Sep. 2016.
- [62] Q. Shi, F. Li and H. Cui, "Analytical Method to Aggregate Multi-Machine SFR Model With Applications in Power System Dynamic Studies," *IEEE Transactions on Power Systems*, vol. 33, pp. 6355-6367, 2018.ID: 1.
- [63] J. Chen and R.J. Patton, *Robust model-based fault diagnosis for dynamic systems*, Springer Science & Business Media, 2012, .

- [64] R.J. Patton, P.M. Frank and R.N. Clarke, *Fault diagnosis in dynamic systems: theory and application*, Prentice-Hall, Inc., 1989, .
- [65] S. Nazari, "The Unknown Input Observer and its Advantages with Examples," *arXiv Preprint arXiv:1504.07300*, 2015.
- [66] B. Shafai and M. Saif, "Proportional-integral observer in robust control, fault detection, and decentralized control of dynamic systems," in *Control and Systems Engineering*, Springer, 2015, pp. 13-43.
- [67] D.E. Kirk, *Optimal control theory: an introduction*, Courier Corporation, 2012, .
- [68] K. Zhou, J.C. Doyle and K. Glover, *Robust and optimal control*, Prentice hall New Jersey, 1996, .
- [69] H. Karimi, M. Karimi-Ghartemani and M. R. Iravani, "Estimation of frequency and its rate of change for applications in power systems," *IEEE Transactions on Power Delivery*, vol. 19, pp. 472-480, 2004.ID: 1.
- [70] S. Gao and M. Barnes, "Phase-locked loop for AC systems: Analyses and comparisons," *6th IET International Conference on Power Electronics, Machines and Drives (PEMD 2012)*, pp. 1-6, 2012.ID: 1.
- [71] C. Roselund, "Hawaii utilities seek more renewables, storage and now grid services too," *PV Magazine*, Apr 9, . 2019.
- [72] D. Remon, A.M. Cantarellas, J.D. Nieto, W. Zhang and P. Rodriguez, "Aggregated model of a distributed PV plant using the synchronous power controller," *2015 IEEE 24th International Symposium on Industrial Electronics (ISIE)* IEEE, 2015.

- [73] J. T. Bi, W. Du and H. F. Wang, "Aggregated dynamic model of grid-connected PV generation farms," *International Conference on Renewable Power Generation (RPG 2015)*, pp. 1-6, 2015.ID: 1.
- [74] Y. Han, M. Luo, X. Zhao, J. M. Guerrero and L. Xu, "Comparative Performance Evaluation of Orthogonal-Signal-Generators-Based Single-Phase PLL Algorithms—A Survey," *IEEE Transactions on Power Electronics*, vol. 31, pp. 3932-3944, 2016.ID: 1.
- [75] American National Standards Institute, "American National Standard Voltage Ratings (60Hz) for Electric Power Systems and Equipment," 2016.ANSI Std. C84.1-2016.
- [76] B. Hauke, "Basic calculation of a boost converter's power stage," *Texas Instruments, Application Report November*, pp. 1-9, 2009.
- [77] S. Mishra, D. Pullaguram, S. Achary Buragappu and D. Ramasubramanian, "Single-phase synchronverter for a grid-connected roof top photovoltaic system," *IET Renewable Power Generation*, vol. 10, pp. 1187-1194, 2016.ID: 1.

APPENDICES

Appendix I: Equations for 2dq PV System Model

1) PV Array

$$i_{PV} = n_p I_{ph} - n_p I_{rs} \left(e^{\frac{q}{kT} \frac{v_{PV}}{n_s}} - 1 \right) \quad (137)$$

$$I_{ph} = [I_{scr} + k_T (T - T_r)] \frac{S}{100} \quad (138)$$

$$i_{PV,2d} = 0, i_{PV,2q} = 0 \quad (139)$$

$$v_{PV,2d} = 0, v_{PV,2q} = 0 \quad (140)$$

2) DC-DC Converter

$$i_{dc1,dc} = \frac{v_{PV,dc} i_{PV,dc}}{v_{dc,dc}} \quad (141)$$

$$i_{dc1,2d} = \frac{i_{PV,dc} v_{PV,2d} - i_{dc1,dc} v_{dc,2d}}{v_{dc,dc}} \quad (142)$$

$$i_{dc1,2q} = \frac{i_{PV,dc} v_{PV,2q} - i_{dc1,dc} v_{dc,2q}}{v_{dc,dc}} \quad (143)$$

3) DC-link

$$\frac{dv_{dc,dc}}{dt} = \frac{i_{dc1,dc} - i_{dc2,dc}}{C} \quad (144)$$

$$\frac{dv_{dc,2d}}{dt} = \frac{i_{dc1,2d} - i_{dc2,2d}}{C} + 2\omega v_{dc,2q} \quad (145)$$

$$\frac{dv_{dc,2q}}{dt} = \frac{i_{dc1,2q} - i_{dc2,2q}}{C} + 2\omega v_{dc,2d} \quad (146)$$

4) Inverter

$$i_{dc2,dc} = \frac{i_{ac,d} v_{ac,d} + i_{ac,q} v_{ac,q}}{2v_{dc}} \quad (147)$$

$$i_{dc2,2d} = \frac{i_{ac,d} v_{ac,q} + i_{ac,q} v_{ac,d}}{2v_{dc}} \quad (148)$$

$$i_{dc2,2q} = \frac{i_{ac,d}v_{ac,d} - i_{ac,q}v_{ac,q}}{2v_{dc}} \quad (149)$$

5) Inverter Control

$$\frac{di_{ac,d}}{dt} = -\frac{1}{\tau}i_{ac,d} - \frac{K_P}{\tau}v_{dc,dc} + \frac{1}{\tau}x + \frac{K_P}{\tau}v_{dc,ref} \quad (150)$$

$$\frac{di_{ac,q}}{dt} = -\frac{1}{\tau}i_{ac,q} + \frac{1}{\tau}i_{ac,q,ref} \quad (151)$$

$$\frac{dx}{dt} = -K_I v_{dc,dc} + K_I v_{dc,ref} \quad (152)$$

Appendix II: System Configurations of PSCAD Testbed

| System Parameters | PV Penetration Level | | |
|------------------------------|----------------------|-------|--|
| | 0% | 40% | 60% |
| Generator Rated Voltage (KV) | 13.78 | | |
| Generator Rated Current (KA) | 0.167 | 0.129 | 0.110 |
| Generator Rated Power (MVA) | 4 | 3.1 | 2.65 |
| Total Load (MW) | 2.25 | | |
| Inertia Constant (s) | 2 | | |
| Droop Constant (p.u.) | 0.04 | | |
| PV Rating (KW) | | | 822.a - 135 836.a – 30 836.b – 10 836.c – 42 836.a - 30 844.a – 135 844.a – 135 844.b – 135 844.c – 135 860.a – 16 860.b – 20 890.a – 150 890.b – 150 890.c - 150 888.a – 150 888.b – 150 888.c – 150 890.a – 150 890.b – 150 890.c - 150 |

Appendix III: System Configurations of Co-simulation Testbed

| System Parameters | | 14-bus System | 8500-node Feeder |
|--------------------------|-----|---------------|------------------|
| Total Load (MW) | | 287.17 | 12.005 |
| Number of Buses | | 14 | 4877 |
| Number of Boundary Buses | | 7 | N/A |
| Number of Feeders | | 24 | N/A |
| Number of Generators/PVs | | 5 | 10 |
| PV Rating (KW) | 0% | N/A | 0 |
| | 20% | N/A | 2.393 |
| | 40% | N/A | 4.786 |

Appendix IV: PV System Parameters

| | | | |
|------------------|----------------------------------|----------------------------|------|
| q | Unit electric charge | 1.602×10^{-19} C | |
| k | Boltzmann's constant | 1.38×10^{-23} J/K | |
| T | $p - n$ junction temperature | 300 K | |
| T_r | Reference temperature | 300 K | |
| k_T | Temperature coefficient | 0.0017 A/K | |
| A | Ideality factor | 1.92 | |
| I_{scr} | Cell short-circuit current | 8.03 A | |
| I_{rs} | Reverse saturation current | 1.2×10^{-7} A | |
| S | Solar irradiation level | 1 | |
| n_s | # of PV cells per string | 500 | |
| n_p | # of PV strings | 70 | |
| P_{PV}^r | PV system rated power | 200 KW | |
| C | DC-link capacitance | 20000 μ F | |
| R | Filter resistance | 0.001 Ω | |
| L | Filter inductance | 2e-5 H | |
| V_{sd} | Nominal system voltage in d-axis | 317 V | |
| $V_{dc,0}^{ref}$ | Nominal DC-link voltage | 500 V | |
| k_P | 20 | k_P^i | 0.02 |
| k_I | 100 | k_I^i | 1 |

Appendix V: Distributed PV System Parameters

| Basic Parameters | | | |
|-----------------------------------|----------------------------------|--|----------------------|
| T | Environment temperature | | 300 K |
| n_s | # of PV cells per string | | 500 |
| n_p | # of PV strings | | 70 |
| P^r | PV system rated power | | 200 KW |
| C_d | Unit DC-link capacitance | | 2×10^{-7} F |
| R | Filter resistance | | 0.001 Ω |
| L | Filter inductance | | 2e-5 H |
| V_{sd} | Nominal system voltage in d-axis | | 317 V |
| $V_{dc,0}^{ref}$ | Nominal DC-link voltage | | 500 V |
| τ | Current loop time constant | | 0.001 |
| k_P^i | Current loop control parameter | | 0.02 |
| k_I^i | Current loop control parameter | | 1 |
| Parameters with variations | | | |
| S_i | Solar irradiance | [100, 70, 65, 80, 85, 90, 92, 75, 83, 90] | |
| $P_{r,i}$ | Rated Power (KW) | [200, 250, 220, 175, 200, 200, 250, 220, 175, 190] | |
| $k_{P,i}$ | Voltage loop control parameters | [10 15 20 20 17 10 15 20 20 17] | |
| $k_{I,i}$ | | [50 100 150 80 50 50 100 150 80 50] | |
| Control Inputs | | | |
| $\Delta V_{PV,i}$ | Change of PV array voltage (V) | [-10, -12, -15, -11, -8, -5, -18, -20, -17, -10] | |
| $\Delta V_{dc,i}^{ref}$ | Change of DC-link voltage (V) | [-10, -5, -8, -7, -5, -4, -9, -11, -6, -12] | |
| ΔV_{PV}^a | -12.775 V | $\Delta V_{dc}^{ref,a}$ | -7.730 V |

Appendix VI: Distributed PV System Parameters

| Parameter | Feeder # | Value |
|------------------|-----------------|--|
| S_i | 1 | [100, 90, 65, 85, 80, 90, 92, 75, 83, 70] |
| | 2 | [95, 85, 90, 70, 77, 75, 88, 83, 96, 100] |
| | 3 | [60, 70, 80, 75, 86, 95, 98, 68, 70, 83] |
| | 4 | [80, 80, 85, 86, 87, 95, 89, 70, 73, 65] |
| $P_{r,i}$ (KW) | 1 | [200, 250, 220, 175, 200, 200, 250, 220, 175, 200] |
| | 2 | [250, 220, 230, 180, 190, 220, 200, 240, 190, 195] |
| | 3 | [165, 200, 185, 200, 195, 200, 210, 200, 220, 190] |
| | 4 | [195, 190, 178, 196, 220, 210, 190, 240, 170, 250] |
| $k_{P,i}$ | 1 | [10, 15, 20, 20, 17, 10, 15, 20, 20, 17] |
| | 2 | [20, 20, 17, 15, 20, 22, 25, 15, 10, 12] |
| | 3 | [10, 25, 25, 22, 19, 15, 10, 12, 17, 20] |
| | 4 | [17, 19, 16, 20, 25, 23, 22, 20, 20, 17] |
| $k_{I,i}$ | 1 | [50, 100, 150, 80, 50, 50, 100, 150, 80, 50] |
| | 2 | [100, 100, 120, 200, 150, 150, 100, 50, 80, 200] |
| | 3 | [50, 80, 80, 95, 120, 110, 100, 100, 80, 75] |
| | 4 | [75, 75, 90, 150, 180, 200, 200, 220, 150, 100] |